RL-451

THE THREE-DIMENSIONAL PHASED ARRAY: PHYSICAL REALIZABILITY AND DIRECTIVE PROPERTIES

by

Thomas Otto Mottl

A dissertation submitted in partial fulfillment
of the requirements for the degree of
Doctor of Philosophy in the
University of Michigan
1968

Doctoral Committee:

Professor Chen-To Tai, Chairman
Professor Charles L. Dolph
Professor Ralph E. Hiatt
Professor John A. M. Lyon
Doctor Dipak L. Sengupta

ACKNOWLEDGEMENTS

I want to express my appreciation to all the members of my graduate committee for their comments and criticism of this dissertation.

My debt to Professor C-T Tai is especially great, not only for suggesting the area for this investigation, but for his continual guidance, criticism, and encouragement.

I want to express my gratitude also to Dr. Dipak Sengupta for the time he has devoted to numerous discussions during the preparation of this manuscript, and to Mr. Joseph Ferris for many helpful discussions and comments relating to the experimental aspects of this work.

In addition, I am indebted to Mr. Peter Wilcox for assistance with many aspects of the computer programs involved in the numerical investigations, and to Mr. Alan Loudon for his help with the experimental measurement work.

Special thanks are due to Mrs. Claire White and to Mrs. Katherine McWilliams for their efforts in the typing and general preparation of this manuscript.

From a personal standpoint, I want to especially acknowledge the support of my wife, Ann, during the years which have led to this thesis.

Finally, a word of thanks to my parents for teaching by word and deed the significance and value of perseverance.

TABLE OF CONTENTS

LIST OF TABLES

LIST OF ILLUSTRATIONS

LIST OF ILLUSTRATIONS
(Continued)

LIST OF ILLUSTRATIONS
(Continued)

LIST OF ILLUSTRATIONS
(Continued)

LIST OF ILLUSTRATIONS
(Continued)

LIST OF ILLUSTRATIONS
(Continued)

LIST OF APPENDICES

I

INTRODUCTION

1.1 General Remarks

The phased array antenna, an old and well-established concept of antenna theory, has drawn increasing attention during the past few years. The renewed interest stems from the flexibility and adaptability of an array and its consequent utility in the areas of beam steerable antennas, pattern synthesis, and signal processing antennas (Allen, 1964, Young and Ksienski, 1961a, Ksienski, 1961b, and Young, 1965).

An array type which has received little attention in the literature to date, is the three-dimensional volume array. A volume array has several potential advantages over other types of antennas in addition to those normally associated with arrays, especially in the frequency bands at, and just below, the microwave range, e.g., the VHF band. For example, at these lower frequencies the cost and size of highly directive antennas, such as the parabolic dish would be extremely great. A volume array of electric dipoles, assuming for the moment that comparable directivity can be so obtained, could very possibly allow a considerable reduction in cost because of the simpler construction methods and materials required. In addition, a reduction in size is also possible, in one sense, due to the possibility of trading off between the three, dimensional parameters of the array. Such a tradeoff is particularly clear in the case where a volume phased array is designed to replace a planar phased array. Such a tradeoff between dimensions could have considerable importance from a practical standpoint. A dimensional tradeoff could also serve to simplify certain aspects of mechanical problems associated with beam scanning if it were desired to mechanically steer the array. However, and more important, the beam scanning function could be shifted from a mechanical problem to an electrical one by utilizing electronic beam steering techniques such as are currently used in linear and planar phased arrays (Allen, 1964, Delaney, 1962, Blass, 1960, Shnitkin, 1960 and Shelton and Kelleher, 1961).

In addition to the properties mentioned above, the volume array would also appear to be a very versatile element for use in a complex signal processing system.

In view of these potential properties, the volume array would seem to be particularly applicable in the areas of radio astronomy, specialized communication systems (e.g. military communication links) and VHF radar.

1.2 Historical Background

The literature related to the true volume array concept is quite meager. Many papers have utilized the concept of a planar array backed by a ground plane, which is in effect a specialized case of a volume array. In this case, the elements are constrained to be in two parallel planes, or to introduce a terminology to be used subsequently, the array can be viewed as consisting of two "stacked decks" of elements. Such examples fail to take advantage of the volume array concept in its general form. To this author's knowledge, the only paper to do otherwise was published by E. J. Sterba (1931).

Sterba's paper presents, without derivation, the expressions for the directivity of certain rectangular configurations of short dipole elements. The one- and two-dimensional cases are given in a general form, but the three-dimensional expression is given only for the case of a unidirectional system, i.e. a two-deck array. Numerical results are presented for the directivity of various types of arrays, mainly as a function of array length for several fixed element spacings, but also for some cases as a function of interelement spacing for several numbers of elements. The limited computational facilities at the time during which this paper was written seem to have resulted in some excessive smoothing of the numerical data and some consequent erroneous conclusions. For example, the family of curves of directivity as a function of interelement spacing for a linear broadside array of parallel elements indicates an optimum spacing limit (as the number of elements increases) of 3/4 λ. As will be shown later, and as was shown by Tai (1963), this result is incorrect.

In addition to the above theoretical work, Sterba quotes one experimental verification of his results. A broadside two-deck planar array, phased for unidirectional (end-fire) radiation was constructed at Deal, New Jersey by the Bell Telephone Laboratories. The array consisted of three collinear tiers of 17 parallel half-wave dipole elements backed by a reflector and operating at 18.3 MHz. The theoretical gain predicted for this antenna was 21.2 db. The actual gain as measured in New Southgate, England, is cited as 21.7 db.

Brief references to the volume array concept occur in several books on antennas. Kraus (1950) discusses the pattern multiplication principle for volume arrays of point sources. He indicates that the volume array concept is an inefficient approach to achieving extremely narrow beamwidth arrays. However, he also mentions that this is not necessarily the case with regard to directivity, and in fact this question is left open. The treatments of the volume array concept by Elliott(Hansen, 1966) and also Wolff (1966) are limited to the pattern multiplication concept. Elliott indicates that no significant change in directivity may be expected from a volume array, a conclusion which seems to be based on his argument concerning beam width reduction.

The above discussions do not consider, however, the added degree of freedom which the depth of the array allows in the overall array design. Specifically, this feature of the array permits variations in the interelement spacings, and a related weighting of the array pattern sidelobe and grating lobe structure as will be shown. These design parameters can in fact have considerable effect on beamwidth and directivity.

1.3 Thesis Objectives

This thesis will undertake to demonstrate two fundamental aspects of the volume array concept. First, and most important, the physical realizability of such an array will be demonstrated by an experimental investigation of a three-dimensional rectangular array of electric dipoles, to be subsequently called the lattice array. The primary goals of this experimental work will be; 1) development of a working model of a lattice array system, 2) verification of theoretically predicted directivity values and radiation patterns for lattice arrays, and 3) qualitative examination of mutual coupling effects in a lattice array. The remaining topic is a detailed theoretical and numerical investigation of the directivity properties of the lattice array. Because of the generality of the results obtained during the theoretical analysis of the directivity of a lattice array, some general results for directivity properties of various types of arrays will also be presented here.

II

AN EXACT EXPRESSION FOR THE DIRECTIVITY OF DIPOLE ARRAYS WITH ARBITRARY ARRAY GEOMETRY

2.1 General Remarks

The expression for the directivity function of phased arrays of short electric dipoles to be derived below, is considered in its most general form. That is, the location, orientation, and excitation of each element in the array remain as parameters of the expression in its final form. After an explicit, exact form has been derived, the general result is reduced to the form appropriate to a three-dimensional lattice array. In view of the generality of the directivity expression, reductions are also made for several other standard array configurations and comparisons are made to known results.

An extension of the result for short dipoles to the long dipole case is given in Appendix A. These results are included for completeness. In practice, the directivity of an array of long dipoles, i.e., length$\sim\frac{\lambda}{2}$, does not differ significantly from that of an array of short (Hertzian) dipoles. This fact is verified by the experimental results of Chapter V, where dipoles of length approaching $\frac{\lambda}{2}$ are used as elements of various types of arrays.

2.2 Directivity of Short Dipole Arrays with Arbitrary Element Location, Orientation and Excitation

2.2.1 Far Field Expression

Consider an array of N short dipoles as shown in Figure 2-1. The location of the dipoles will be described by the coordinate system (R, θ, ϕ) or, equivalently (x, y, z). The origin of this system is within, or in, the vicinity of the region occupied by the array. A set of secondary coordinate systems $(R_i', \theta_i', \phi_i')$ or the equivalent (x_i', y_i', z_i') system, $1 \leq i \leq N$ will be associated with elements of the array, each element of the set corresponding to one array element. The origin of each secondary coordinate system corres-

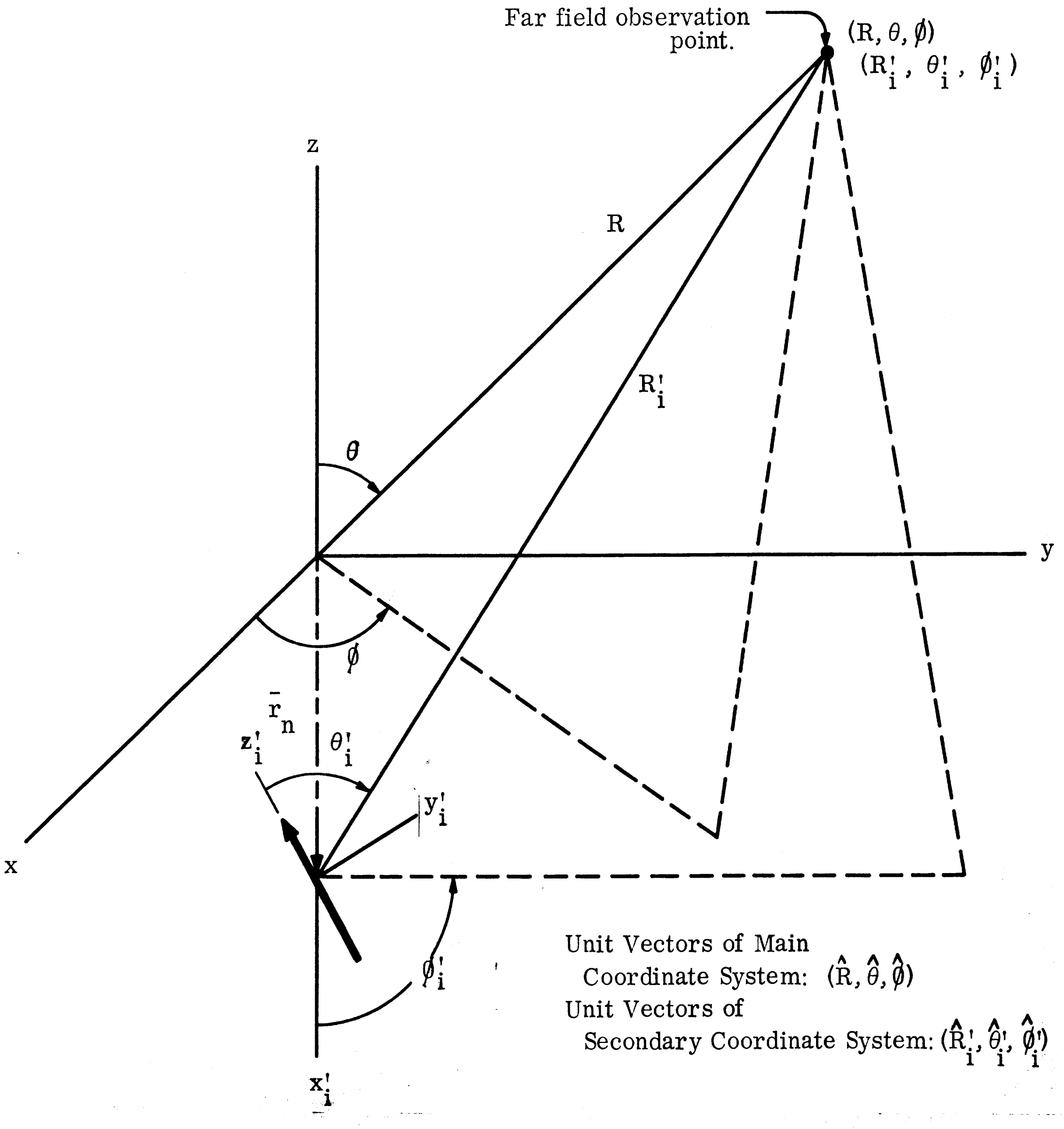

Unit Vectors of Main Coordinate System: $(\hat{R}, \hat{\theta}, \hat{\phi})$

Unit Vectors of Secondary Coordinate System: $(\hat{R}_i', \hat{\theta}_i', \hat{\phi}_i')$

FIG. 2-1: MAIN COORDINATE SYSTEM (R, θ, ϕ) OR (x, y, z) AND REPRESENTATIVE ARRAY ELEMENT WITH ASSOCIATED SECONDARY COORDINATE SYSTEM $(R_i', \theta_i', \phi_i')$ OR (x_i', y_i', z_i').

ponds to the midpoint of its associated dipole element, and the $+z'_i$ axis of the system is coincidental with, and in the direction of, the current element representing the dipole.

In terms of the above notation, a typical dipole element indexed by n ($1 \leq n \leq N$) has; 1) location (x_n, y_n, z_n); 2) orientation (θ_n, ϕ_n) as determined by the current element orientation upon rigid translation of its base to the origin of the (R, θ, ϕ) system); 3) far field

$$\bar{E}_n = V_n e^{j\delta_n} \frac{e^{jkR'_n}}{R'_n} \sin\theta'_n \, \hat{\theta}'_n$$

($V_n e^{j\delta_n}$ being representative of the excitation of the element, R'_n the distance from the midpoint of the dipole to the far-field observation point, and an assumed time dependence $e^{+j\omega t}$).

The far-field of the array is therefore

$$\bar{E} = \sum_{n=1}^{N} \bar{E}_n = \sum_{n=1}^{N} V_n e^{j\delta_n} \frac{e^{-jkR'_n}}{R'_n} \sin\theta'_n \, \hat{\theta}'_n \qquad (2.1)$$

The mixed coordinate notation of this expression can be converted to that of the common system (R, θ, ϕ) by using the relations

$$R'_n = R - \bar{r}_n \cdot \hat{R}$$

where $\bar{r}_n \equiv$ vector position of the n'th dipole, and R is the distance to the far-field observation point from the origin. If $R \gg |\bar{r}_n|$

$$\therefore \frac{1}{R'_n} \doteq \frac{1}{R}$$

and

$$\sin\theta'_n \, \hat{\theta}'_n \doteq \left\{\sin\theta\cos\theta_n - \cos\theta\sin\theta_n\cos(\phi-\phi_n)\right\} \hat{\theta} + \left\{\sin\theta_n\sin(\phi-\phi_n)\right\} \hat{\phi} .$$

Substituting these expressions into (2.1)

$$\bar{E} = \sum_{n=1}^{N} V_n e^{j\delta_n} \frac{e^{-jkR}}{R} e^{+jk\bar{r}_n \cdot \hat{R}} \left\{ \left[\sin\theta\cos\theta_n - \cos\theta\sin\theta\cos(\phi-\phi_n)\right] \hat{\theta} + \left[\sin\theta_n \sin(\phi-\phi_n)\right] \hat{\phi} \right\} . \qquad (2.2)$$

2.2.2 Directivity Function Expression

The expression for the directivity function is

$$D(\theta,\phi) = \frac{\mathcal{U}(\theta,\phi)}{\frac{1}{4\pi}\iint \mathcal{U}(\theta,\phi)d\Omega} \qquad \text{where } d\Omega = \sin\theta\, d\theta\, d\phi$$

where

$$\mathcal{U}(\theta,\phi) = R^2 \left|\bar{S}_{avg}(\theta,\phi)\right| = \frac{R^2}{2\eta_o} \left|\bar{E} \times \hat{R} \times \bar{E}^*\right|$$

is the radiation intensity of the array. with $\eta_o \equiv$ free space impedance $\sqrt{\frac{\mu_o}{\epsilon_o}}$ and $S_{avg} \equiv$ time averaged Poynting Vector.

Therefore, for an arbitrary array, the explicit expression for $\mathcal{U}(\theta,\phi)$ is given by

$$\mathcal{U}(\theta,\phi) = \frac{1}{2\eta_o} \sum_{n=1}^{N} \sum_{m=1}^{M} V_n V_m e^{j(\delta_n-\delta_m)} e^{jk\hat{R}\cdot(\bar{r}_n-\bar{r}_m)}$$

$$\left| \left\{ \left[\sin\theta\cos\theta_n - \cos\theta\sin\theta_n\cos(\phi-\phi_n)\right] \hat{\theta} + \sin\theta_n \sin(\phi-\phi_n)\hat{\phi} \right\} \times \hat{R} \right.$$

$$\left. \times \left\{ \left[\sin\theta\cos\theta_m - \cos\theta\sin\theta_m\cos(\phi-\phi_m)\right] \hat{\theta} + \sin\theta_m \sin(\phi-\phi_m)\hat{\phi} \right\} \right|$$

After carrying out the indicated operations and expanding and collecting appropriate terms, the resulting expression is

$$\mathcal{U}(\theta,\phi) = \frac{1}{2\eta_o} \sum_{n=1}^{N} \sum_{m=1}^{N} V_n V_m e^{j(\delta_n-\delta_m)} e^{jk\hat{R}\cdot(\bar{r}_n-\bar{r}_m)} \mathcal{F}_{nm}(\theta,\phi) \qquad (2.3)$$

where $\mathcal{F}_{nm}(\theta,\phi)$ is to be called the pattern-product function

$$\mathcal{F}_{nm}(\theta,\phi) = A_{nm}+B_{nm}+\left\{-A_{nm}+B_{nm}+C_{nm}\right\}\cos^2\theta + C_{nm}\sin^2\theta\sin^2\phi$$

$$- D_{nm}\sin^2\theta\cos\phi\sin\phi - E_{nm}\cos\theta\sin\theta\cos\phi$$

$$- F_{nm}\cos\theta\sin\theta\sin\phi \ ,$$

and

$$A_{nm} = A_{mn} = \cos\theta_n\cos\theta_m$$

$$B_{nm} = B_{mn} = \sin\theta_n\sin\theta_m\sin\phi_n\sin\phi_m$$

$$C_{nm} = C_{mn} = \sin\theta_n\sin\theta_m\cos(\phi_n+\phi_m)$$

$$D_{nm} = D_{mn} = \sin\theta_n\sin\theta_m\sin(\phi_n+\phi_m)$$

$$E_{nm} = E_{mn} = \sin\theta_n\cos\theta_m\cos\phi_n + \cos\theta_n\sin\theta_m\cos\phi_m$$

$$F_{nm} = F_{mn} = \sin\theta_n\cos\theta_m\sin\phi_n + \cos\theta_n\sin\theta_m\sin\phi_m$$

In the above expression for $\mathcal{U}(\theta,\phi)$(Eq. 2. 3), the following relationship and notation will be introduced.

Since

$$\bar{r}_n-\bar{r}_m=(x_n-x_m)\hat{x}+(y_n-y_m)\hat{y}+(z_n-z_m)\hat{z}$$

and
$$\hat{R}=\sin\theta\cos\phi\,\hat{x}+\sin\theta\sin\phi\,\hat{y}+\cos\theta\,\hat{z}$$

$$\therefore\ \hat{R}\cdot(\bar{r}_n-\bar{r}_m)=(x_n-x_m)\sin\theta\cos\phi+(y_n-y_m)\sin\theta\sin\phi+(z_n-z_m)\cos\theta\ .$$

Let

$$x_{nm}=x_n-x_m=-x_{mn},\quad y_{nm}=y_n-y_m=-y_{mn},\quad z_{nm}=z_n-z_m=-z_{mn}$$

and
$$\delta_{nm}=\delta_n-\delta_m=-\delta_{mn}\quad .$$

In view of this notation, and upon appropriately combining terms

$$\mathcal{U}(\theta,\phi)=\frac{1}{2\eta_0}\sum_{n=1}^{N}\sum_{m=1}^{N}V_nV_m\cos(x_{nm}k\sin\theta\cos\phi+y_{nm}k\sin\theta\sin\phi$$

$$+z_{nm}k\cos\theta+\delta_{nm})\,\mathcal{F}_{nm}(\theta,\phi)\ . \tag{2.4}$$

2.2.3 Evaluation of Total Radiated Power.

The integration of $\mathcal{U}(\theta, \phi)$, (resulting in total power radiated) is relatively straightforward and results in the form

$$\frac{1}{4\pi}\iint \mathcal{U}(\theta, \phi)\, d\Omega = \frac{1}{2\eta_0}\sum_{n=1}^{N}\sum_{m=1}^{N} V_n V_m I_{nm}$$

with

$$I_{nm} = \sum_{i=1}^{6} \vartheta_i^{nm}$$

where

$$\vartheta_i^{nm} = \frac{1}{4\pi}\int_0^{\pi}\int_0^{2\pi} \cos(w_{nm} k \sin\theta \sin(\phi+\xi_{nm})+z_{nm} k \cos\theta+\delta_{nm}) f_i^{nm}(\theta, \phi)\, d\Omega$$

with

$$w_{nm} = \left[x_{nm}^2 + y_{nm}^2\right]^{1/2}$$

$$\xi_{nm} = \tan^{-1}\left\{\frac{x_{nm}}{y_{nm}}\right\} \qquad (\xi_{nm} \equiv 0 \quad \text{when} \quad w_{nm} = 0)$$

$$f_1^{nm}(\theta, \phi) = A_{nm} + B_{nm}$$

$$f_2^{nm}(\theta, \phi) = (-A_{nm} + B_{nm} + C_{nm})\cos^2\theta$$

$$\vdots$$

and

$$\mathcal{F}_{nm}(\theta, \phi) = \sum_{i=1}^{6} f_i^{nm}(\theta, \phi) .$$

Evaluation of the terms ϑ_i^{nm} follows rather directly if one makes use of the periodic properties of the integrands and performs coordinate transformations of the type used in problems on the geometry of the sphere (Watson, 1944), i.e., permutations of direction cosines while integrating over a fixed spherical cap. An example illustrating the method is given in Appendix B. After performing the indicated integrations, and then appropriately collecting terms, one obtains

[redacted]

$$\frac{1}{4\pi}\iint \mathcal{U}(\theta,\phi)\,d\Omega = \frac{1}{2\eta_o}\sum_{n=1}^{N}\sum_{m=1}^{N} V_n V_m \cos\delta_{nm} \left\{\sum_{w=0}^{1} j_w(k\rho_{nm})\,G_w(k\rho_{nm},\mu_{nm},\xi_{nm})\right\} \tag{2.5}$$

where $j_w(k\rho_{nm})$ are spherical Bessel functions and

$$\rho_{nm} = \left\{w_{nm}^2 + z_{nm}^2\right\}^{1/2} = \left\{x_{nm}^2 + y_{nm}^2 + z_{nm}^2\right\}^{1/2}$$

$$\mu_{nm} = \tan^{-1}\left\{\frac{z_{nm}}{w_{nm}}\right\} = \tan^{-1}\left\{\frac{z_{nm}}{(x_{nm}^2 + y_{nm}^2)^{1/2}}\right\}$$

with $\mu_{nm} \equiv 0$ when $\rho_{nm} \equiv 0$ and ξ_{nm} as defined previously

$$G_o(k\rho_{nm}, \mu_{nm}, \xi_{nm}) = \cos^2\mu_{nm}\left\{A_{nm} - B_{nm} - C_{nm}\sin^2\xi_{nm} - \frac{D_{nm}}{2}\sin 2\xi_{nm}\right\}$$

$$- \frac{\sin 2\mu_{nm}}{2}\left\{E_{nm}\sin\xi_{nm} + F_{nm}\cos\xi_{nm}\right\} + 2B_{nm} + C_{nm}$$

$$G_1(k\rho_{nm}, \mu_{nm}, \xi_{nm}) = \frac{1}{k\rho_{nm}}\Bigg[\cos^2\mu_{nm}\Bigg\{3(-A_{nm} + B_{nm} + C_{nm}\sin^2\xi_{nm})$$

$$+ \frac{D_{nm}}{2}(1 + 2\sin 2\xi_{nm})\Bigg\} + \frac{3}{2}\sin 2\mu_{nm}(E_{nm}\sin\xi_{nm} + F_{nm}\cos\xi_{nm})$$

$$+ 2\left\{A_{nm} - B_{nm}\right\} - C_{nm}\Bigg]$$

2.2.4 The Exact, Explicit Expression for Directivity

Using all the above results, the exact expression for the directivity of an array of short dipoles with arbitrary array geometry is obtained:

$$D(\theta,\phi)=\frac{\sum_{n=1}^{N}\sum_{m=1}^{N} V_n V_m \cos\left(kx_{nm}\ \text{[illegible]}\ ky_{nm}\sin\theta\sin\phi+kz_{nm}\cos\theta+\delta_{nm}\right)\mathcal{F}_{nm}(\theta,\phi)}{\sum_{n=1}^{N}\sum_{m=1}^{N} V_n V_m \cos\delta_{nm}\left\{\sum_{w=0}^{1} j_w(k\rho_{nm})G_w(k\rho_{nm},\mu_{nm},\xi_{nm})\right\}} \tag{2.6}$$

2.3 Special Cases

2.3.1 A Linear Broadside Array of Parallel Short Dipoles

Consider a linear array of N short dipoles positioned along the z axis with center to center spacing $z_i-z_{i-1}=c$, oriented parallel to the y axis. The first element is centered at (0, 0, 0) The parameters of the directivity expression for this array are:

$$\theta_n=\frac{\pi}{2},\quad \phi_n=\frac{\pi}{2},\quad x_{nm}=y_{nm}=0,\quad z_{nm}=(n-m)c$$

or equivalently,

$$w_{nm}=0,\ \rho_{nm}=(n-m)c$$

$$A_{nm}=D_{nm}=E_{nm}=F_{nm}=0,\quad B_{nm}=+1,\quad C_{nm}=-1$$

$$\mu_{nm}=\begin{cases}+\frac{\pi}{2} & \text{if } n>m\\ 0 & \text{if } n=m\\ -\frac{\pi}{2} & \text{if } n<m\end{cases}\qquad \xi_{nm}=0$$

$$V_n=V,\ \delta_{nm}=0$$

$$\therefore D(\theta,\phi) = \frac{\sum_{n=1}^{N}\sum_{m=1}^{N} \cos(\left\{n-m\right\} ck\cos\theta)\left[1-\sin^2\theta\sin^2\phi\right]}{\sum_{n=1}^{N}\sum_{m=1}^{N}\left\{j_0(\left\{n-m\right\}ck)\left[1-\cos^2\mu_{nm}\right]+j_1(\left\{n-m\right\}ck)\frac{1}{\left\{(n-m)ck\right\}}\cdot\left[3\cos^2\mu_{nm}-1\right]\right\}}.$$

This expression may be simplified by expanding the indicated double sums, introducing the numerical values of μ_{nm}, introducing the index p=n-m, and then collecting similar terms. After performing these manipulations, one finds,

$$D(\theta,\phi) = \frac{\left\{1+2\sum_{p=1}^{N-1}(1-\frac{p}{N})\cos(pck\cos\theta)\right\}\left\{1-\sin^2\theta\sin^2\phi\right\}}{\frac{2}{3}+2\sum_{p=1}^{N-1}(1-\frac{p}{N})\left\{j_0(pck)-j_1(pck)\frac{1}{(pck)}\right\}}$$

The maximum directivity is, therefore,

$$D_{max} = \frac{\frac{3}{2}N}{1+3\sum_{p=1}^{N-1}(1-\frac{p}{N})(j_0(pck)-j_1(pck)\frac{1}{(pck)})},$$

with the directions of the two identical maxima being along the $\pm$ x axes, i.e., $\theta = \pi/2,\ \phi = \left\{0,\ \pi\right\}$.

2.3.2 A Linear Broadside Array of Collinear Short Dipoles

Consider a linear array of N short dipoles positioned and oriented along the + z axis. Let the element spacing, center to center, be "c" and the first element centered at (0, 0, 0). The parameters of the directivity expression for this array are:

$$\theta_n = 0, \quad \phi_n \equiv 0$$

$$x_{nm} = y_{nm} = 0, \quad z_{nm} = (n-m)c$$

or equivalently, $w_{nm} = 0, \quad \rho_{nm} = (n-m)c$

$$A_{nm} = +1, \quad B_{nm} = C_{nm} = D_{nm} = E_{nm} = F_{nm} = 0$$

$$\mu_{nm} = \begin{cases} +\frac{\pi}{2} \text{ if } n > m \\ 0 \text{ if } n = m \\ -\frac{\pi}{2} \text{ if } n < m \end{cases} \qquad \xi_{nm} \equiv 0$$

$$V_n = V, \quad \delta_{nm} = 0$$

$$\therefore \quad D(\theta, \phi) = \frac{\sum_{n=1}^{N} \sum_{m=1}^{N} \cos(\{n-m\} kc \cos\theta) \left[1 - \cos^2\theta\right]}{\sum_{n=1}^{N} \sum_{m=1}^{N} \left\{ j_0(\{n-m\} ck) \cos^2 \mu_{nm} + j_1(\{n-m\} ck) \frac{1}{((n-m)ck)} \cdot \left[2 - 3\cos^2 \mu_{nm}\right] \right\}}.$$

Proceeding as in Section 2. 3. 1, one finds

$$D(\theta, \phi) = \frac{\left\{1 + 2 \sum_{p=1}^{N-1} (1 - \frac{p}{N}) \cos(pck \cos\theta)\right\} \sin^2\theta}{\frac{2}{3} + 2 \sum_{p=1}^{N-1} (1 - \frac{p}{N}) j_1 (pck) \frac{2}{(pck)}}$$

The maximum directivity is, therefore

$$D_{max} = \frac{\frac{3}{2}N}{1+6\sum_{p=1}^{N-1}(1-\frac{p}{N})j_1(pck)\frac{1}{(pck)}}$$

in the plane $\theta = \frac{\pi}{2}$.

2.3.3 A Linear End-fire Array of Parallel Short Dipoles.

The parameters of this array are identical with those of the array of Section 2.3.1 with the exception of δ_{nm}. Let $\delta_{nm} = + (n-m)\ kc$ so that the maximum radiation is in the -z direction. Substituting the parameters into $D(\theta,\phi)$, and performing the simplifications indicated before, one obtains

$$D(\theta, \phi) = \frac{\left\{1+2\sum_{p=1}^{N-1}(1-\frac{p}{N})\cos\left\{pck\,(1+\cos\theta)\right\}\right\}\left[1-\sin^2\theta\sin^2\phi\right]}{\frac{2}{3}+2\sum_{p=1}^{N-1}(1-\frac{p}{N})\cos(pck)\left\{j_0(pck)-j_1(pck)\frac{1}{(pck)}\right\}} .$$

The maximum directivity is therefore ,

$$D_{max} = \frac{\frac{3}{2}N}{1+3\sum_{p=1}^{N-1}(1-\frac{p}{N})\cos(pck)\left\{j_0(pck)-j_1(pck)\frac{1}{(pck)}\right\}} .$$

and occurs in the direction of the -z axis, i.e., $\theta = \pi$.

The results of this and the preceding two sections are identical with those given by Tai (1963) except for the notation used. Here, the standard notation for spherical Bessel functions is used in place of Tai's p, ℓ, and q functions.

2.3.4 A Rectangular Broadside Planar Array of Short Dipoles.

Consider an array of short dipoles, with the dipoles centered at the intersection points of a rectangular grid in the x-z plane with grid lines parallel to the x and z axes. The elements of the grid have spacing "a" along the x-axis and spacing "c" along the z-axis. The grid is centered on the origin (0, 0, 0) and has dimensions (L-1) a x (N-1)c. There are L· N dipole elements in the array, and all elements are aligned in the +z direction.

Statement of the parameters of the directivity expression is facilitated, and simplifications in $D(\theta,\phi)$ easier to visualize, if the running index on the dipole elements, n, is changed to a double index (i, k). The elements of the double index (i, k) correspond to a matrix type indexing with "i" referring to an indexing along the x-axis, and "k" an indexing along the z-axis. Carrying out this change in indexing;

$$n \rightarrow (i, k) \text{ and } m \rightarrow (i', k') \text{ where } 1 \leq i \leq L, \quad 1 \leq k \leq N \ .$$

The index pairs (i, k) and (i', k') will be represented by "p" and "q" respectively for clarity of notation.

In terms of the new matrix indexing, the parameters of the directivity expression for the array are:

$$x_{pq} = (i - i')\,a, \quad y_{pq} = 0, \quad z_{pq} = (k - k')\,c$$

or equivalently,

$$w_{pq} = (i - i')\,a$$

$$\rho_{pq} = \sqrt{(i - i')^2 a^2 + (k - k')^2 c^2}$$

$$A_{pq} = +1, \quad B_{pq} = C_{pq} = D_{pq} = E_{pq} = F_{pq} = 0$$

$$\mu_{pq} = \tan^{-1}\left\{\frac{x_{pq}}{w_{pq}}\right\} = \tan^{-1}\left\{\frac{(k - k')\,c}{(i - i')\,a}\right\}$$

$$\xi_{pq} = \tan^{-1}\left\{\frac{x_{pq}}{y_{pq}}\right\} = \begin{cases} +\frac{\pi}{2} & \text{if } i > i' \\ -\frac{\pi}{2} & \text{if } i < i' \end{cases}$$

Introducing these parameter values and their indexing into the expression for $D(\theta,\phi)$, expanding the indicated sums, and then introducing the variables $\ell=i-i'$, $n=k-k'$ (with the result that $\mu_{pq}=\tan^{-1}\frac{nc}{\ell a}\equiv\mu_{\ell n}$) and collecting similar terms (the number of each type of term can be determined from simple geometric considerations involving the array geometry), the resulting expression for the directivity of the array is:

$$D(\theta,\phi)=\frac{\left\{1+2\sum_{\ell=1}^{L-1}\left(1-\frac{\ell}{L}\right)\cos\left(\beta_{\ell,0}\sin\theta\cos\phi\right)+2\sum_{n=1}^{N-1}\left(1-\frac{n}{N}\right)\cos\left(\beta_{0,n}\cos\theta\right)+4\sum_{\ell=1}^{L-1}\sum_{n=1}^{N-1}\left(1-\frac{\ell}{L}\right)\left(1-\frac{n}{N}\right)\cos\left(\beta_{\ell,0}\sin\theta\cos\phi\right)\cos\left(\beta_{0,n}\cos\theta\right)\right\}\sin^2\theta}{\frac{2}{3}+2\sum_{\ell=1}^{L-1}\left(1-\frac{\ell}{L}\right)\left\{j_0(\beta_{\ell,0})-j_1(\beta_{\ell,0})\frac{1}{\beta_{\ell,0}}\right\}+2\sum_{n=1}^{N-1}\left(1-\frac{n}{N}\right)\left\{2j_1(\beta_{0,n})\frac{1}{\beta_{0,n}}\right\}+4\sum_{\ell=1}^{L-1}\sum_{n=1}^{N-1}\left(1-\frac{\ell}{L}\right)\left(1-\frac{n}{N}\right)\left\{j_0(\beta_{\ell,n})\cos^2\mu_{\ell n}+j_1(\beta_{\ell,n})\left(\frac{2-3\cos^2\mu_{\ell n}}{\beta_{\ell,n}}\right)\right\}}$$

where $\beta_{\ell,n}=k\left[(\ell a)^2+(nc)^2\right]^{1/2}$.

This expression achieves a maximum for $\theta=\frac{\pi}{2}$; $\phi=\left\{\pi/2,\ 3\pi/2\right\}$ with the maximum being

$$D_{max}=\frac{3}{2}LN\Big/\left[1+3\sum_{\ell=1}^{L-1}\left(1-\frac{\ell}{L}\right)\left\{j_0(\beta_{\ell,0})-j_1(\beta_{\ell,0})\frac{1}{\beta_{\ell,0}}\right\}+3\sum_{n=1}^{N-1}\left(1-\frac{n}{N}\right)\left\{2j_1(\beta_{0,n})\frac{1}{\beta_{0,n}}\right\}+6\sum_{\ell=1}^{L-1}\sum_{n=1}^{N-1}\left(1-\frac{\ell}{L}\right)\left(1-\frac{n}{N}\right)\left\{j_0(\beta_{\ell,n})\cos^2\mu_{\ell,n}+j_1(\beta_{\ell,n})\left(\frac{2-3\cos^2\mu_{\ell,n}}{\beta_{\ell,n}}\right)\right\}\right]$$

2.3.5 A Three-Dimensional Lattice Array of Short Dipoles.

Consider an array of short dipoles with the dipole elements centered at the intersection points of a three-dimensional grid, the grid lines being parallel to the x, y, and z axes. The elements of the grid have spacing "a" along the x-axis, "b" along the y-axis and "c" along the z-axis. The grid is centered at (0, 0, 0), and has dimensions $(L-1)a \times (M-1)b \times (N-1)c$ in the x, y, z directions respectively. There are $L \cdot M \cdot N$ dipole elements in the array and all elements are aligned in the +z direction.

As in Section 2.3.4, an index change is desirable to facilitate the statement of the parameter values of the directivity function of the array, and in order to better visualize the simplifications which may be made in $D(\theta,\phi)$. In this case, the running index "n" is changed to the triple index (i, j, k) which corresponds to indexing along the x, y and z axes respectively. Carrying out such a change,

$$n \rightarrow (i, j, k) \qquad\qquad m \rightarrow (i', j', k')$$

where

$$1 \leq i \leq L, \qquad 1 \leq j \leq M, \qquad 1 \leq k \leq N \ .$$

Again for notational efficiency, let the triples, (i, j, k) and (i', j', k') be represented by "p" and "q" respectively. In terms of this new indexing, the parameters of the directivity function of the array are:

$$x_{pq} = (i-i')a; \qquad y_{pq} = (j-j')b; \qquad z_{pq} = (k-k')c$$

or equivalently

$$w_{pq} = \left[(i-i')^2 a^2 + (j-j')^2 b^2\right]^{1/2}$$

$$\rho_{pq} = \left[(i-i')^2 a^2 + (j-j')^2 b^2 + (k-k')^2 c^2\right]^{1/2}$$

$$\mu_{pq} = \tan^{-1}\left\{\frac{z_{pq}}{w_{pq}}\right\} = \tan^{-1}\left\{\frac{(k-k')c}{\left[(i-i')^2 a^2 + (j-j')^2 b^2\right]^{1/2}}\right\}$$

$$\xi_{pq} = \tan^{-1}\left\{\frac{x_{pq}}{y_{pq}}\right\} = \tan^{-1}\left\{\frac{(i-i')a}{(j-j')b}\right\}$$

$$A_{pq} = +1$$

$$B_{pq} = C_{pq} = D_{pq} = E_{pq} = F_{pq} = 0$$

$$\delta_{pq} = -(j-j')\, bk\, .$$

It is to be noted that this choice of excitation phase results in broadside operation for each set of elements contained in a plane parallel to the x-z plane, and in endfire operation of elements in successive planes parallel to the x-z plane, i.e., maximum radiation along the + y axis. Introducing this indexing into the expression for $D(\theta,\phi)$, expanding the indicated sums, and then introducing the variables

$$\ell = i-i', \quad m = j-j', \quad n = k-k'$$

results in

$$\mu_{pq} = \tan^{-1}\left\{\frac{nc}{\left[(\ell a)^2+(mb)^2\right]^{1/2}}\right\} \equiv \mu_{\ell mn}$$

$$\xi_{pq} = \tan^{-1}\left\{\frac{\ell a}{mb}\right\} \equiv \xi_{\ell m}$$

$$\delta_{pq} = m\, b\, k \equiv \delta_{m}$$

after collecting similar terms (the number of terms having identical forms again being determined from simple geometric considerations involving the array geometry). The resulting expression for the directivity of the array is:

$$D(\theta, \phi) = \frac{S_N(\theta, \phi)}{S_D} \quad \text{where}$$

$$S_N(\theta, \phi) = \Bigg\{ 1+2\sum_{\ell=1}^{L-1}(1-\frac{\ell}{L})\cos(\beta_{\ell,0,0}\sin\theta\cos\phi)+2\sum_{M=1}^{M-1}(1-\frac{m}{M})\cos(\beta_{0,m,0}\big[\sin\theta\sin\phi-1\big])$$

$$+2\sum_{n=1}^{N-1}(1-\frac{n}{N})\cos(\beta_{0,0,n}\cos\theta)+4\sum_{\ell=1}^{L-1}\sum_{m=1}^{M-1}(1-\frac{\ell}{L})(1-\frac{m}{M})\cos(\beta_{\ell,0,0}\sin\theta\cos\phi)\cos(\beta_{0,m,0}\big[\sin\theta\sin\phi+1\big])$$

$$+4\sum_{m=1}^{M-1}\sum_{n=1}^{N-1}(1-\frac{m}{M})(1-\frac{n}{N})\cos(\beta_{0,m,0}\big[\sin\theta\sin\phi-1\big])\cos(\beta_{0,0,n}\cos\theta)$$

$$+4\sum_{\ell=1}^{L-1}\sum_{n=1}^{N-1}(1-\frac{\ell}{L})(1-\frac{n}{N})\cos(\beta_{\ell,0,0}\sin\theta\cos\phi)\cos(\beta_{0,0,n}\cos\theta)$$

$$+8\sum_{\ell=1}^{L-1}\sum_{m=1}^{M-1}\sum_{n=1}^{N-1}(1-\frac{\ell}{L})(1-\frac{m}{M})(1-\frac{n}{N})\cos(\beta_{\ell,0,0}\sin\theta\cos\phi)\cos(\beta_{0,m,0}\big[\sin\theta\sin\phi-1\big])\cos(\beta_{0,0,n}\cos\theta)\Bigg\}\ \sin^2\theta$$

and

$$S_D = \frac{2}{3}+2\sum_{\ell=1}^{L-1}(1-\frac{\ell}{L})\left\{j_0(\beta_{\ell,0,0})-j_1(\beta_{\ell,0,0})\frac{1}{\beta_{\ell,0,0}}\right\}+2\sum_{m=1}^{M-1}(1-\frac{m}{M})\cos(\beta_{0,m,0})\left\{j_0(\beta_{0,m,0})-j_1(\beta_{0,m,0})\frac{1}{\beta_{0,m,0}}\right\}$$

$$+2\sum_{n=1}^{N-1}(1-\frac{n}{N})\left\{2j_1(\beta_{0,0,n})\frac{1}{\beta_{0,0,n}}\right\}+4\sum_{\ell=1}^{L-1}\sum_{m=1}^{M-1}(1-\frac{\ell}{L})(1-\frac{m}{M})\cos(\beta_{0,m,0})\left\{j_0(\beta_{\ell,m,0})-j(\beta_{\ell,m,0})\frac{1}{\beta_{\ell,m,0}}\right\}+$$

$$+4\sum_{m=1}^{M-1}\sum_{n=1}^{N-1}(1-\frac{m}{M})(1-\frac{n}{N})\cos(\beta_{0,m,0})\left\{j_0(\beta_{0,m,n})\cos^2\mu_{0,m,n}+j_1(\beta_{0,m,n})\left(\frac{2-3\cos^2\mu_{0,m,n}}{\beta_{0,m,n}}\right)\right\}$$

$$+4\sum_{\ell=1}^{L-1}\sum_{n=1}^{N-1}(1-\frac{\ell}{L})(1-\frac{n}{N})\left\{j_0(\beta_{\ell,0,n})\cos^2\mu_{\ell,0,n}+j_1(\beta_{\ell,0,n})\left(\frac{2-3\cos^2\mu_{\ell,0,n}}{\beta_{\ell,0,n}}\right)\right\}$$

$$+8\sum_{\ell=1}^{L-1}\sum_{m=1}^{M-1}\sum_{n=1}^{N-1}(1-\frac{\ell}{L})(1-\frac{m}{M})(1-\frac{n}{N})\cos(\beta_{0,m,0})\left\{j_0(\beta_{\ell,m,n})\cos^2\mu_{\ell,m,n}+j_1(\beta_{\ell,m,n})\left(\frac{2-3\cos^2\mu_{\ell,m,n}}{\beta_{\ell,m,n}}\right)\right\}$$

where $\beta_{\ell,m,n}=k\left[(\ell a)^2+(mb)^2+(nc)^2\right]^{1/2}$. The maximum directivity occurs in the direction of the +y axis.

The value of this maximum is:

$$D_{max}=\frac{3}{2}LMN\Big/\left[1+3\sum_{\ell=1}^{L-1}(1-\frac{\ell}{L})\left\{j_0(\beta_{\ell,0,0})-j_1(\beta_{\ell,0,0})\frac{1}{\beta_{\ell,0,0}}\right\}\right.$$

$$+3\sum_{m=1}^{M-1}(1-\frac{m}{M})\cos(\beta_{0,m,0})\left\{j_0(\beta_{0,m,0})-j_1(\beta_{0,m,0})\frac{1}{\beta_{0,m,0}}\right\}$$

$$+3\sum_{n=1}^{N-1}(1-\frac{n}{N})\left\{2j_1(\beta_{0,0,n})\frac{1}{\beta_{0,0,n}}\right\}\quad +$$

$$+6\sum_{\ell=1}^{L-1}\sum_{m=1}^{M-1}\left(1-\frac{\ell}{L}\right)\left(1-\frac{m}{M}\right)\cos(\beta_{0,m,0})\left\{j_0(\beta_{\ell,m,0})-j_1(\beta_{\ell,m,0})\,\frac{1}{\beta_{\ell,m,0}}\right\}$$

$$+6\sum_{m=1}^{M-1}\sum_{n=1}^{N-1}\left(1-\frac{m}{M}\right)\left(1-\frac{n}{N}\right)\cos(\beta_{0,m,0})\left\{j_0(\beta_{0,m,n})\cos^2\mu_{0,m,n}+j_1(\beta_{0,m,n})\left(\frac{2-3\cos^2\mu_{0,m,n}}{\beta_{0,m,n}}\right)\right\}$$

$$+6\sum_{\ell=1}^{L-1}\sum_{n=1}^{N-1}\left(1-\frac{\ell}{L}\right)\left(1-\frac{n}{N}\right)\left\{j_0(\beta_{\ell,0,n})\cos^2\mu_{\ell,0,n}+j_1(\beta_{\ell,0,n})\left(\frac{2-3\cos^2\mu_{\ell,0,n}}{\beta_{\ell,0,n}}\right)\right\}$$

$$+12\sum_{\ell=1}^{L-1}\sum_{m=1}^{M-1}\sum_{n=1}^{N-1}\left(1-\frac{\ell}{L}\right)\left(1-\frac{m}{M}\right)\left(1-\frac{n}{N}\right)\cos(\beta_{0,m,0})\left\{j_0(\beta_{\ell,m,n})\cos^2\mu_{\ell,m,n}\right.$$

$$\left.+j_1(\beta_{\ell,m,n})\left(\frac{2-3\cos^2\mu_{\ell,m,n}}{\beta_{\ell,m,n}}\right)\right\}\Bigg]\;.$$

III

NUMERICAL RESULTS

3.1 General Discussion

The general theoretical expression for the directivity of arrays of short dipoles with arbitrary array geometry derived in Chapter II (Eq. 2.6) provides the opportunity for considering the problem of maximization of the nominal directivity of such an array. Unfortunately, this maximization problem is not feasible from a purely analytical standpoint due to the complexity of the system of nonlinear equations which result from such an approach In view of this difficulty, a direct numerical investigation was attempted.

The specific problem chosen for analysis was the following: Consider a fixed number of elementary radiators arranged in rectangular array geometry. (The one, two, and three dimensional cases are considered independently of one another.) The number of elements arranged along each coordinate axis of the array is fixed, and the interelement spacing along an axis is uniform (see Fig. 3-1). For what values of interelement spacings is the nominal directivity of such an array maximized, and what is the maximum value achieved? (The maximum nominal directivity is defined as the maximum of directive gain considered as a function of interelement spacing for uniform excitation with progressive phasing of elements, as discussed by Tai (1964).)

The directivity expressions for rectangular array geometries in one, two, and three dimensions are given in Chapter II. Since these expressions are functions of at most three variables, they are considerably simpler to investigate than the general directivity expression for arbitrary array configurations which, for an N element array, must be considered as a function of 3N variables. For this reason, and because of their practical significance, uniformly spaced (in any one coordinate direction) rectangular array configurations, were chosen for investigation.

The maximum value achieved by the directivity function will be designated as the maximum nominal directivity, as mentioned above, and denoted by the symbol $\hat{D}$. The element spacings at which $\hat{D}$ occurs will be called the optimum spacing values.

MISSING
PAGE

The goal of the numerical investigation is to obtain values of $\hat{D}$ and optimum element spacings for the various arrays of interest. In addition to these principal results, it is also of interest to obtain some ranges of element spacings, expecially in the vicinity of the point at which the value $\hat{D}$ is achieved. This latter information indicates the sensitivity of the maximum nominal directivity value to slight variations in the values of the element spacing variables. Such sensitivity is of considerable practical interest. A very large value of $\hat{D}$ might have little practical significance if its sensitivity to changes in the effective element spacings is very large.

In addition to the computations carried out during the directivity maximization study, a computer program was written to obtain theoretical radiation patterns for the "E" and "H" plane pattern cuts for the types of arrays mentioned above. These patterns are of interest for several reasons, the principal one being the need for theoretical patterns for comparison with experimental results obtained later. In addition, these patterns provided information needed for determining the gain-beamwidth product under the condition of maximum nominal directivity, for two and three dimensional arrays. Information on the pattern sidelobe behavior under this constraint is also of interest.

3.2 Computer Search Program Design

The directivity expressions for one dimensional, or linear, arrays of uniformly spaced elements presents the simplest possible maximization problem. These expressions, being functions of a single variable, can be evaluated in a straightforward manner without using excessive computer time, and the computer programs involved are relatively simple. Extensive numerical results for this case were published by Tai (1964) for the several types of linear arrays including the cases of isotropic, short dipole, and crossed short dipole sources.

Although somewhat repetitive in terms of the above published results, calculations were carried out here for the linear array cases in order to obtain some experience with this type of computation in its simplest form. In addition, it was desirable to obtain extensions of some of Tai's calculations for comparison with certain results for arrays of higher dimensions.

The computation problem for two and three dimensional arrays becomes considerably more complex than for the one dimensional case. The reason for this increased complexity is the so called "curse of dimensionality", i.e., the extremely rapid increase in computation time for optimization problems as the number of independent variables of the problem increases.

Based upon the results obtained for linear arrays, and general intuition, it was not apparent that the directivity functions for two and three dimensional arrays are, a prior, unimodal, i.e., possess a unique global maximum without local maxima, or do not exhibit "ridge" behavior. Without knowledge of such functional surface characteristics, the standard maximization search methods, i.e., gradient methods, simplex methods, etc., are not practicable. In view of this fact, and the results desired from the computations (Section 3.1), a simple exhaustive type search procedure was devised to examine the directivity function for a fairly wide range of the independent variables.

For two dimensional arrays, the computer program was organized along the following lines. Input data to the program specified ranges for;

1) the two independent spacing variables; and

2) the initial resolution limit, i.e., minimum incremental steps for the independent variables. Given this and other data on the number of elements in the array and the desired minimum, function resolution, the program first computes the value of the directivity function at the intersection points of a grid covering an area of the element-spacing plane determined by (1), with the minimum spacing of parallel grid lines being

determined by (2). Then, based on the results of these calculations, an identical computation procedure for the intersection points of a smaller grid with half the initial resolution limit is carried out. This new grid is centered on the maximum value found during the first set of calculations. This process is repeated until the specified degree of resolution of the directivity function is obtained.

All of the computed directivity values are printed out in the form of rectangular grids corresponding to the region of the element-spacing plane for which the calculations were performed. Such output data are directly interpretable as contour maps of the particular directivity function. A subroutine sorting procedure incorporated into the program was designed to yield output data corresponding to cross-section profiles of the directivity surface through the maximum point.

The computation program for the three dimensional array involves a search of a region of the three dimensional element-spacing space corresponding to a rectangular parallelepiped. The search procedure was organized in a manner similar to that of the two dimensional search program and can best be explained by appealing to a geometric representation. The region of the three dimensional element-spacing space which is of interest is determined by specifying as input data a range for each of the three element spacing variables. Then, as specified by other input data, planar cross sections of this region are examined as in the two dimensional search program. Such planar cross sections are taken normal to the element-spacing axis which corresponds to spacing of progressively phased array elements. The resolution of the directivity function along this axis, i.e., the spacing between planar cross section cuts, is specified as input data for this first set of computations. Based on the largest maximum directivity value computed in any cross sectional cut, a smaller region (again a rectangular parallelepiped) is defined, centered on the location of that maximum value. Cross sectional cuts of this region are then made as in the first stage of the search procedure, with the increment between cuts being half as large as in the previous stage of the search. This procedure is then repeated until the desired resolution of the directivity function along the axis normal to the cross sectional cuts is obtained.

At each stage of the search, all directivity values which have been computed are read out in the same form as for the two dimensional case, with the exception of the cross section profile data. The output data are again interpretable as contour maps, but each contour map must now be labled to indicate its position within the rectangular parallelepiped region being searched.

The contour maps resulting from the output format of these computer programs achieve the goals of the maximization study as discussed in Section 3.1. Not only are the value and coordinates of the maximum directivity point determined, but the general functional behavior of the directivity function is displayed over a range of the function variables, with increasing detail in the vicinity of the maximum value point.

Using geometric terminology, the highest point of the surface (hypersurface) defined by the directivity function of the two (three) dimensional array is determined. In addition, the behavior of the entire surface (hypersurface) within the limits imposed by input data is determined, with the surface (hypersurface) resolution increasing as the surface (hypersurface) high point is approached.

3.3 Directivity Properties of Planar Arrays

Examples of the contour maps derived from the search program for two dimensional arrays are shown in Figs. 3-2 through 3-5 for several array sizes. The values given for the various contour lines, or level curves, are expressed in percent of the maximum value $\hat{D}$. Each such value gives the upper bound on

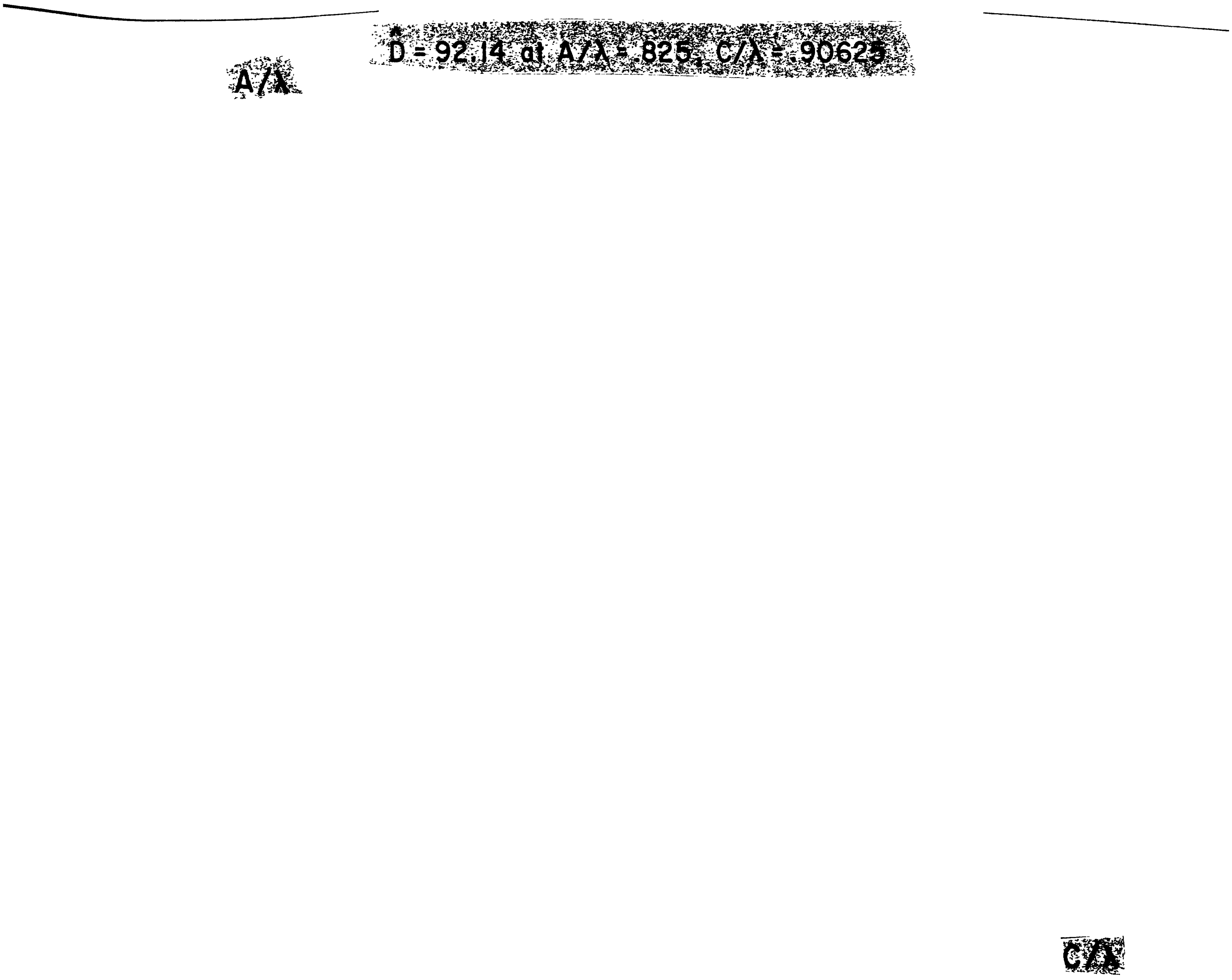

FIG. 3-2: CONTOUR MAP - DIRECTIVITY OF 5 x 5 PLANAR ARRAY.

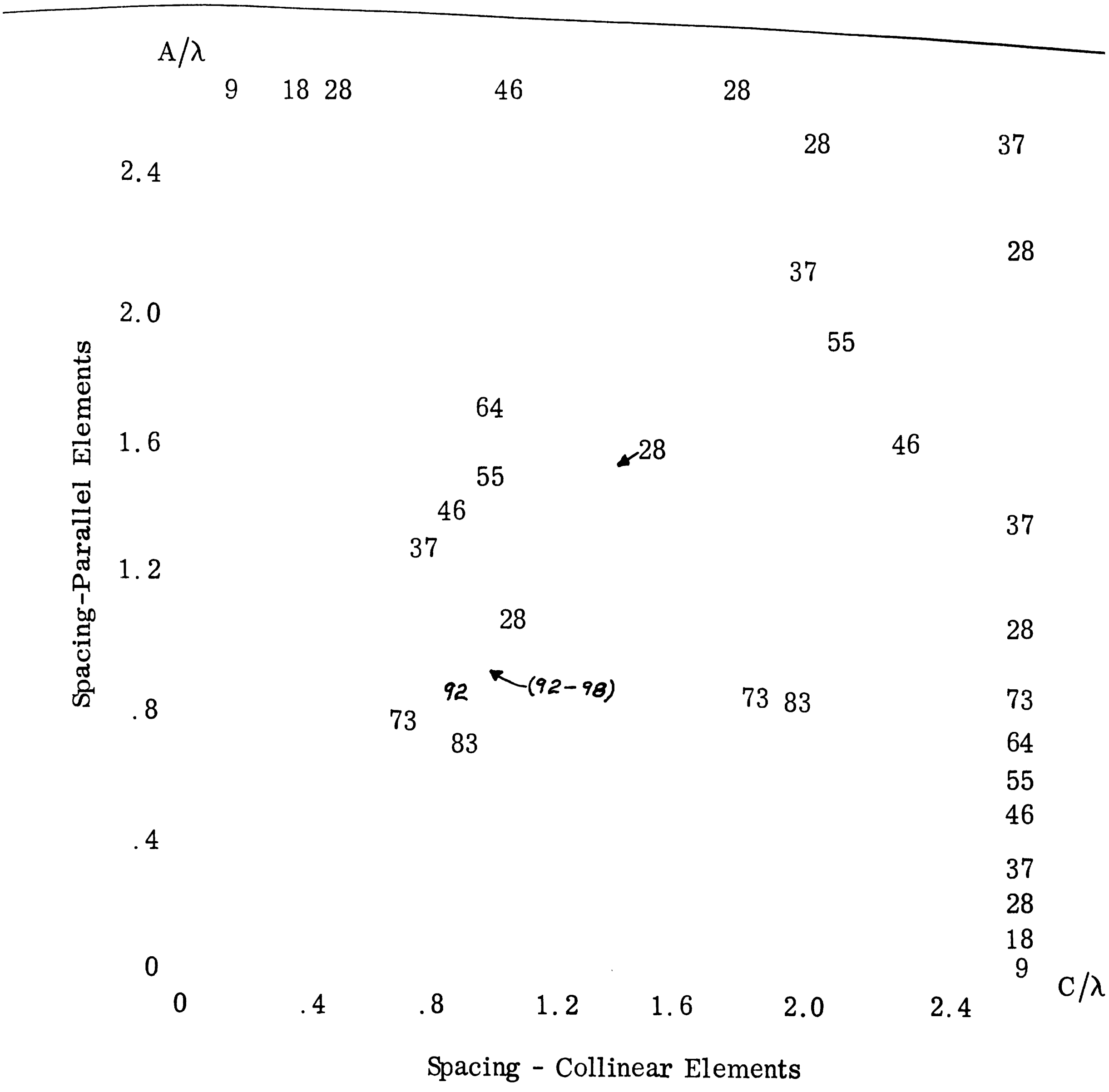

Contour Values in Percent of Maximum

C = 414.12 at A/λ = .81875

C/λ = .94375

FIG. 3-3: CONTOUR MAP - DIRECTIVITY OF 10x10 PLANAR ARRAY.

FIG. 3-4: CONTOUR MAP - DIRECTIVITY OF 20 x 20 PLANAR ARRAY.

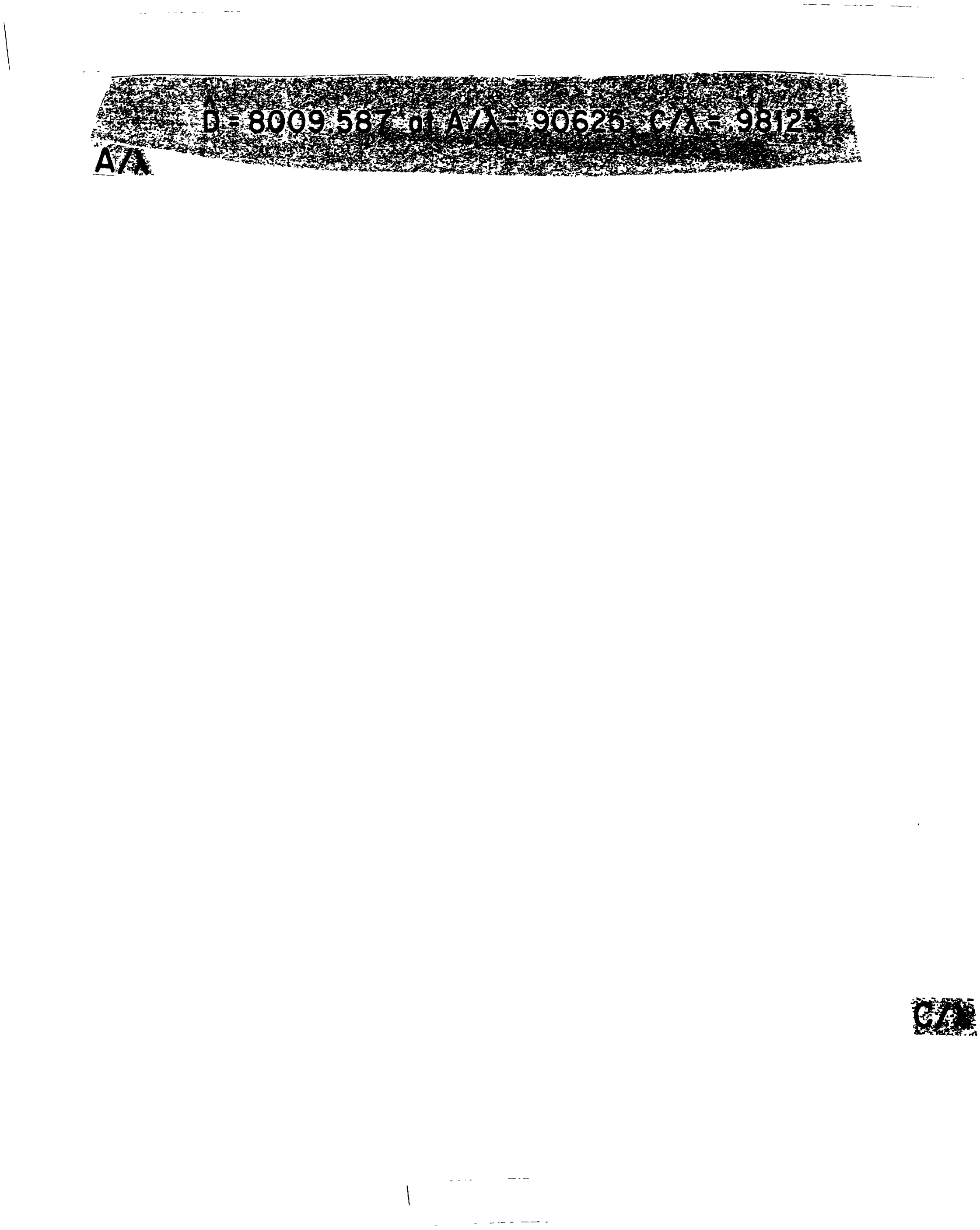

FIG. 3-5: CONTOUR MAP - DIRECTIVITY OF 40x40 PLANAR ARRAY.

the values of the directivity function for all points lying in the region characterized by contour lines of lower value. Those areas which are only bounded by one contour line are characterized by directivity values lying between the labled contour line value and the next highest contour value of the map, e.g., in Fig 3-2 at the extreme upper right of the map, the regions bounded only by the lines marked 35 percent and 52 percent contain values lying in the ranges 35 percent through 43 percent, and 52 percent through 61 percent respectively.

As is evident from these contour maps, with the exception of Fig. 3-3, the search program was limited to a region 1.5λ by 1.5λ in the element-spacing plane. This limitation was imposed since it is known that the formation of grating lobes, i.e., multiple "main beams", in the radiation pattern of a planar array occurs for element spacings greater than 1λ, and this behavior is associated with a marked decrease in directivity. The case of a 10 x 10 planar array, Fig. 3-3, was investigated over a somewhat larger range of the element spacing variables to demonstrate this directivity limiting in a positive manner.

The shaded areas in Figs. 3-3, 3-4, and 3-5 represent regions of rapid change in the value of the directivity function, i.e., a steep slope in the surface defined by the directivity function.

The absence of a strip-like region of large rapid change in directivity parallel to the axis of A/λ (parallel element spacing), can be ascribed to the influence of the array element pattern. The dipole element pattern has a null lying in the direction corresponding to potential grating lobes which would be formed as the collinear element spacing of the array approaches and then exceeds one wavelength. As can be seen from the contour maps, although no such sharply defined region occurs, the array directivity does decrease noticeably as C passes through the value $C/\lambda = 1.0$ indicating that the grating lobes associated with collinear element spacing are not completely surpressed, with resultant large sidelobes.

In order to obtain a clearer representation of the details of the directivity surface in the vicinity of the maximum directivity point, cross section profiles of the surface were also obtained from the computer program output, as mentioned in Section 3.2. Figure 3-6 summarizes the behavior of these cuts. Four separate cross section profiles were obtained, each representing an excursion of approximately $\lambda/16$ on either side of the point of maximum directivity. Two cuts, denoted by "C = constant" and "A = constant" in Fig. 3-6, were taken parallel to the contour map coordinate axes through the maximum directivity point. The remaining two profiles, denoted by "$\Delta A = \Delta C$" and "$\Delta A = -\Delta C$" in Fig. 3-6, passed through the maximum directivity point and were oriented at 45° with respect to the first two cuts. The maximum variation in the directivity value which occurs over the range of any cross section profile is given at the right of each set of profiles. The variation is expressed in percent of the value $\hat{D}$.

From these figures it appears that if a directivity value within roughly 10 percent of the value $\hat{D}$ is to be achieved, then element spacings must be approximately within $\pm$ 3 percent of their optimum values as a conservative estimate. It is assumed here, and in the following discussions that all elements of a planar array are coplanar to within a very close tolerance, e.g., less than 1 percent variation. Since element spacing is normalized by wavelength in all calculations, variation in the operating frequency of the array, i.e., frequency bandwidth, causes variations in effective element spacings. Thus, the above statement concerning directivity variations can also be interpreted in the following manner. If it is desired that a planar array operate with near uniform maximum directivity, then, all other factors being equal, the array bandwidth should be restricted to about $\pm$ 3 percent, assuming accurate physical positioning of the array elements. This comment on bandwidth effects on directivity assumes that the array pattern is the dominant factor in determining the overall array directivity. The problem is, of course, considerably more complex since the array element and feed system components may all have bandwidth limitations of a more severe nature. The experimental results of Chapter V indicate that the applicability of results of array directivity calculations given here are not limited to the short dipole model used in deriving the directivity expressions leading to these results. Consequently, the results on directivity can, within limits, be applied to various cases, independent of the array

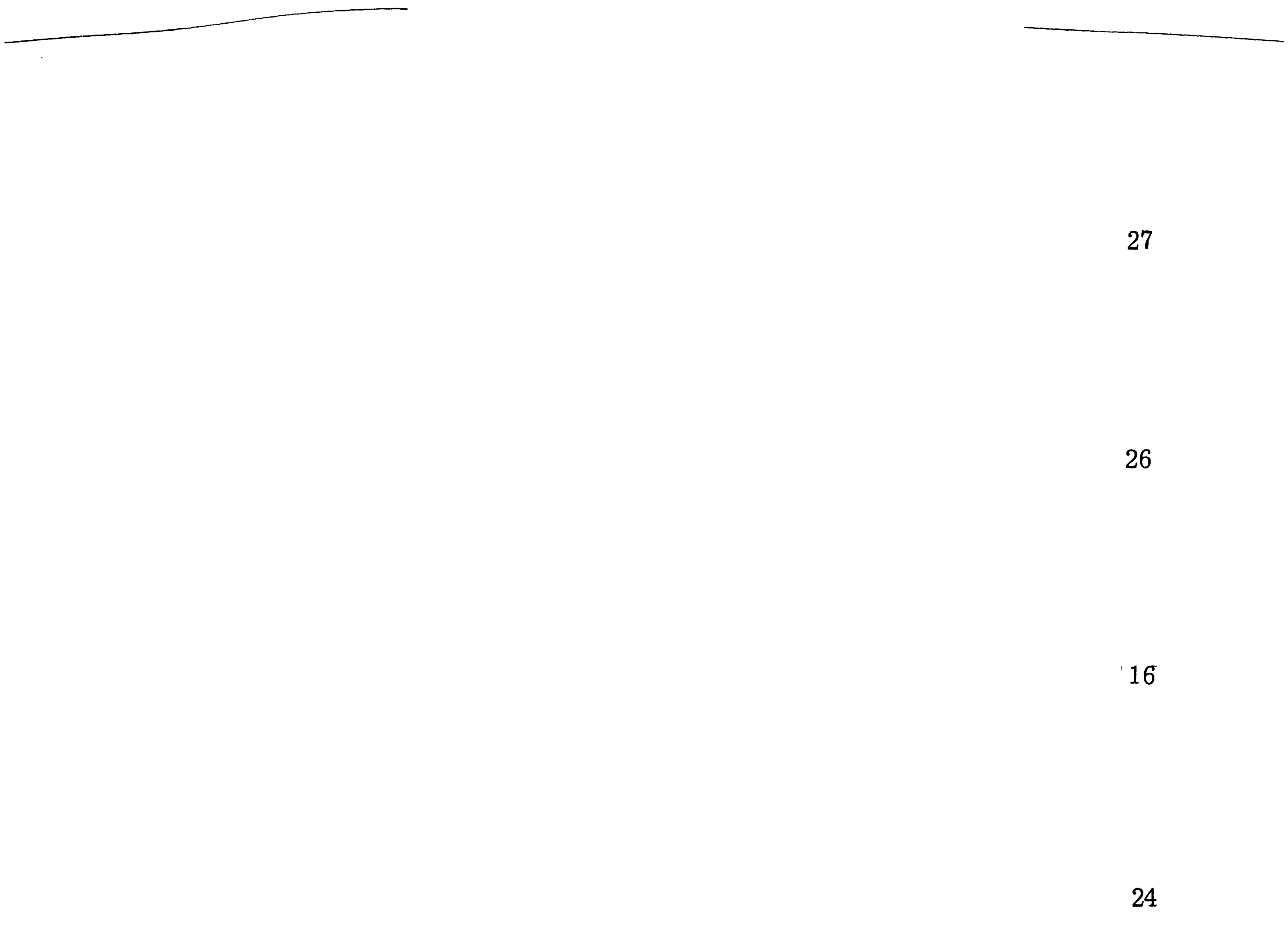

FIG. 3-6: CROSS SECTION PROFILES OF THE PLANAR ARRAY DIRECTIVITY FUNCTION SURFACE.

element used. Thus the bandwidth limitations discussed above can be considered independent of other bandwidth restrictions. The component with the narrowest bandwidth will then determine the system bandwidth.

In general, the directivity contour maps and their cross section profiles indicate that from the standpoint of minimum sensitivity to variations in interelement spacing, the point corresponding to $\hat{D}$ is not the most efficient operating point. Less variation in directivity can be achieved over a given neighborhood of the operating point if the point is displaced in the direction of lower values of interelement spacings, i.e., displaced towards the origin of the contour map axes. The "bandwidths" for such "non-optimum" operating points increase to about ± 5 to ± 6 percent.

With reference to the initial assumptions of Section 3.2 concerning the behavior of the surface defined by the directivity function, it can be noted from the cross section profiles that the surface is in fact not unimodal for the larger array cases. The contour maps do not illustrate these surface "corrugations" because of the coarse resolution necessary for readable maps. The contour maps and cross section profiles both indicate that the functional surface also can exhibit ridge behavior.

3.3.1 Directivity Properties of a Planar Array Backed by a Ground Plane

A ground plane is often used in conjunction with a planar array for reasons related to the bidirectional radiation characteristics of the array. The presence of a ground plane behind a planar array eliminates the ambiguity of the two identical main beams of the (isolated) array and results in a radiation pattern essentially confined to a half space.

The influence of a ground plane on the directivity of planar arrays of various sizes was studied by using the image technique. This technique, assuming an infinite ground plane, converts the problem into a form which can be investigated by using as a model a three dimensional array composed of two decks of elements. The two array decks are constrained to remain 180° out of phase at all times.

Two specific cases were chosen for the ground plane spacing. The first, having a ground plane to array separation of $h = .1\lambda$, corresponds to a case of high directivity but minimal signal strength, i.e., maximum received signal approaching zero. The second case, $h = .25\lambda$, results in a lower directivity value, but largest attainable signal strength. Three array sizes were considered for each of these cases: 1) 5 x 5 ; 2) 10 x 10 ; 3) 20 x 20 . (The notation "LxM" denotes the number of elements along each coordinate axis of the array, and will be later extended to "LxMxN" for the lattice array cases.) The contour maps of the directivity function of the 20 x 20 array for both ground plane configurations are shown as Figs. 3-7 and 3-8 . Cross section profiles of the directivity function surface for each array size and for each ground plane configuration are shown as Figs. 3-9 and 3-10. The format for these profiles is the same as used in Fig. 3-6, discussed above.

Several effects of the ground plane on array directivity can be observed from these figures. First, comparing the level curves of the contour maps of the 20 x 20 arrays both with and without a ground plane (Figs. 3-4, 3-7, and 3-8), shows the directivity surface in the ground plane case to generally have much less pronounced slopes in the regions about $A/\lambda = 1.0$ and $C/\lambda = 1.0$, i.e., the grating lobe phenomnea is surpressed by the ground plane. In addition, regions of high directivity, e.g., within 75 percent of the maximum, are noticeably larger in the ground plane cases. Comparing the various cross section profiles for the ground plane cases and the ordinary array in free space, it is apparent that the directivity surface in the vicinity of the ground plane is strongly smoothed by the presence of the ground plane. This smoothing is particularly evident for the larger array sizes where the isolated array directivity function surface is quite corrugated. The cross section profiles for "A = constant" clearly illustrate the significant change in the directivity surface rate of decrease in the vicinity of $C/\lambda = 1.0$ (when $A = A_{\text{optimum}}$) from the isolated array cases.

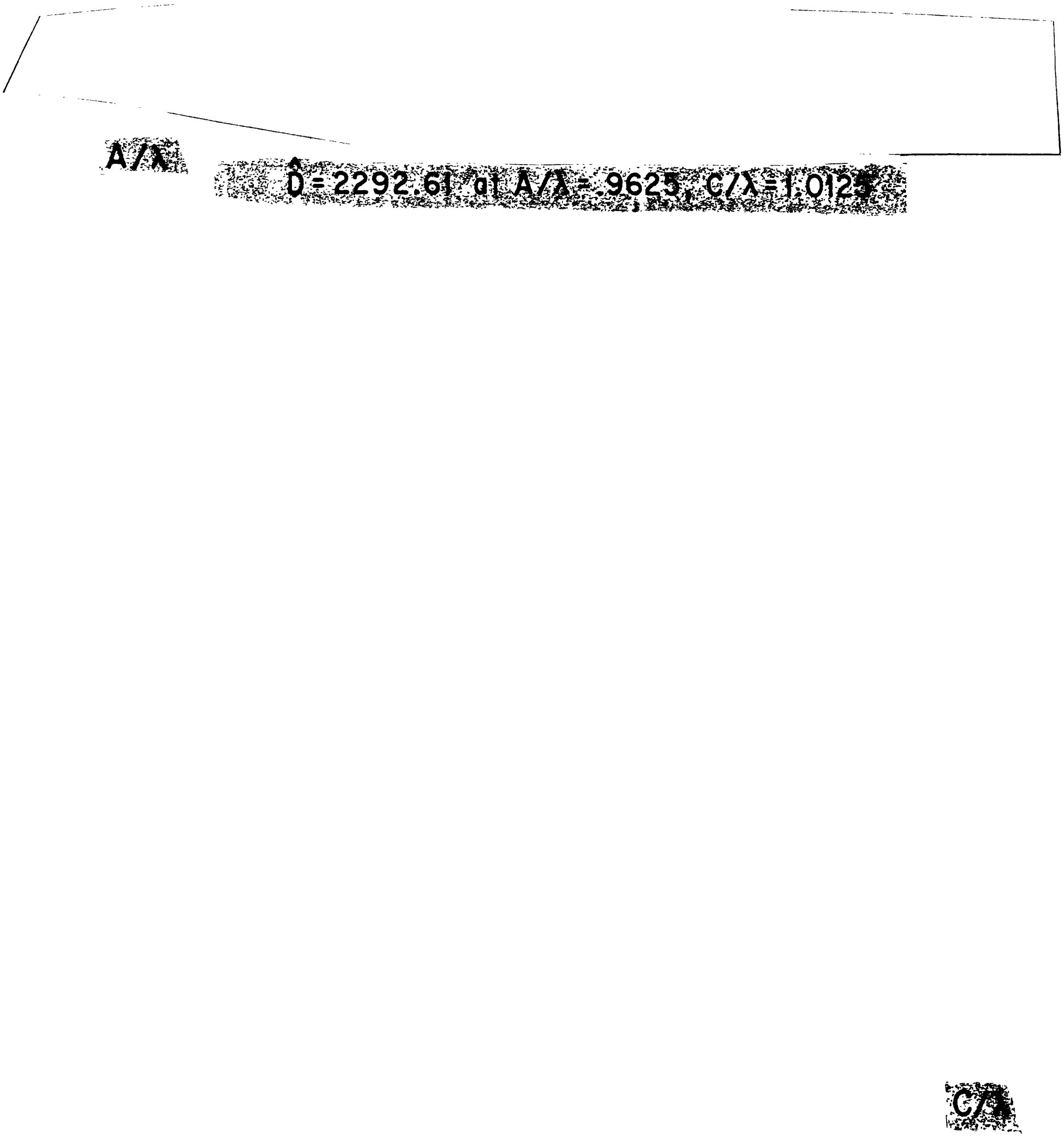

Contour Values in Percent of Maximum

FIG. 3-7: CONTOUR MAP - DIRECTIVITY OF 20 x 20 PLANAR ARRAY GROUND PLANE CASE: $h/\lambda = .1$.

Contour Values in Percent of Maximum

FIG. 3-8: CONTOUR MAP - DIRECTIVITY OF 20 x 20 PLANAR ARRAY GROUND PLANE CASE: $h/\lambda = .25$.

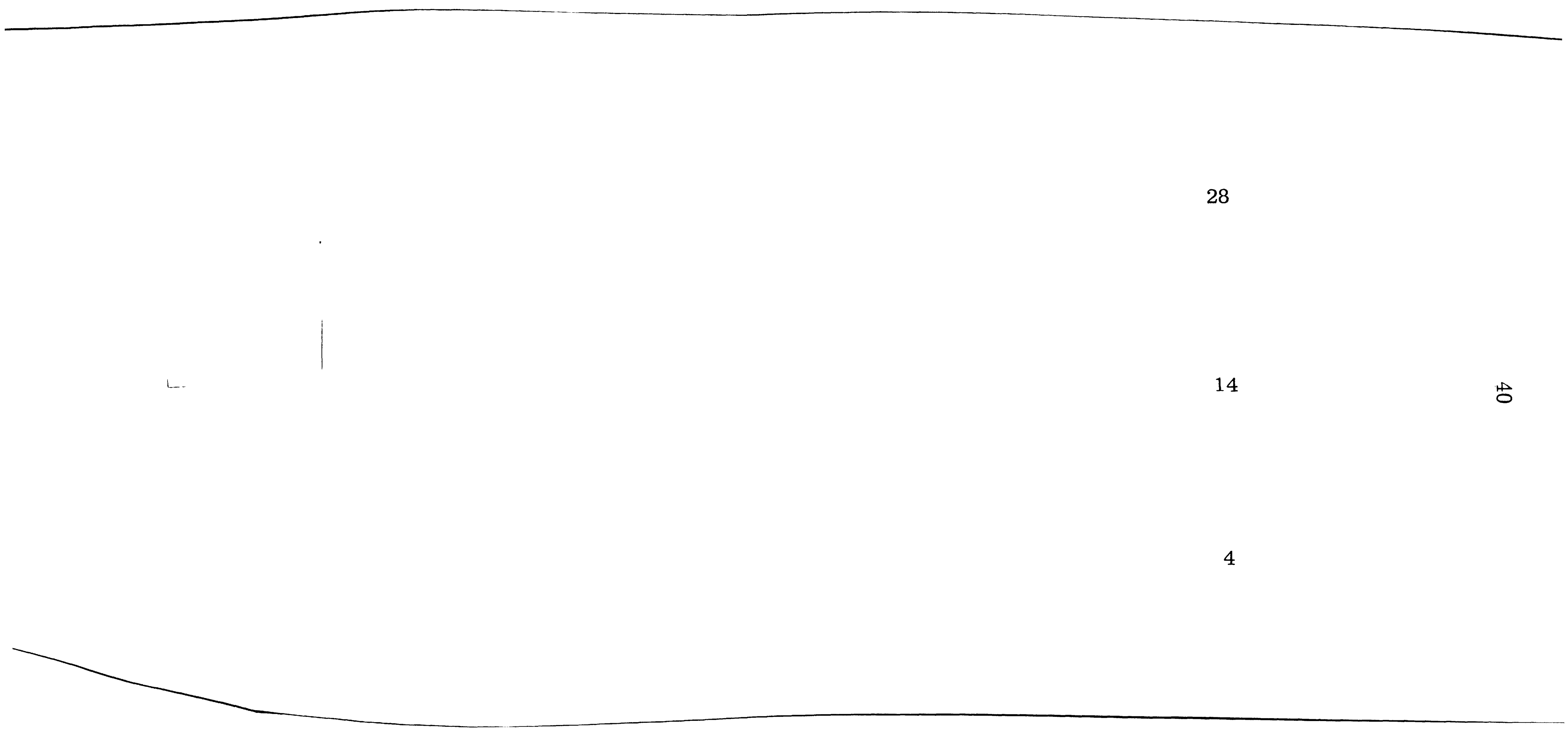

FIG. 3-9: CROSS SECTION PROFILES OF THE PLANAR ARRAY DIRECTIVITY FUNCTION — GROUND PLANE CASE: $h/\lambda = .1$.

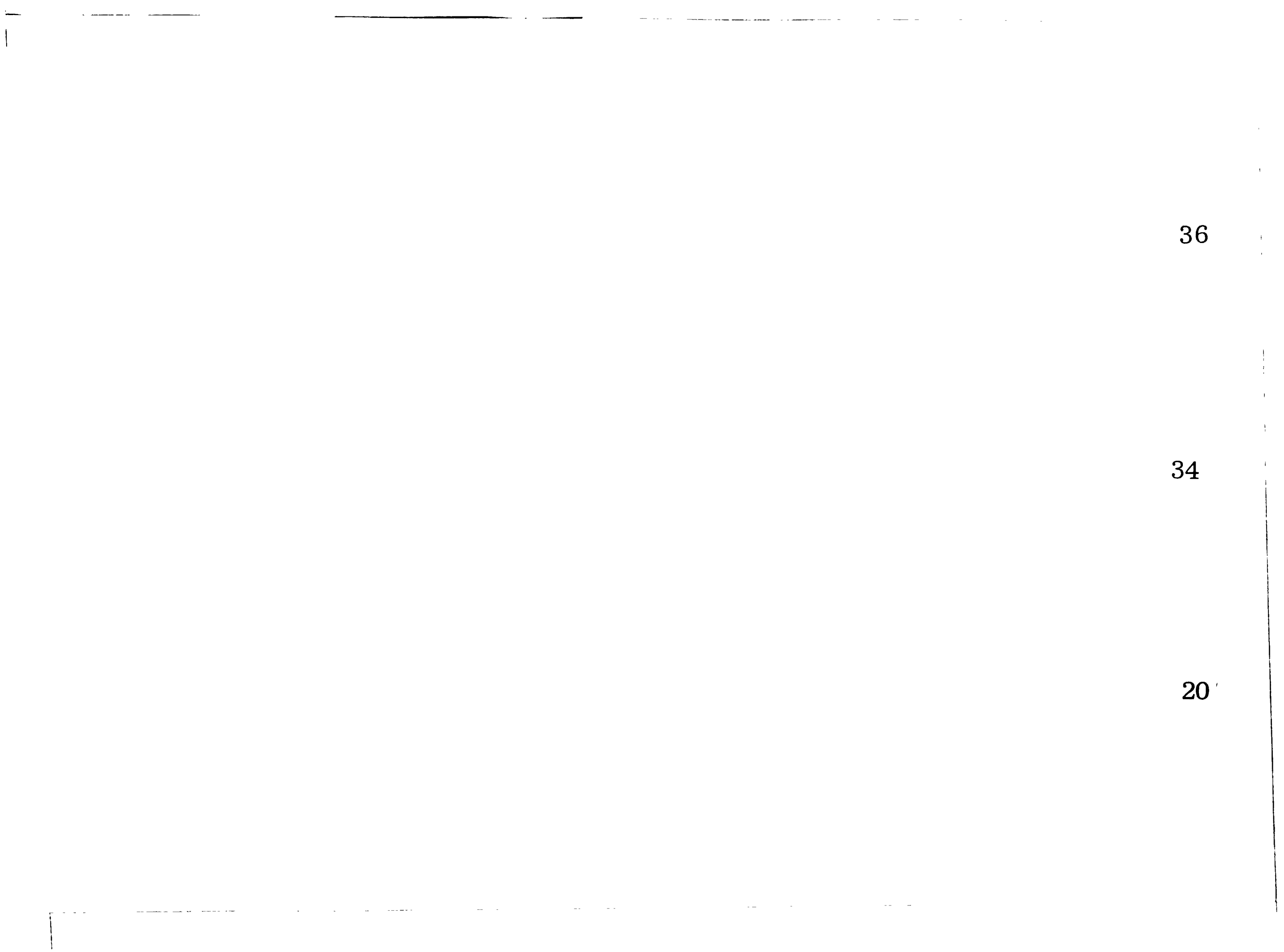

FIG. 3-10: CROSS SECTION PROFILES OF THE PLANAR ARRAY DIRECTIVITY FUNCTION — GROUND PLANE CASE: $h/\lambda = .25$.

Estimates of the sensitivity of the maximum nominal directivity value to changes in element spacing or to frequency bandwidth, similar to those of Section 3.3, are also of interest for the array type of this section.

In the case of a planar array backed by a ground plane, frequency variations cause variations in the effective spacing of broadside elements, and also in the effective spacing "h" between the planar array and the ground plane, i.e., changes in the effective "spacing" of the broadside elements and their images. Effective or actual (i.e., spatial distance) changes in the value of the parameter h, however, are secondary effects as far as the array directivity is concerned. Figure 3-11 shows the behavior of $\hat{D}$ as a function of "h". This curve has essentially the same form, regardless of the number of elements in the planar array. The table given in the figure illustrates the extent of the variation in $\hat{D}$ as "h" varies from $.1\lambda$ to $.25\lambda$. The dominating effect of the broadside array pattern over the endfire pattern of the array-ground plane configuration is apparent from the decrease in "Δ" with increasing array size. Comparison of this figure with the preceding Figs. (3-7 through 3-10) indicates that the directivity function is much less sensitive to changes in the value "h" than to changes in the values "A" and "C". Thus, comments on the effective "bandwidth" of a planar array backed by a ground plane can be based essentially on the parameters "A" and "C", i.e., the contour maps and contour map profiles.

Proceeding on this basis, the directivity of a planar array backed by a ground plane appears to be significantly less sensitive to changes or errors in the spacing of the array elements, or to bandwidth effects, than is the isolated array directivity. As an example, from the contour maps of the 20 x 20 planar array cases, it appears that the operational directivity of such an array can be maintained within 10 percent of the maximum nominal value $\hat{D}$ for bandwidths of the order of ±8 to ±10 percent for non optimum operating points. ("Bandwidth" as used here implies either frequency or element-spacing variations.)

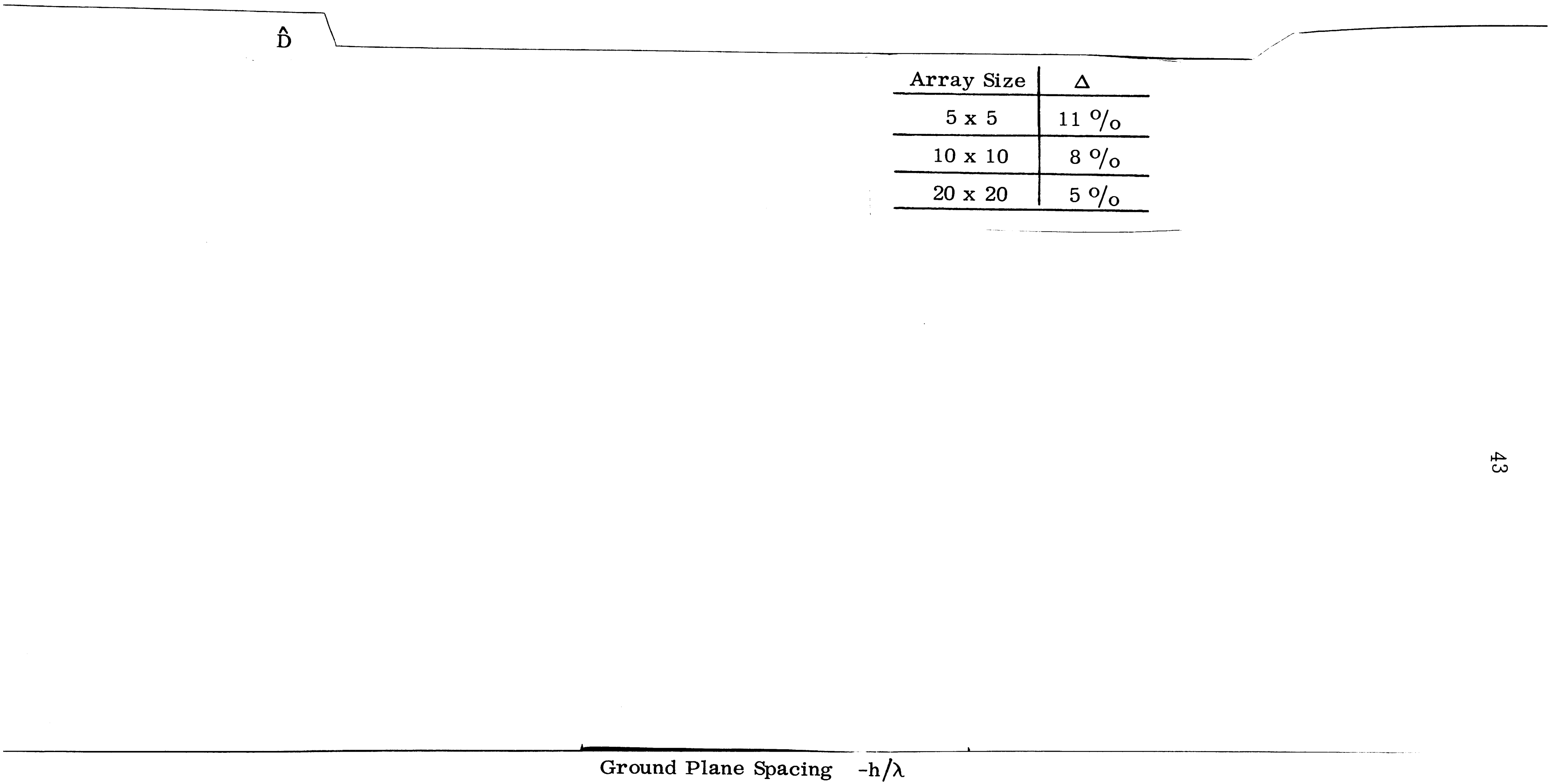

Array Size	Δ
5 x 5	11 %
10 x 10	8 %
20 x 20	5 %

FIG. 3-11: PLANAR ARRAY MAXIMUM NOMINAL DIRECTIVITY VERSUS GROUND PLANE SPACING.

However, if such an array is operated at the point at which $\hat{D}$ is achieved, then the effective "bandwidth" decreases to roughly the same magnitude as in the case of an isolated array, i.e., ± 3 percent.

Thus, in addition to its chief purpose, i.e., converting bidirectional radiation to unidirectional radiation, a ground plane used in conjunction with a planar array also results in slightly increased directivity, an appreciable increase in the effective "bandwidth" of the array, and a much "smoother" directivity function surface as compared with the isolated planar array case.

3.4 Directivity Properties of Lattice Arrays

The computation procedure for the three dimensional lattice array is a direct extension of that for the planar array from the conceptual standpoint, as discussed in Section 3.2. However, the computer time which would be required to search the full, presumably useful, ranges of each spacing variable increases enormously from that characteristic of the two dimensional case. This increase is due to the "depth" of the array, i.e., the decks of elements arranged in endfire configuration. As the number of decks increases, the required computation time increases very rapidly. This behavior results from the increase in both number and complexity of the terms involved in the directivity expression for the lattice array configuration, i.e., the increased number of double summations involved, and the addition of a triple sum.

The computation problem is further complicated by the fact that the ranges of interelement spacings for which grating lobe phenomena occur are no longer clear cut. This situation can be explained as follows.

Based upon the pattern multiplication principle, the endfire pattern of progressively phased decks of a lattice array provides a weighting factor which can be tailored to suppress grating lobes which would normally exist due to the planar array pattern of a typical array deck when the spacings of deck elements exceed λ . Similarly, the planar array pattern can be viewed as a weighting function for the endfire radiation pattern of the array decks and tailored to suppress grating lobes which would occur when the deck spacings exceed λ/2.

In view of these facts, it appears difficult, apriori, to limit the upper bounds of the ranges of the spacing variables to be searched in determining $\hat{D}$, and still be certain that a global, and not a local maximum of the directivity function has been found. However, this difficulty was resolved on the basis of the following practical considerations.

The endfire pattern for spacings less than λ/2 provides a very effective weighting factor for suppression of any grating lobes which might be associated with the planar array radiation pattern of a typical deck of elements. The effectiveness of this pattern as a weighting function is related to the fact that it is a figure of revolution in three dimensional space, its configuration being completely specified by any two dimensional cut containing its axis of revolution.

It is not apparent that a planar array pattern with no grating lobes can be as effective in suppressing the grating lobes associated with the endfire pattern of the array decks. The rather complicated structure of the planar array pattern in three dimensions makes it difficult to visualize its effect as a weighting function on the endfire radiation pattern. In addition, from studies of linear arrays (Tai, 1963), it is known that the directivity parameter is considerably more sensitive to the broadside element spacing variable, than to the endfire element spacing variable. Consequently, from the standpoint of achieving as large a value as possible for the directivity of a lattice array, it seems less desirable to restrict broadside element spacings within a deck (to prevent grating lobes), than to restrict the endfire spacings of the lattice decks (as in the previous case).

Consider now the case where the broadside planar array pattern of a typical lattice deck, and the endfire pattern of successive lattice decks are both allowed to exhibit grating lobes. In this case the problem of grating lobe suppression, as discussed above, becomes considerably more complex since neither component pattern is free of grating lobes. The maximum directivity value achieved in such a case can exceed that achieved in other cases due to the increase in all array dimensions. However, the practical significance of this case is doubtful from two standpoints.

First, the radiation pattern of such an array can display extremely high sidelobes due to incomplete cancellation of grating lobes. Second, the stability of the pattern of such an array with respect to mechanical and electrical tolerance error is likely to be quite poor since many potential grating lobes must be simultaneously suppressed.

Based on all of the above considerations and the results for linear and planar arrays, the ranges of interelement spacings chosen for a computer search procedure were: parallel (broadside) element spacing "A", $.6 \leq A/\lambda \leq 1.5$; endfire element (deck) spacing "B", $.1 \leq B/\lambda \leq .5$; collinear (broadside) element spacing "C", $.6 \leq C/\lambda \leq 1.5$. These values were used for an extensive investigation of a small (nominal) size lattice array which corresponds to the array developed for the experimental portion of this study, i.e., a 4 x 4 x 4 array. In addition to a search of the above ranges of spacing variables, some data were also obtained for the case when $\left\{A/\lambda \leq 1.0,\ C/\lambda \leq 1.0,\ .5 \leq B/\lambda \leq 1.0\right\}$, i.e., the region where the planar array pattern serves as a weighting function to suppress grating lobes of the endfire pattern, and also for the case when all spacing variable ranges include values which characterize grating lobe behavior for the corresponding radiation patterns. These calculations, though somewhat limited, substantiated the above intuitive limitations on these cases.

The results of the search calculations for the principal region of interest for the 4 x 4 x 4 lattice array case gave sufficient data to enable subsequent search calculations for larger array sizes to be performed over smaller ranges of the spacing variables.

The four dimensional nature of the directivity function hypersurface in the lattice array case obviously poses certain difficulties for displaying the behavior of directivity as a function of the spacing variables. A combination of a contour map and a single curve was chosen to yield significant information on the behavior of the hypersurface. The contour map displays the values of directivity as a function of broadside element spacing, i.e., spacing of elements within a given planar array deck, for that value of endfire spacing which achieves $\hat{D}$. Two such contour maps are shown in Figs. 3-12 and 3-13 for the 4 x 4 x 4 and 10 x 10 x 10 lattice array cases. The remaining data display is a curve which shows the behavior of the maximum nominal directivity as a function of "B". Curves of this type for each array size investigated are shown in Fig. 3-14.

Two features of the lattice array contour maps which differ considerably from the planar array contour maps are: 1) the (broadside) interelement spacings which correspond to the point $\hat{D}$ exceed the value λ (with the exception of the value "A" in the smaller array case of Fig. 3-12); 2) the contour maps do not exhibit grating lobe behavior similar to that observed in the planar array maps.

The curves of directivity as a function of endfire ("array deck") spacing, Fig. 3-14, illustrate the directivity values attainable with various sizes of arrays, and also the increase in the optimum value of "B" as the array depth (number of decks) increases.

The complexity of the four dimensional directivity hypersurface makes it difficult to comment on element spacing tolerance limits, or "array bandwidth", as was done above for planar arrays. It is assumed, however, that the contour maps of the cross section cuts of the directivity hypersurface for values of "B" close to the optimum are similar to those shown for $B = B_{optimum}$, then combining the features noted in Figs. 3-12, 3-13, and 3-14, it appears that "bandwidths" on the order of those indicated for the planar array backed by a ground plane apply to lattice arrays as well, i.e., bandwidths on the order of ± 5 to ± 10 percent.

3.5 Figures of Merit and General Characteristics of Linear, Planar, and Lattice Arrays

Numerical data on various parameters of linear, planar, and lattice arrays have been compiled from the directivity calculations discussed in the above sections,

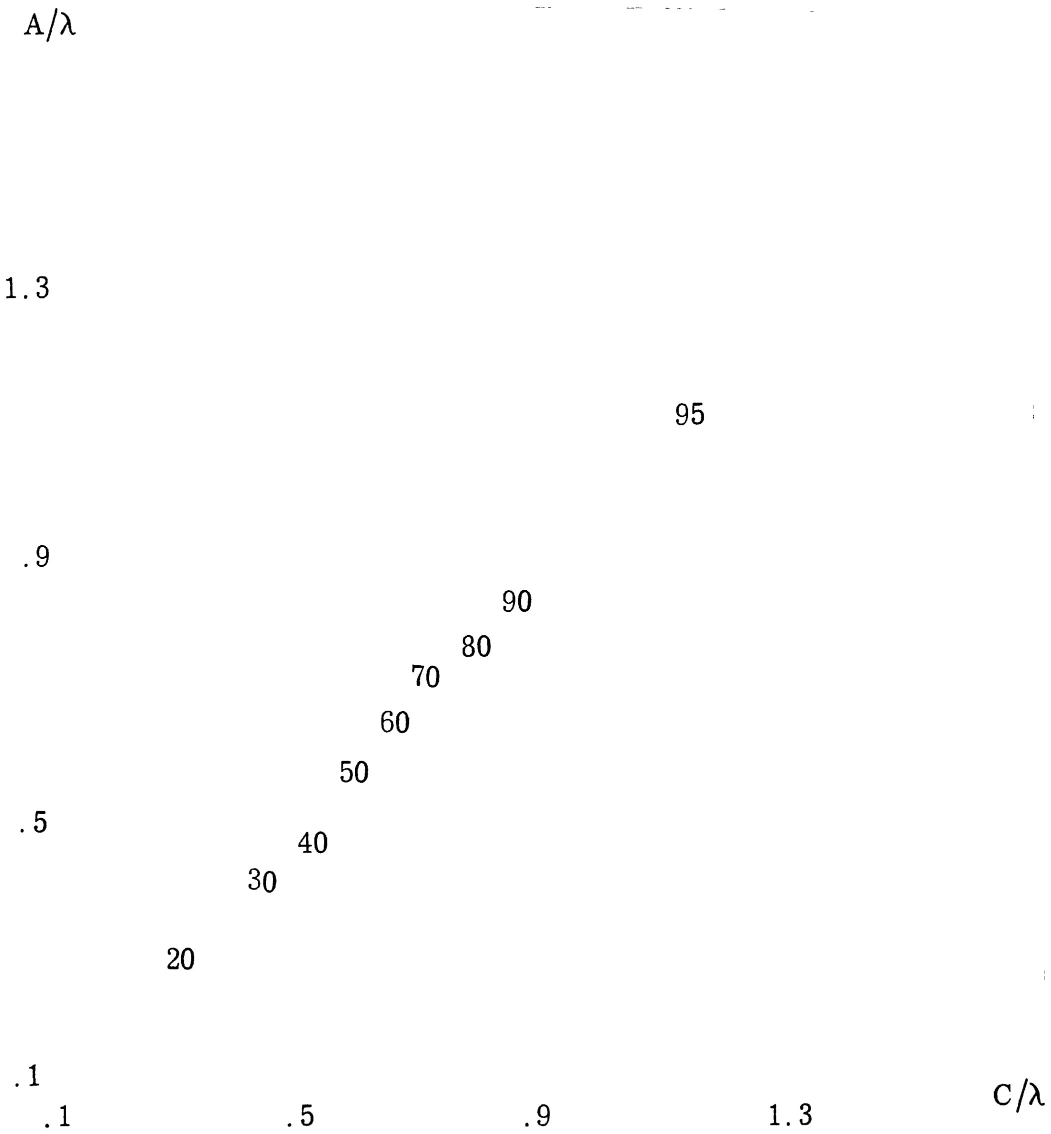

Contour Values in Percent of Maximum

$B/\lambda = .3875$

$\hat{D} = 152.8$ at $A/\lambda = .8875$

$C/\lambda = 1.0875$

FIG. 3-12: CONTOUR MAP - DIRECTIVITY OF 4x4x4 LATTICE ARRAY.

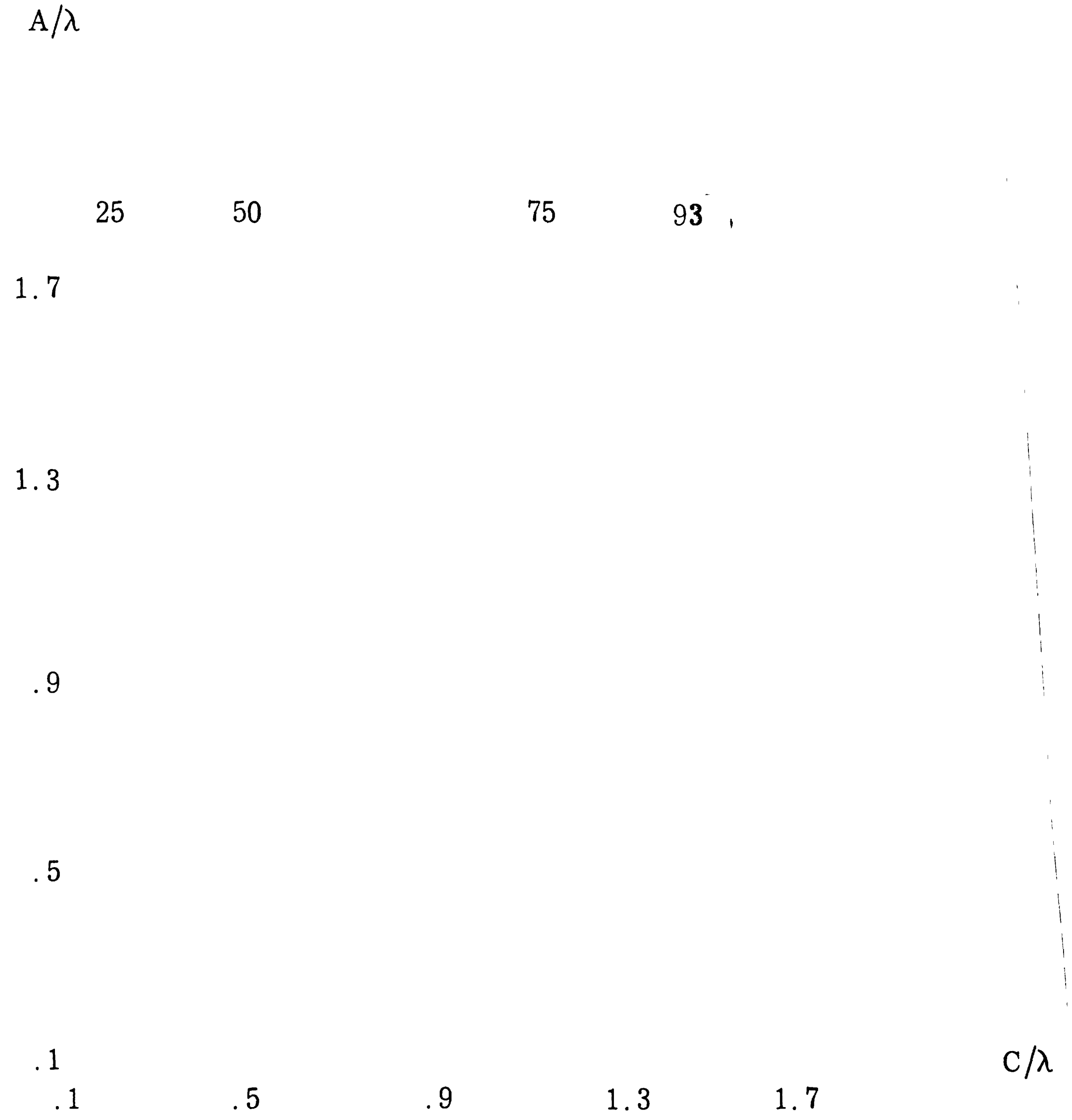

Contour Values in Percent of Maximum

B/λ = .450

$\hat{D}$ = 2851.5 at A/λ = 1.675

C/λ = 1.70

FIG. 3-13: CONTOUR MAP - DIRECTIVITY OF 10x10x10 LATTICE ARRAY.

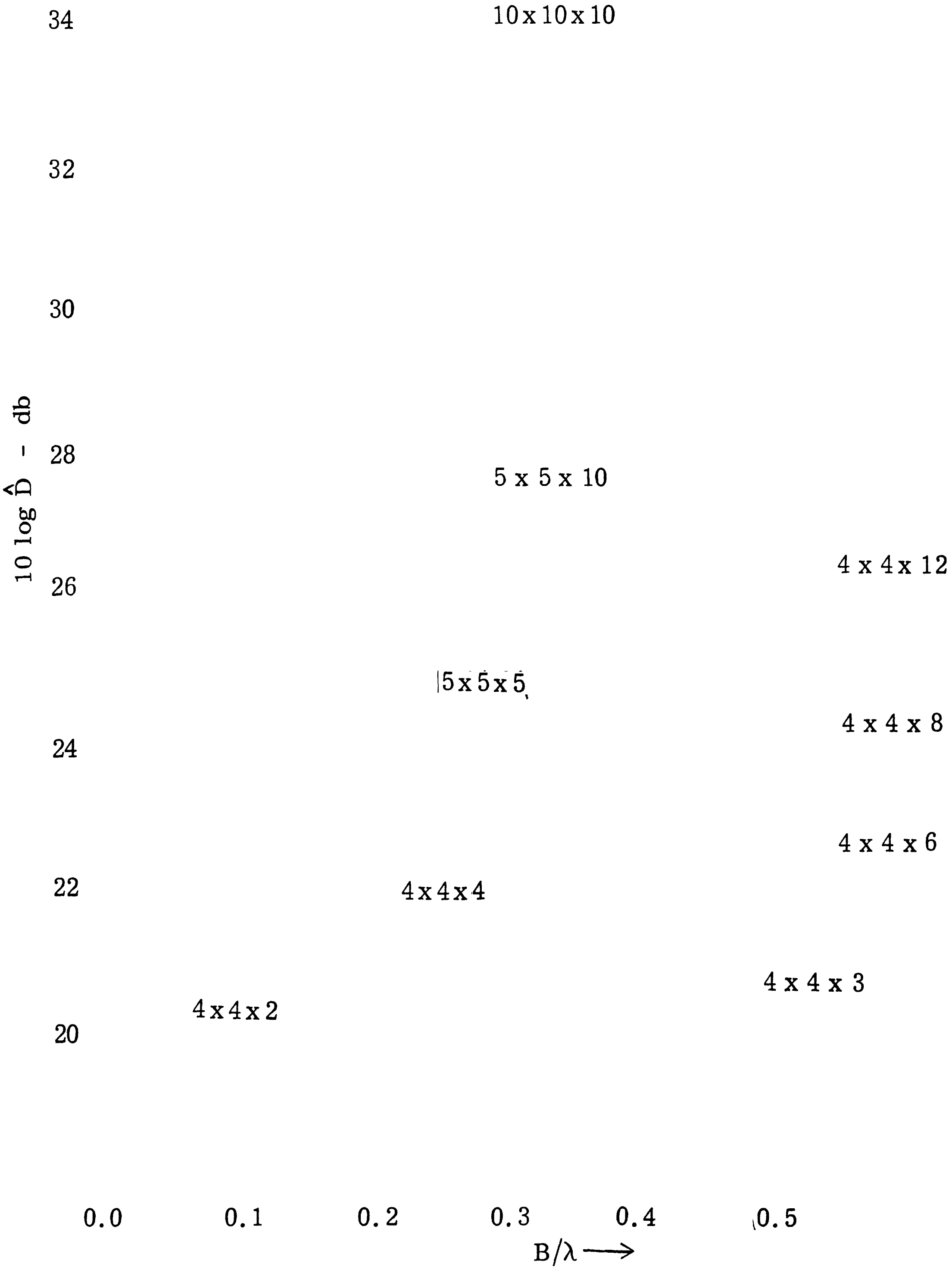

FIG. 3-14: NOMINAL DIRECTIVITY VERSUS ENDFIRE SPACING "B" — LATTICE ARRAYS.

and the radiation pattern calculations to be discussed below. By presenting this data on a comparative basis, i.e., drawing comparisons between parameter values for different array types, the significance of certain figures of merit becomes apparent, and some advantages and disadvantages of the various array types clarified. The following subsections summarize these figures of merit and array characteristics.

3.5.1 Maximum Nominal Directivity

Figure 3-15 summarizes the results of the directivity calculations for planar and lattice arrays. The three lattice array data points indicated with an asterisk were not computed using the three dimensional search procedure. The directivities indicated for these twenty deck arrays were calculated based on estimates of the optimum spacing values obtained from the data of Section 3.5.2. This procedure was necessary since very large computer times would have been required in a direct search for $\hat{D}$. Based on the optimum results for other cases, the values of directivity obtained for these arrays appear close to the maximum nominal values which would be expected.

The planar arrays studied in this investigation have been constrained to have the same number of elements along each coordinate axis of an array, i.e., an N x N array. From Fig. 3-15, it is seen that the maximum nominal directivity increases roughly in proportion to the number of elements. For example, increasing the size of a planar array from 10 x 10 to 20 x 20 results in an increase of 6.5 db in the value of $\hat{D}$. The exact change in $\hat{D}$ which results from the doubling of the parameter "N" is seen to be slightly larger than 6.0 db for smaller arrays, and approaches an apparent limit of 6.0 db for very large arrays.

The two cases shown in Fig. 3-15 for a planar array backed by a ground plane exhibit only slight differences in $\hat{D}$ for a given array size. The increase in $\hat{D}$ obtained by use of the ground plane over that of an isolated planar array of similar size is also small, i.e., approximately 1.0 db or less. Consequently, effects other than increased directivity are probably more significant in the choice of a planar array backed by a ground plane over an isolated array for a given application.

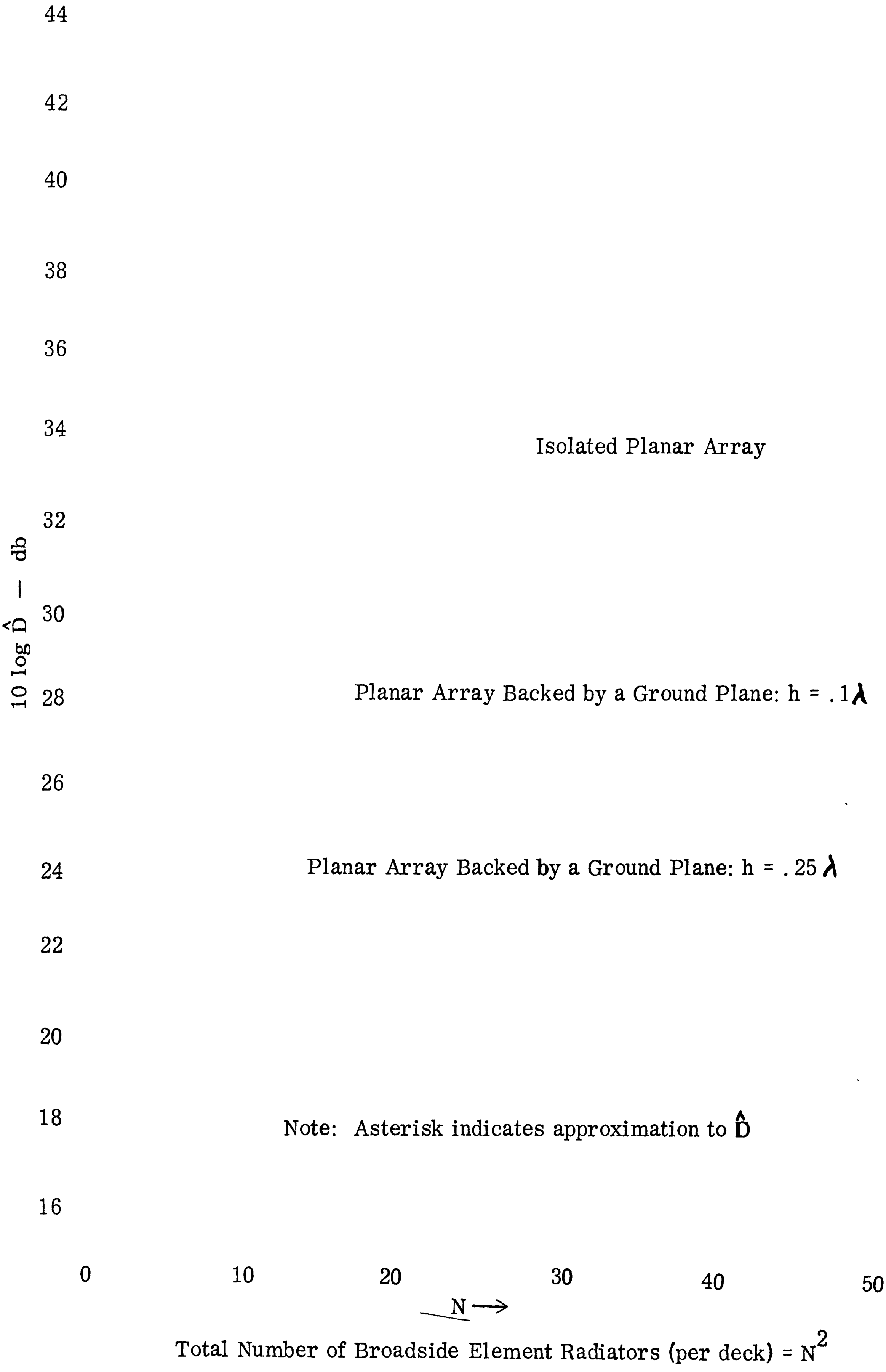

FIG. 3-15: MAXIMUM NOMINAL DIRECTIVITIES OF TWO AND THREE DIMENSIONAL DIPOLE ARRAYS.

The points defining the directivity "curves" for the lattice arrays are labeled according to the number "M" of decks in the array. From the curve for the 4 x 4 x M case, it is seen that as M increases, the increase in $\hat{D}$ becomes proportional to $K \Delta M$, where $\Delta M = \frac{M_{new}}{M_{old}}$ and K is slightly less than 1.0. This same rule holds for the 5 x 5 x M and 10 x 10 x M cases. As the number of elements N along each (broadside) aperture axis increases, the increase in $\hat{D}$ appears to vary in the same manner as for planar arrays. As an example of these relations, if the number of elements along each coordinate axis of a lattice array is doubled, the value $\hat{D}$ is increased by a factor of approximately $(2)^3 = 8$, or 9 db.

Direct comparisons between planar and lattice array directivities will be left to Section 3.5.3 where, using the figures of merit defined there, more meaningful comparisons of the two array types can be obtained. The values of $\hat{D}$ which characterize the various sizes and types of arrays can be observed directly from Fig. 3-15.

3.5.2 Optimum Element Spacings for Linear, Planar, and Lattice Arrays

The spacings of element radiators for which the value $\hat{D}$ is achieved are termed "optimum element spacings". The optimum spacings for the various types and sizes of arrays which have been considered in this investigation are shown in Fig. 3-16.

Curves for the three linear array types are given in Fig. 3-16a for $N \leq 50$. Calculations for these array types were carried out for $N \leq 100$, but since the optimum spacing curves are close to their limiting values at $N = 50$, the abscissa of the curve was terminated at $N = 50$. The exact limiting values, or asymptotes, of these optimum spacing curves are;

1) $B/\lambda = .48$ for linear endfire arrays
2) $A/\lambda = .96$ for broadside linear arrays of parallel elements
3) $C/\lambda = 1.00$ for broadside linear arrays of collinear elements.

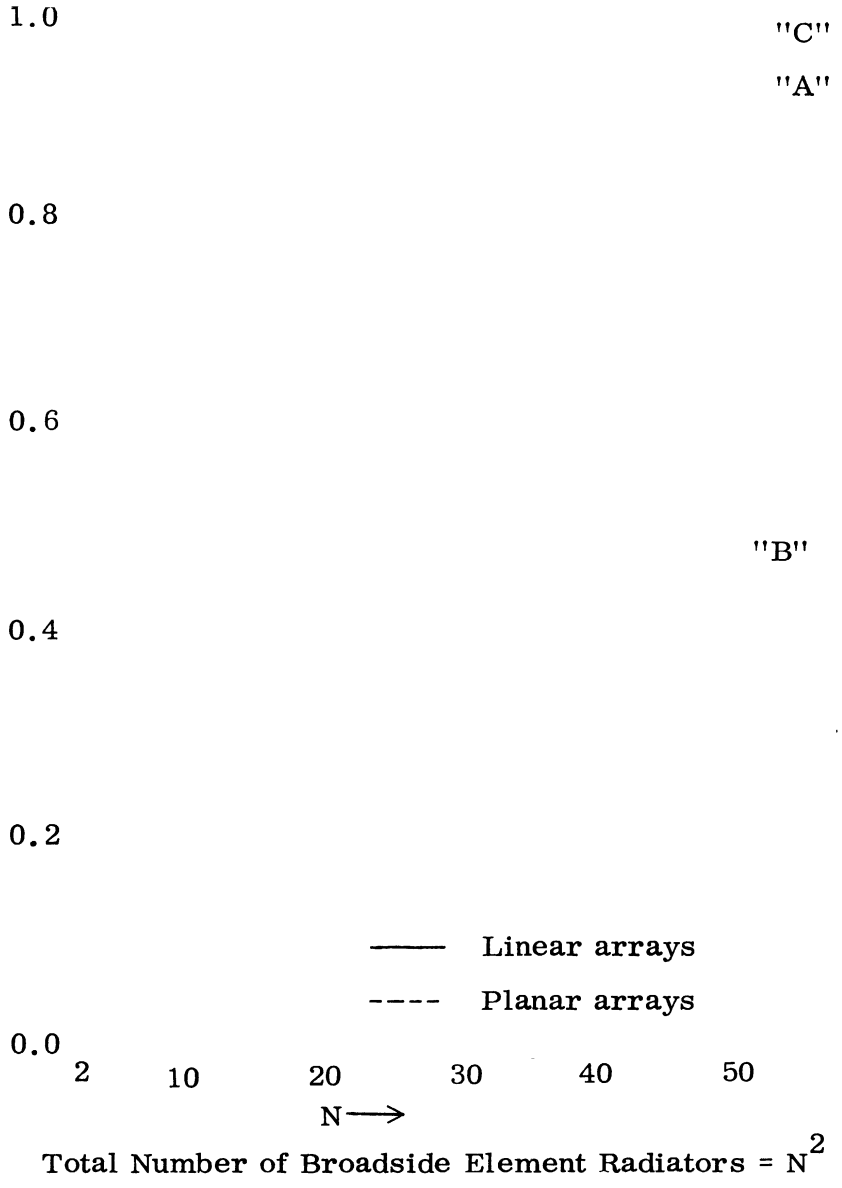

FIG. 3-16a: OPTIMUM ELEMENT SPACING LINEAR AND PLANAR ARRAYS.

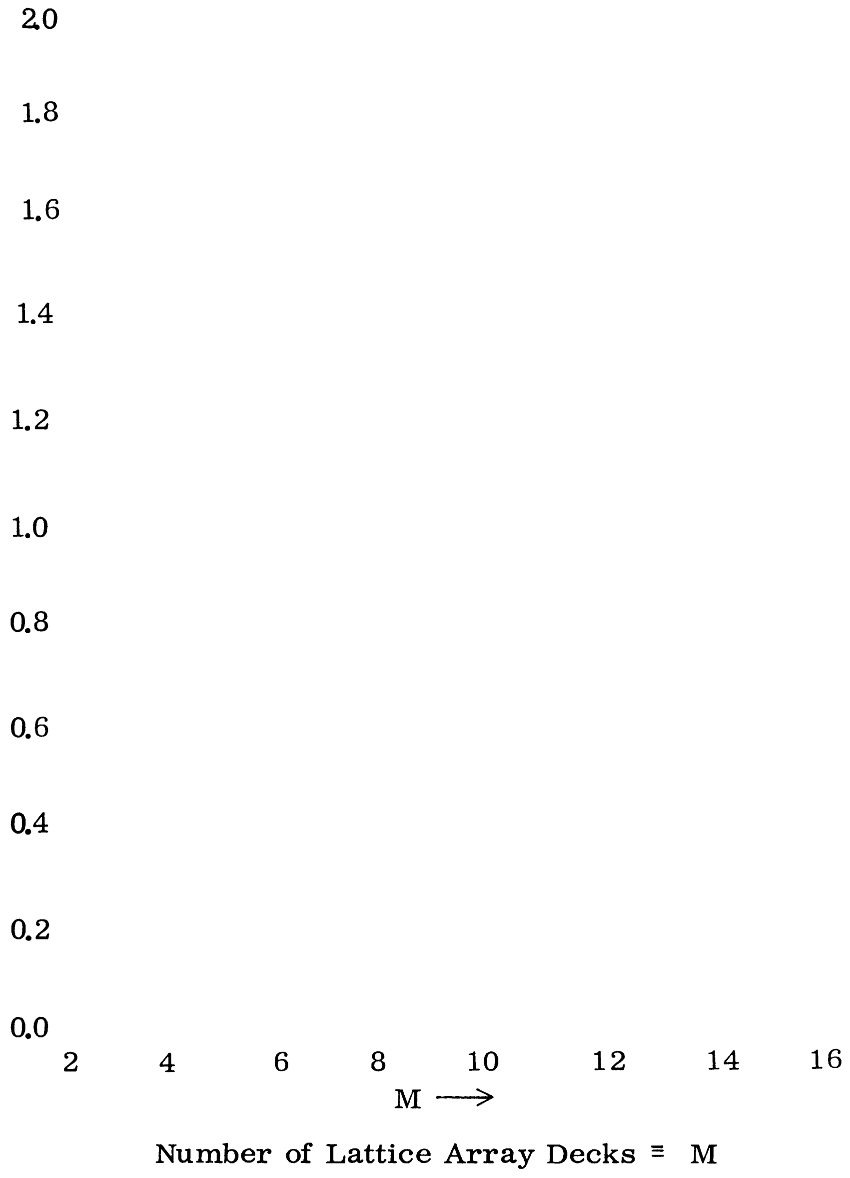

FIG. 3-16b: OPTIMUM ELEMENT SPACING LATTICE ARRAYS.

Also given in Fig. 3-16a are curves for the optimum spacings of planar array elements. These curves of optimum parallel element spacing "A" and optimum collinear spacing "C" resemble the corresponding curves for linear arrays. The asymptotes of the curves are:

1) $A/\lambda \cong .91$ for parallel elements
2) $C/\lambda \cong .99$ for collinear elements.

Figure 3-16b shows the functional behaviors of the three element spacing variables of the lattice arrays. As previously discussed, "A", "B", and "C" denote parallel, endfire, and collinear spacings, and their optimum values are displayed as functions of the number of lattice array decks. The key at the lower right of the figure relates the various curves to the appropriate lattice array cases.

The curve for the optimum value of "B" (endfire deck spacing) resembles that for the optimum element spacing of linear endfire arrays, particularly so as the number of endfire "elements" becomes large. As "M" increases, "B_{optimum}" appears to approach a limiting value similar to that of the linear array case, i.e., $.48\lambda$.

From Fig. 3-16b, it appears that for the range of "M" considered, the optimum values of "A" and "C" are proportional to "M". This contrasts with the planar and linear array cases where "A_{optimum}" and "C_{optimum}" are always restricted to be less than λ. This departure in behavior is related to the grating lobe suppression factor discussed in Section 3.4. A proportionality between the optimum values of "A" and "C", and the values of "M" considered could be expected. As "M" increases, the endfire pattern (which acts as a weighting function on the planar array pattern) becomes more directive, i.e., the main lobe becomes narrower. This results in a larger spatial region over which grating lobes can be effectively suppressed. With grating lobes suppressed over a larger spatial region, the broadside element spacings can be increased to achieve greater directivity, i.e., the main beam can be narrowed while the grating lobes remain suppressed regardless of their new angular position.

It should be noted, however, that from an intuitive standpoint the optimum values of the spacings "A" and "C" will ultimately approach limiting values as "M" becomes large. The basis for this conjecture relates to the array environment as viewed from the location of any given deck in a lattice. As "M" (the number of decks) becomes large, a point is reached where a majority of the array decks are characterized by essentially identical array environments, and further increases in "M" have little effect on these decks. It is at such a point that limiting of the optimum values of "A" and "C" should take effect.

From the curves of Fig. 3-16b, it also appears that as the number of elements along each coordinate axis of a lattice becomes large, the optimum values of "A" and "C" for a given value of "M" become almost identical. Using this fact, a linear approximation to the common curve, and the limiting value of "B_{optimum}", approximations to $\hat{D}$ were calculated for 5x5x20, 10x10x20, and 20x20x20 lattice arrays. In Section 3.4 it was observed that for small deviations of the lattice array element spacings from their optimum values, the deviations of the directivity value from $\hat{D}$ were also small. In view of this fact, in spite of the approximate nature of the values chosen for "A", "B", and "C", one would expect the directivity values calculated for the above lattice arrays to be close to their maximum nominal directivities $\hat{D}$. Based on the various figures of merit calculated for these particular arrays in Section 3.5.3, this does in fact appear to be the case, i.e., the approximate value in each case agrees quite well with the value which would be expected for $\hat{D}$.

Figure 3-17 illustrates the relationship between physical aperture area and number of element radiators for planar and lattice arrays under the condition of maximum nominal directivity. The planar array curve relates aperture area to the number of elements "N" along each of the two coordinate axes of the array (total number of elements in the array is N^2). The lattice array cases are represented by the vertical line "curves". Each lattice array curve is located at that abscissa value corresponding to the number of elements "N" along each of the two coordinate axes of the broadside aperture face of the array. The points defining each curve are then labeled according to the number of decks of each array considered.

The lattice array cases indicated by asterisks (20 deck arrays) are those for which element spacings were approximated from the optimum spacing curves, as discussed above.

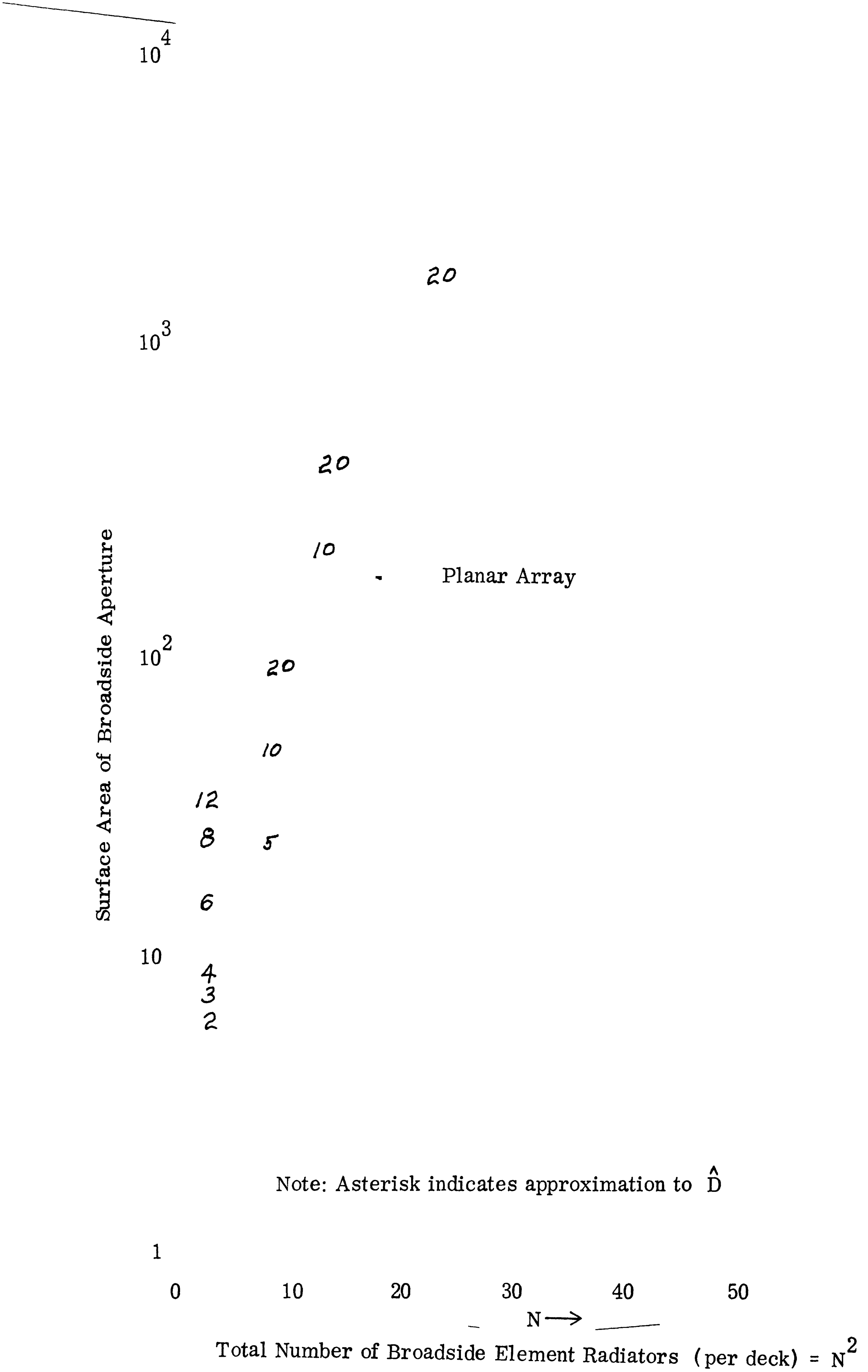

FIG. 3-17: SURFACE AREA OF BROADSIDE APERTURES – PLANAR AND LATTICE ARRAYS – MAXIMUM NOMINAL DIRECTIVITY CASES.

Using Fig. 3-15 and Fig. 3-17, a comparison of the physical aperture areas of planar and lattice arrays with similar directivities can be made. Such comparisons indicate that for similar directivities, a savings of more than 50 percent in aperture area can be obtained by using a lattice array instead of a planar array.

If the number of element radiators in each type of array are compared under the same constraint, it appears that slightly less than twice as many elements are required for the lattice array as compared with the planar array.

3.5.3 Figures of Merit for Maximum Nominal Directivity Arrays

Evaluation of the relative merits of each of the array types which have been studied can be performed more easily by considering certain figures of merit. These quantities, ratios or products of specific absolute array parameters values, provide single numerical "constants" by which one can characterize a given array type. Such "constants" facilitate meaningful comparisons between array types.

3.5.3.a Gain - Beamwidth Product. A standard figure of merit used to characterize antennas is the gain - beamwidth product. This quantity serves not only as a basis for comparison between various antennas, but it provides a working relationship between the beamwidth and gain of a given antenna. ("Gain" as used here refers to the ideal gain which is equivalent to the directivity, i.e., the maximum value of the directivity function $D(\theta, \phi)$.

The gain-beamwidth products for the planar and lattice arrays studied previously are given in Table III-1. As noted in the table, a factor of 2 is included in the values for planar arrays. This is conventional practice and accounts for the bidirectional radiation characteristic of the planar array radiation pattern. This factor of 2 should be kept in mind when comparing planar and lattice arrays. Since the gain-beamwidth product values given in Table III-1 are roughly the same for both planar and lattice arrays, this factor

TABLE III-1: GAIN-BEAMWIDTH PRODUCTS FOR PLANAR AND LATTICE ARRAYS UNDER THE CONDITION OF MAXIMUM NOMINAL DIRECTIVITY.

Array Type	Array Size	Gain-Beamwidth Product (Factor of 2 Included in Planar Array Figures)
Planar Arrays	4x4	26485
	5x5	26487
	10x10	27729
	15x15	26138
	20x20	27135
	25x25	26883
	30x30	28400
	35x35	29165
	40x40	29155
	45x45	29569
	50x50	30782
Lattice Arrays	4x4x2	26729
	4x4x3	26605
	4x4x4	26585
	4x4x6	23967
	4x4x8	24041
	5x5x5	23669
	5x5x10	24126
	5x5x20	22667*
	10x10x10	25664
	10x10x20	26400*
	20x20x20	27,900*

Note: Asterisk indicates use of approximation to $\hat{D}$.

of 2 indicates that for a given beamwidth, a lattice array will have almost twice the directivity of a planar array, or vice versa.

The gain-beamwidth product for a planar array above a ground plane is on the order of 5 percent larger than that for an isolated planar array of the same size. Therefore, the above comparison between a lattice array and a planar array also holds true when comparing a lattice array to a planar array backed by a ground plane.

The gain beamwidth product for a parabolic dish as given by Kelleher (Jasik, 1961, Chapter 12) is 27,000. From Table III-1, it appears that the gain-beamwidth product of a lattice array falls within five to ten percent of that for the parabolic dish.

3.5.3.b Directivity - Aperture Area Relationships . The theoretical relationship between an antenna's gain and physical aperture area as specified by the approximate Fourier Transform relation between the aperture field distribution and the far field radiation pattern is $G \leq 4\pi A_{\lambda^2}$. The notation A_{λ^2} is used to denote the physical aperture area expressed in square wavelengths, and G is again the ideal gain, or directivity. Rearranging the terms of this expression and using the notation "D" for directivity in place of the gain "G", the theoretical maximum of the directivity per unit aperture area is obtained, i.e., $D/A_{\lambda^2} \leq 4\pi$. This quantity (a measure of aperture efficiency) is another figure of merit for an antenna and provides a basis for comparison of the given antenna with the so called ideal of the uniformly illuminated aperture for which $D/A_{\lambda^2} = 4\pi$, and/or with other antennas.

Figure 3-18 summarizes the behavior of $\hat{D}/A_{\lambda^2}$ (maximum nominal directivity per unit area of broadside aperture) for the arrays which have been investigated. Also indicated in this figure for reference purposes, are the values of D/A_{λ^2} for the uniformly illuminated aperture, and the experimental value for large parabolic reflectors. The theoretical value of D/A_{λ^2} for large parabolic reflectors is approximately 9.3, i.e., 75 percent of the value for the uniformly illuminated aperture.

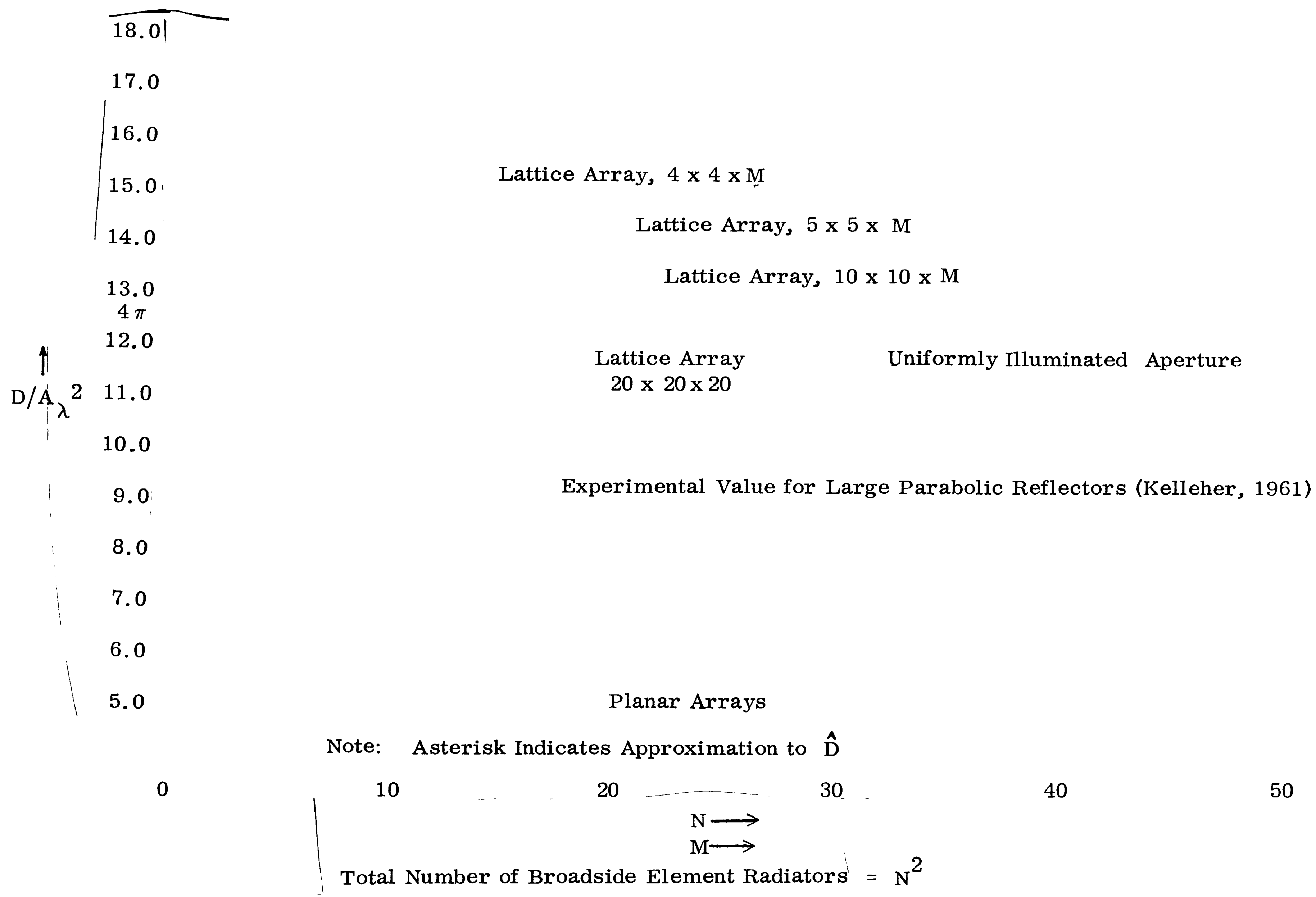

FIG. 3-18: MAXIMUM NOMINAL DIRECTIVITY PER UNIT AREA OF BROADSIDE APERTURE.

The curve for $\hat{D}/A_{\lambda^2}$ for planar arrays is plotted as a function of "N", the number of elements along each of the two coordinate axes of the planar array. From this plot, it appears that $\hat{D}/A_{\lambda^2} \cong 6.0$ for large planar arrays under the condition of maximum nominal directivity. This value is roughly 75 percent of that indicated for the parabolic reflector, indicating that the aperture area of a planar array must be at least 33 percent larger than the aperture area of a parabolic dish of the same directivity.

The curves of $\hat{D}/A_{\lambda^2}$ for the various lattice arrays indicate significantly larger directivities for a given aperture area than in either the planar array or parabolic dish cases. (Each lattice array curve is plotted for a fixed number of deck elements, as a function of the number of decks "M".) The majority of the lattice arrays have values of $\hat{D}/A_{\lambda^2}$ exceeding that of the uniformly illuminated aperture. This fact must of course be interpreted in light of the added complexity of the lattice array which results from its three dimensional nature. Nevertheless, if such complexity is allowable in a given application, then for a given aperture area, a lattice array can attain directivity values comparable to, or larger than that which characterizes a uniformly illuminated aperture of the same physical area.

Comparing the theoretical values of $\hat{D}/A_{\lambda^2}$ which generally characterize the lattice arrays, it appears that a parabolic dish requires about thirty five to fifty percent more aperture area than does a lattice array in achieving identical directivity values. Contrasting the planar and lattice array cases, it appears that a planar array requires fifty to sixty percent more aperture area to achieve the same directivity as a lattice array. (This relationship agrees with the approximate aperture area proportionality ratio of 2:1 for similar values of $\hat{D}$, mentioned earlier in Section 3.5.2 while comparing specific cases of planar and lattice array aperture areas.)

3.5.3.c Directivity Per Unit Volume. The three dimensional geometry of the lattice array suggests the possibility of a directivity-volume relationship in analogy to the directivity - aperture area relation of the previous section. For the various lattice array configurations which have been studied in this chapter, values of the parameter $\hat{D}/V_{\lambda^3}$ have been calculated and are summarized in Table III-2 ($\hat{D}/V_{\lambda^3}$ symbolizes the maximum nominal directivity per unit volume, with the notation V_{λ^3} indicating a normalization of volume to units of cubic wavelengths). The values given in Table III-2 show considerable variation in magnitude, but seem to rapidly approach approximately unity value for larger array sizes.

The concept of a stable value for $\hat{D}/V_{\lambda^3}$ is supported by the data of Sections 3.5.1 and 3.5.2. Referring to Fig. 3-15, the data presented for the various "NxNxM" lattice arrays indicate that if the values of "N" and "M" are increased by a certain factor or factors, the resulting increase in the value of $\hat{D}$ is closely related to the product of such factors. For example, consider the cases of the 5x5x5 and 10x10x10 lattice arrays, where doubling the number of array elements along each array coordinate axis results in an increase in the value of $\hat{D}$ of approximately 9 db, from 25.5 db to 24.5 db.

If an array is sufficiently large, the optimum element spacings A_{optimum}, B_{optimum}, and C_{optimum} should remain essentially constant as the overall array size is increased (see Section 3.5.2). Consequently the "volume" of the array will increase according to the product of the same factors by which "N" and "M" are increased, i.e., V_{λ^3} and $\hat{D}$ will increase by the same factor.

For the range of array sizes which have been considered, the data on $\hat{D}/V_{\lambda^3}$ indicates a proportionality relationship $\hat{D} \sim V_{\lambda^3}$ gives at least a conservative estimate of the maximum directivity attainable with a lattice array of optimally spaced element radiators.

TABLE III-2: MAXIMUM NOMINAL DIRECTIVITY PER UNIT VOLUME FOR LATTICE ARRAY CONFIGURATIONS.

Lattice Array Size	Maximum Nominal Directivity Per Unit Volume $\hat{D}/V_{\lambda^3}$
4x4x2	66.8
4x4x3	25.2
4x4x4	15.1
4x4x6	7.35
4x4x8	4.95
4x4x12	3.1
5x5x5	8.6
5x5x10	3.48
5x5x20	1.55*
10x10x10	3.06
10x10x20	1.41*
20x20x20	1.34*

Note: Asterisk indicates use of approximation to $\hat{D}$.

3.5.3.d Maximum Nominal Directivity Factor. The number of array element radiators required to achieve a given directivity value varies considerably depending on the type of array geometry used. Consider a single class of arrays, i.e., linear endfire, planar, etc. If for each array in the class, the maximum nominal directivity of the array is divided by the number of array elements, then a value which characterizes the maximum nominal directivity per unit element is obtained for each array of the class. This value is a figure of merit for an array, and will be called the maximum nominal directivity factor DF_{mn}. This quantity is defined by the relation $\mathrm{DF}_{mn} \equiv \hat{D}/N_T$, where N_T is the total number of elements in the array which achieves a maximum nominal directivity $\hat{D}$. (From the definition of $\hat{D}$, it can be shown that the quantity DF_{mn} is inversely proportional to the power radiated by an array.)

The quantity DF_{mn} can be considered as a measure, in some sense, of the directive efficiency of an array, i.e., a measure of the number of elements required to attain some given directivity. As such, it facilitates comparison of arrays on a directivity basis. However, it should be noted that directivity is not usually the sole concern in evaluating an array. In particular, the details of the radiation pattern, i.e., main beam shape, sidelobe level, backlobes, etc., can be at least of equal importance. It is of some interest to compare the various classes of arrays on the basis of the values of DF_{mn} which characterize each of them. Because directivity is not the sole concern in evaluating the desirability of an array for a particular application, comparisons between array classes on the basis of the quantity DF_{mn} should not be taken as an absolute indication of the desirability, or lack thereof, of a particular array class.

With these points in mind, consider Fig. 3-19, which gives a graphical representation of the Maximum Nominal Directivity Factor for various classes of arrays as a function of the total number of elements in an array. As is

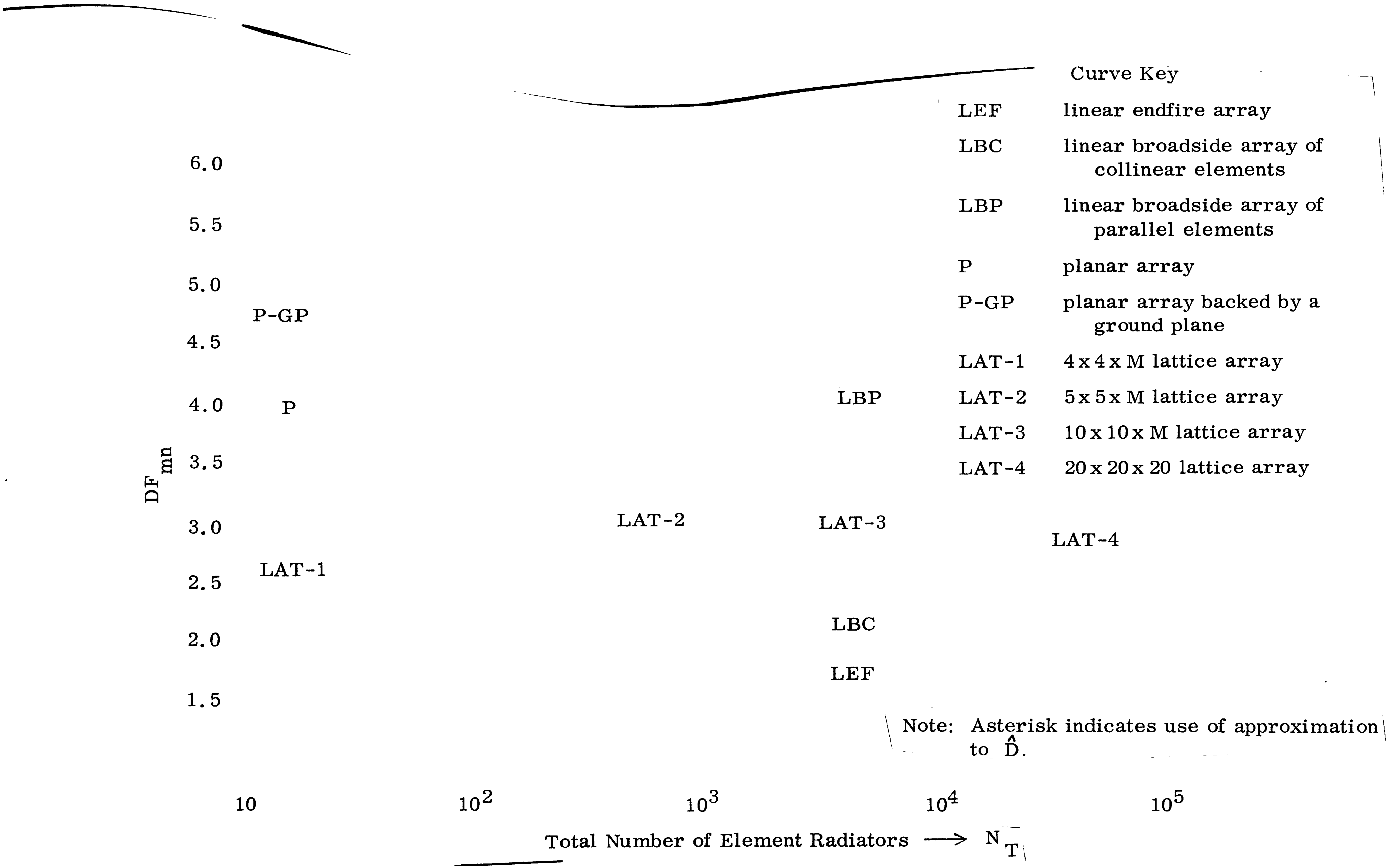

Note: Asterisk indicates use of approximation to $\hat{D}$.

FIG. 3-19: MAXIMUM NOMINAL DIRECTIVITY FACTOR $DF_{mn} = \hat{D}/N_T$.

evident from this figure, the planar array backed by a ground plane is the most "efficient" array type in terms of obtaining some specific directivity value with the smallest number of elements. From this same standpoint, the linear endfire array is the "least efficient" array configuration. The various curves given in this figure, and their interrelationships are largely self explanatory.

In the literature, it is often assumed that the interelement spacings of broadside configurations of radiators is $.5\lambda$, and that of endfire configurations is $.25\lambda$. In some cases such spacings are in fact required to meet certain design criteria, i.e., no grating lobes in real space for a specified range of scan angle, etc. However, in cases where no such design restrictions exist, the use of optimum interelement spacings can result in considerable gains in the directivity value achieved with a given number of array elements. Consider a directivity factor for the various types of arrays which have been studied, but without the constraint of a maximum nominal directivity array configuration. If the element spacings for broadside and endfire elements are chosen as mentioned above, i.e., $.5\lambda$ and $.25\lambda$, then the values of $DF \equiv D/N_T$ are:

1) $DF \cong 1.0$ for linear endfire arrays, and for broadside linear arrays of collinear elements

2) $DF \cong 2.0$ for broadside linear arrays of parallel elements

3) $DF \cong 1.5$ for planar arrays

4) $DF \cong 1.6$ for planar array backed by a ground plane

5) the value of DF for lattice arrays is not very stable for the cases considered, but appears to be bounded roughly between $DF \cong .2$ and $DF \cong .5$.

Comparing these values of DF with the values of DF_{mn} given in Fig. 3-19, it appears that for the LEF and LBC cases an increase of about 3 db in the array directivities can be obtained by using the optimum interelement spacing values. For the LBP case the increase in directivity is about 2.7 db. In the planar array case, the increase in directivity obtained by using optimum interelement spacings is about 4 to 5 db. For a planar array backed by a ground plane, the increase in directivity is between 4.5 to 5.5 db. The increase in directivity obtained in the various lattice array cases is on the order of 8 to 10 db when the elements are optimally spaced.

From these sample calculations it is clear that, other design considerations permitting, the optimally spaced array configurations offer considerable improvement in the attainable directivity values without increasing the number of element radiators.

3.6 Theoretical Lattice Array Radiation Patterns

A computer program was written to compute the radiation patterns of lattice array configurations. Such patterns were needed for comparison with experimental patterns (see Chapter V), and to obtain data on beamwidths and sidelobe levels for this type of array. These theoretical patterns for all arrays except the 4x4x2, 4x4x3, and 4x4x4 lattice arrays are given in Fig. 3-20 through 3-25. The theoretical radiation patterns of the remaining arrays are given along with the experimental patterns in Chapter V.

Beamwidth data for the various array types which have been considered, planar as well as lattice arrays, are summarized in Table III-3. The arrays are grouped into categories according to the indicated beamwidth ranges.

From the various lattice array radiation patterns, it is observed that in general the majority of sidelobes are depressed at least -13 db relative to the main beam maximum. Occassionally a sidelobe of -11 to -12 db is encountered in the arrays having small broadside apertures (small in the sense of the number of deck elements NxN). These larger sidelobes appear to be related to incomplete grating lobe surpression. Surpression of grating lobes becomes more difficult for smaller arrays due to the broader beamwidths and higher sidelobes of the component planar and endfire patterns, which are related to the radiation pattern of the lattice array. In particular, consider the case of the -11 db sidelobe which appears in the "E" plane cut of the radiation pattern of the 5x5x10 lattice array. This sidelobe is oriented approximately 36.5° away from the direction of the pattern main beam. For the optimum broadside element spacings used in computing this pattern, calculation shows that a grating lobe of the component planar array pattern is located approximately 36° away from the main beam in the "E" plane of the array. Thus, the planar array grating lobe is the source of the high sidelobe in this direction.

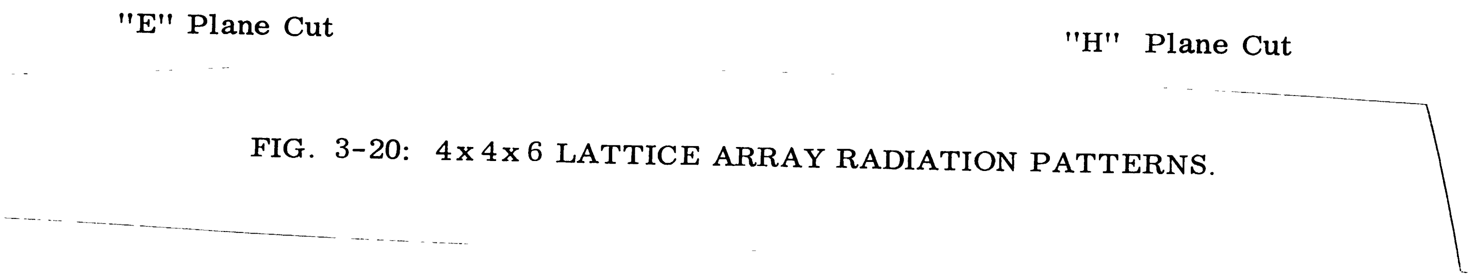

FIG. 3-20: 4 x 4 x 6 LATTICE ARRAY RADIATION PATTERNS.

"E" Plane Cut

"H" Plane Cut

FIG. 3-21: 4x4x8 LATTICE ARRAY RADIATION PATTERNS.

"E" Plane Cut

"H" Plane Cut

FIG. 3-22: 4x4x12 LATTICE ARRAY RADIATION PATTERNS.

"E" Plane Cut

"H" Plane Cut

FIG. 3-23: 5x5x5 LATTICE ARRAY RADIATION PATTERNS.

"E" Plane Cut

"H" Plane Cut

FIG. 3-24: 5x5x10 LATTICE ARRAY RADIATION PATTERNS.

"E" Plane Cut

"H" Plane Cut

FIG. 3-25: 10 x 10 x 10 LATTICE ARRAY RADIATION PATTERNS.

TABLE III-3: HALF POWER BEAMWIDTHS OF PLANAR ARRAYS, PLANAR ARRAYS BACKED BY GROUND PLANES, AND LATTICE ARRAYS UNDER THE CONDITION OF MAXIMUM NOMINAL DIRECTIVITY.

Beamwidth Range	Planar Array			Planar Array GLP				Lattice Array		
	Size	Half Power Beamwidth		Size	h	Half Power Beamwidth		Size	Half Power Beamwidth	
		E-Plane	H-Plane			E-Plane	H-Plane		E-Plane	H-Plane
1^{o} - 2^{o}	50 x 50	1.05	1.15					20 x 20 x 20*	1.1	1.1
	45 x 45	.15	1.25							
	40 x 40	.3	1.4							
	35 x 35	.5	1.6							
	30 x 30	.6	1.8							
2^{o} - 3^{o}	25 x 25	2.1	2.3	20 x 20	.1	2.50	2.65	10 x 10 x 20*	2.2	2.2
	20 x 20	2.6	2.8	20 x 20	.25	2.55	2.65	10 x 10 x 10	3.0	3.0
3^{o} - 6^{o}	15 x 15	3.4	3.8	10 x 10	.1	5.0	5.4	5 x 5 x 20*	4.4	4.4
				10 x 10	.25	5.1	5.5			
6^{o} -10^{o}	10 x 10	5.4	6.2					5 x 5 x 10	6.0	6.25
								4 x 4 x 12	7.0	7.25
								4 x 4 x 8	8.5	8.75
								5 x 5 x 5	8.6	8.6
10^{o} - 17^{o}	5 x 5	11.5	12.5	5 x 5	.1	10.0	11.4	4 x 4 x 6	10.0	10.2
	4 x 4	14.5	16.5	5 x 5	.25	10.6	11.8	4 x 4 x 4	12.0	14.5
								4 x 4 x 3	13.25	15.0
								4 x 4 x 2	14.5	16.5

Note: Asterisk indicates use of approximation to $\hat{D}$.

3.7 Comparison of the Volume - Directivity Relationship for Lattice Arrays and Parabolic Dishes- Sample Calculations

The discussions of previous sections have resulted in comparisons between various parameter values which characterize lattice array configurations, and the identical quantities for parabolic dishes. These discussions have indicated that the lattice array can theoretically attain directivities and gain - beamwidth products which compare quite well with those of the dish, and at reduced aperture areas.

A volume can be associated with the parabolic reflector antenna, just as for the lattice array antenna. While the geometries of these volumes are quite different, a comparison of the volumes associated with each antenna type for a given directivity value is still of some interest. Sample calculations of this type have been performed, and comparisons made between the 4x 4x4 and 10x 10x 10 lattice arrays, and high directivity dishes with $f/d = .5$.

The expressions for the volumes of the two antenna geometries, normalized to units of cubic wavelengths are:

1) $V_D = \frac{\pi}{8} (\frac{f}{\lambda})^3$ for the dish

2) $V_L = (N-1)(\frac{A}{\lambda})(N-1)(\frac{C}{\lambda})(M-1)(\frac{B}{\lambda})$ for the lattice .

The expression used for the directivity of a parabolic dish is (Kelleher, 1961):

$G = 6.4 (\frac{d}{\lambda})^2$ where d is the diameter of the circular aperture of the dish .

The results of the sample calculations are summarized in Table III-4. From these calculations, it would appear that the volume ratio V_D/V_L is approximately the reciprocal of the results for the ratio of aperture areas of the two antenna types with identical directivities.

3.8 The Role of Mutual Coupling in the Array Model.

The expressions and methods used in obtaining the general expression of Chapter II, Section 2.2.4 for the directivity of general array configurations of dipoles made no explicit reference to the mutual coupling effects which are

TABLE III-4: SUMMARY OF SAMPLE CALCULATIONS RELATING LATTICE ARRAY AND PARABOLIC DISH PARAMETERS UNDER THE CONDITION OF IDENTICAL DIRECTIVITY VALUES.

Lattice Array Size	Maximum Nominal Directivity Value $\hat{D}$ (Linear Scale)	Volume		V_D/V_L
		V_L Lattice Array	V_D Parabolic Dish	
4x4x4	152.79	10.0	5.72	.572
10x10x10	2851.5	936	460	.491

known to exist in such arrays. Since the model considered consists of short dipole elements, the current distribution and resultant pattern of an element is not affected significantly by coupling effects, as shown by Chang and King (1967). However, mutual coupling will considerably affect the magnitudes and phases of the excitation currents of the dipole elements, as will be seen from the experimental results of Chapter V, and as has been shown theoretically by Chang and King, (1967). As a consequence of this fact, mutual coupling effects would be of vital concern in implementing a practical feed-network to properly and efficiently excite an array, and the details of such effects must be considered in practical systems. From the standpoint of the radiation pattern and directivity of the array of short dipoles, however, mutual coupling may be neglected in terms of its effects on the excitation coefficients of the array elements, i.e., the excitations symbolized by $V_n e^{j\delta_n}$ in Chapter II. This viewpoint is based on the fact that as an array becomes larger, and the mutual coupling effects more significant, the far field radiation pattern results from the sum of a large number of terms. Thus from an intuitive standpoint, a "large number averaging" type of effect comes into play with a consequent de-emphasis of the effects of mutual coupling on the individual elements. As a consequence of this viewpoint, the element excitations $V_n e^{j\delta_n}$ are assumed known and uniform in the specific arrays considered in Sections 2.3 through 2.3.5, Chapter II. This intuitive position is borne out by the experimental results of Chapter V.

Neglect of the effects of mutual coupling on the element excitations does not infer, however, that the mutual interactions, or coupling effects, do not play a role in the expression for directivity and the related results of this chapter. The maximization procedures carried out on the directivity expression actually represent a minimization procedure for the radiated power, i.e., the numerator of the directivity expression is constant for any given array. The radiated power has been obtained in this investigation by means of the exact integration of the array radiation pattern. From a conceptual viewpoint, the minimization of radiated power is then carried out by altering the shape of the radiation pattern of the array by varying the interelement spacings.

The radiated power of an array is also expressible in terms of the currents and input impedances of the element radiators of an array. The real part of the input impedance between other elements and the given element. Each mutual impedance term has a functional dependency on the distance between the given element and the coupled element. Such distances are of course related to interelement spacing values. In view of these facts, and radiated power can be expressed in matrix notation for an "n" element array as

$$P_r = \text{Re}\begin{bmatrix} I_1 \\ I_2 \\ \cdot \\ \cdot \\ \cdot \\ \cdot \\ I_n \end{bmatrix}^t \begin{bmatrix} Z_{11} & Z_{12}(\rho_{12}) & Z_{13}(\rho_{13}) \cdots\cdots & Z_{1n}(\rho_{1n}) \\ Z_{21}(\rho_{12}) & Z_{22} & Z_{23}(\rho_{23}) \cdots\cdots & Z_{2n}(\rho_{2n}) \\ \cdot & \cdot & \cdot & \cdot \\ \cdot & \cdot & \cdot & \cdot \\ \cdot & \cdot & \cdot & \cdot \\ \cdot & \cdot & \cdot & \cdot \\ Z_{n1}(\rho_{1n}) & Z_{n2}(\rho_{2n}) & Z_{n3}(\rho_{3n}) & Z_{nn} \end{bmatrix} \begin{bmatrix} I_1 \\ I_2 \\ \cdot \\ \cdot \\ \cdot \\ \cdot \\ I_n \end{bmatrix}$$

where ρ_{ij} represents the distance between the ith and jth elements, and is a function of the element spacings for the array.

The minimization of radiated power performed on the basis of an integration of the array radiation pattern is obviously analogous to minimizing the radiated power by considering the above expression for radiated power in terms of the real parts of the input impedances of the array elements. Since this expression is a function of the mutual impedances $Z_{ij}(\rho_{ij})$, a maximization of directivity does in fact, either implicitly or explicitly, always take into account the interaction between the elements of an array, i.e., mutual coupling effects.

In this sense, the mutual coupling phenomena is implicit in the general expression derived for the directivity of an array in Chapter II, and the subsequent numerical investigation of this expression carried out in this chapter.

IV

ARRAY AND ARRAY FEED-NETWORK DESIGN

4.1 General Comments

The main goal of the experimental work which will be described below is to demonstrate that a volume array can in fact be constructed and made to function in accordance with general theoretical principles. An important array parameter whose theoretical and experimental values will be compared, is maximum directivity. In accordance with this goal, the design of the array and associated feed network will follow a relatively simple line, and subordinate such factors as impedance mismatch, bandwidth, and feed-network power losses to the principal objective of this thesis, i.e., demonstration of the physical realizability and directivity properties of a volume array.

Two restrictions are placed on the array and feed-network design. First, available measurement facilities, instrumentation, and basic components dictate a choice of model operating frequency in the range 1.0 - 2.0 GHz. This frequency scaling results in the second restriction, namely that all techniques and devices used in achieving the array model at the model frequency, be translatable without variation in form, to the practical frequency ranges of interest, e.g. 100 MHz. This requirement ensures the applicability of all results to actual systems.

4.2 Array Feed-Network Design

The element "dimensionality" decided upon for the experimental model was 4x4 x4, i.e., a lattice configuration with four element radiators in each of the three coordinate directions. This resulted in a total of 64 element radiators arranged in four successive "decks", each deck having 16 elements. The choice of four element radiators in each coordinate direction was made to obtain a sufficient number of elements in each direction to give some indication of the extent of mutual coupling effects yet still limiting the total number of elements, and the physical array dimensions to manageable sizes.

The amplitude and phase of the excitation of each element of an array with fixed geometry determines the operating characteristics of the array. Attaining a given theoretical distribution of amplitude and phase can, in practice, be quite difficult. External mutual coupling (via the radiating elements of the array), internal mutual coupling (between the various branch lines which feed the array elements) and reflections due to impedance mismatches are all contributing factors which tend to distort an ideal excitation distribution. In view of the purposes of this investigation, some aspects of the problem of excitation distortion due to impedance mismatch were dealt with by using padding (attenuators) to minimize the effects of such mismatches. In particular, impedance mismatches, which would normally be compensated for by the use of matching sections or by design changes altering the impedance levels of various components of the system, were minimized by padding. The problem of excitation distortions due to internal mutual coupling relates mainly to the power dividing network which must be present in the array feed-network. Such effects were minimized by devising a new type of power divider to be described in Section 4.3. This device also tended to minimize certain effects of mismatched array elements. The excitation distortions due to external mutual coupling were considered as inherent in the system and no minimization of this problem was attempted.

4.2.1 Feed-Network Component Arrangement

The arrangement of the components of the feed-network for the volume array is shown in block diagram form in Fig. 4-1. This configuration was arrived at in order to minimize the number of phase shifting elements required for the system while still providing for the progressive phasing of the four successive "decks" of elements.

Although this design does not take full advantage of the output port decoupling properties of the power divider design (see Section 4.3) economic factors required this compromise.

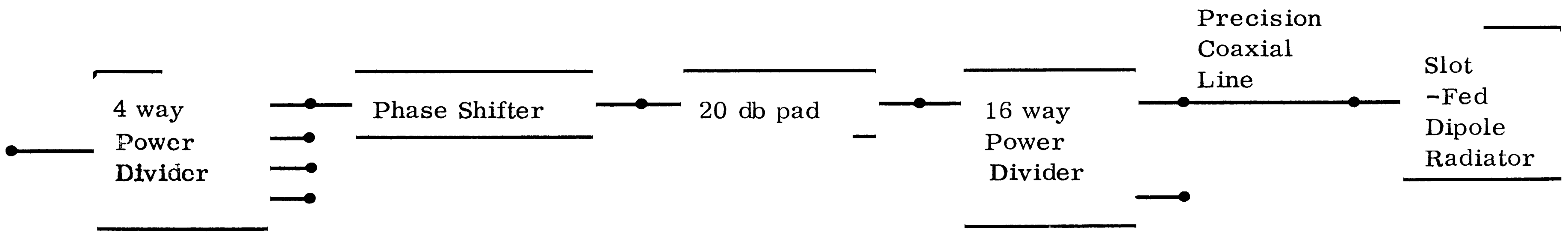

FIG. 4-1 BLOCK DIAGRAM OF LATTICE ARRAY FEED - NETWORK - DETAILS OF COMPONENT ARRANGEMENT SHOWN FOR ONE OF FOUR IDENTICAL CHANNELS.

The details of the feed system are as follows: The input port of the four-way power divider represents the input (output) terminal pair for the array. Each output port of the four-way power divider is connected to an adjustable-length, air-filled coaxial line (Microlab Line Stretcher No. SR-05-N) which serves as the phase-shifting element of the system. Each such line stretcher is then connected to a 20 db pad. The purpose of the pads at this point in the sytem is to provide a constant impedance loading condition for the output ports of the four-way divider. This condition allows the divider to behave as an adder when the system is operated as a receiving system rather than transmitting. In addition, these pads virtually eliminate "ringing" effects due to mismatch between the four-way divider output ports and their final loads, i.e., the 16-way dividers shown in the block diagram (Fig. 4-1). Any reflected signal component will be at least -40 db down in comparison to its original level when returned to the point of origin of the signal.

Each of the 20 db pads is connected by a three foot length of RG 58 A/U coaxial cable to the input of one sixteen-way power divider. The maximum difference in the electrical lengths of these cables is less than 10° at the design frequency of the array. The variance of the electrical length of these cables is 8.4°. The attenuation of each cable is .7 db. The output ports of the sixteen-way dividers are each connected to an element radiator of the array by a fifteen-foot length of RG 58 A/U coaxial cable. The maximum difference in the electrical length of any two such feed lines is less than 10° at the design frequency of the array. The variance of the electrical lengths of the 64 feed lines is 2.8°. The attenuation related to the losses which occur over the length of a feed cable is 3.6 db. This attenuation results in a "padding" effect between each radiating element and the power divider output port connected to it via the feed line. This padding effect is desirable in order to minimize "ringing" effects in the feed lines, i.e., multiple reflections due to mismatch conditions at both ends of the feed line.

The actual feed system, including the details of the mounting arrangements for the power dividers and line stretchers, can be noted in the photograph shown in Fig. 4-2. Half of the total number of components are visible.

4.3 Radial Strip Line Power Divider*

The restrictions on the array-system design discussed in Section 4.2 led to fabrication of the power dividing network from strip transmission-line materials. The economy, versatility and comparative ease of fabrication of microwave components from stripline material is well known (Sanders Associates, 1956; Barrett, 1955; Arditi, 1955; Dukes, 1958; Jasik, 1961). Conventional strip line power dividers, or "finger type" dividers, such as the one shown in Fig. 4-3, have several undesirable features for the application considered here. First, unless the output lines are sufficiently spaced, coupling between adjacent lines can be significant, i.e., the internal coupling problem mentioned above comes into play. Spreading the output port lines will reduce this coupling, but add considerably to the physical size of the device. Since a large number of output ports will be required for most moderate sized lattice arrays, this structure is not very attractive. The use of several dividers in series, as shown in Fig. 4-4, to decrease the overall width of the divider network does not seem desirable either. Such an approach would produce nonuniform coupling, and would reduce the effective isolation obtainable by using a large number of ports in parallel, i.e., an averaging of a large number of small terms. In addition, the length of the divider network would be considerably increased.

Other drawbacks to the use of the conventional divider configuration are the increasing difficulties encountered in attempting to join all of the output lines with the main feed line as the number of lines becomes large, i.e., increasing constructional accuracy requirements for impedance matching, amplitude balance and phase uniformity.

A simple solution to these problems was devised using the principles of radial transmission lines combined with strip line techniques. The symmetrical

*Patent Disclosure to be filed.

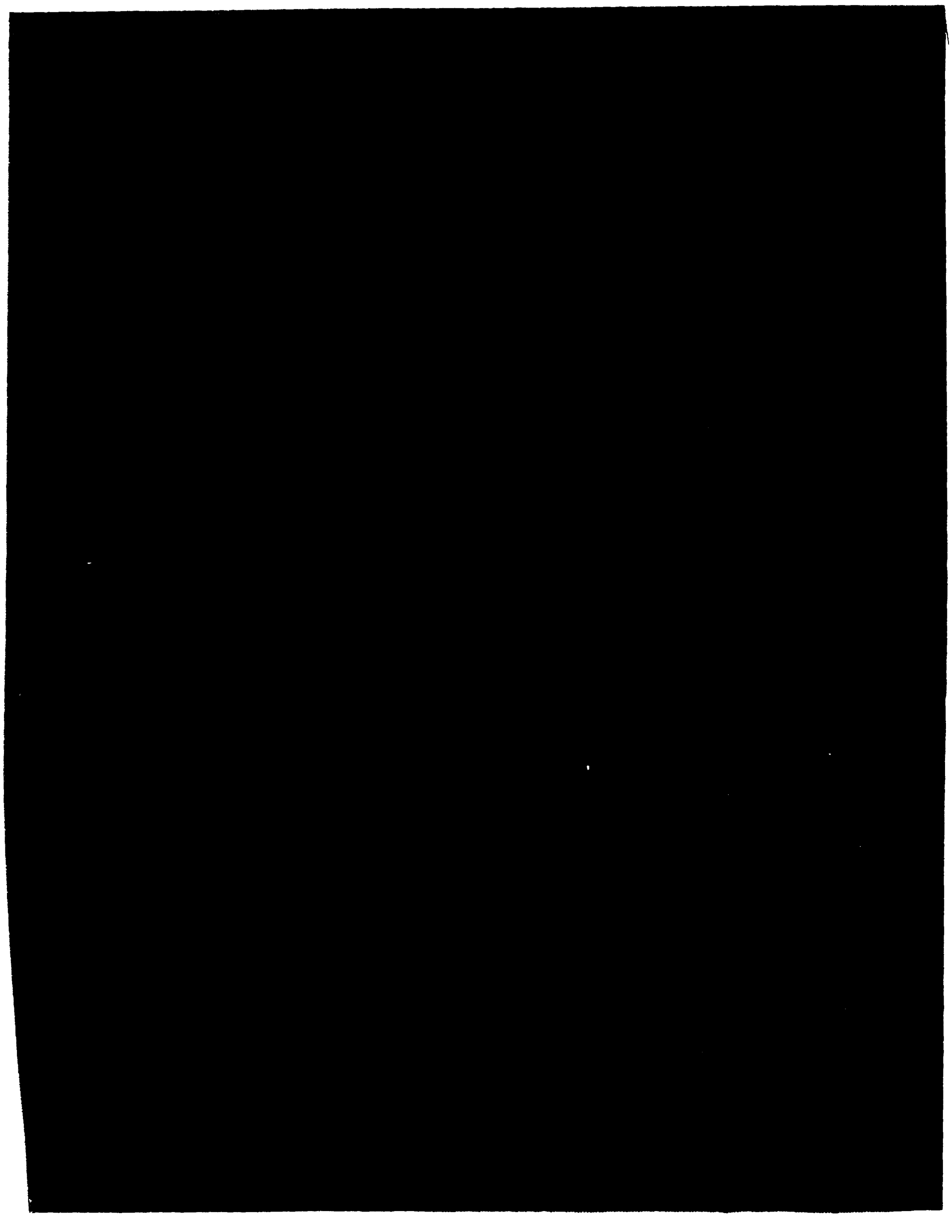

FIG. 4-2: POWER DIVIDER FEED NETWORK FOR A 4x4x4 LATTICE ARRAY.

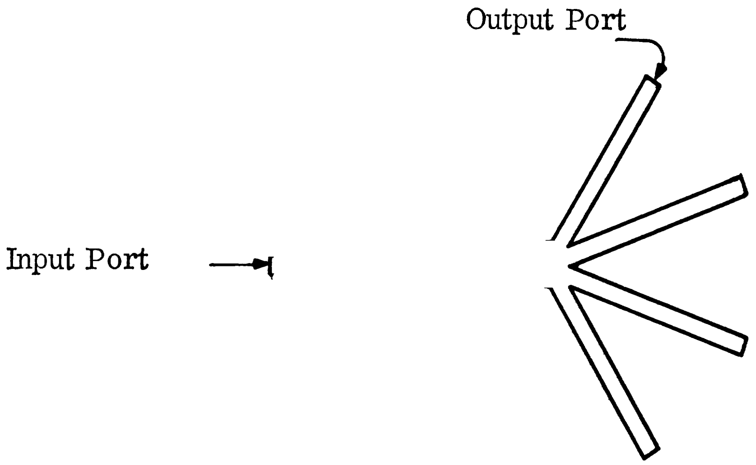

FIG. 4-3: CONVENTIONAL "FINGER TYPE" STRIP TRANSMISSION-LINE POWER DIVIDER.

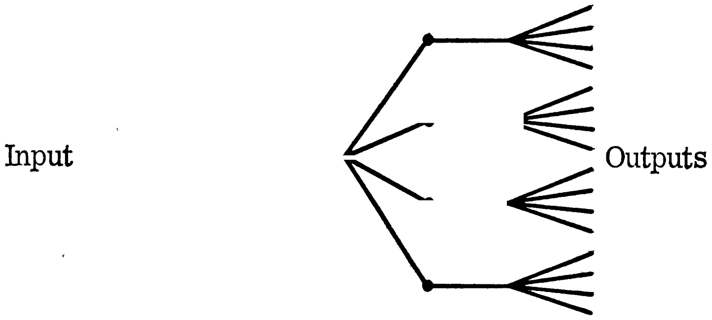

FIG. 4-4: SERIES ARRANGEMENT OF FIVE CONVENTIONAL STRIP LINE POWER DIVIDERS TO GIVE 16-WAY DIVISION.

nature of a center-fed disc configuration provided the basis for the design of a novel type of power divider. The nature of the device construction may be compared to two cylindrical cavities placed back to back (Fig. 4-5). The cavity plates are in this case, the circular sheets of copper material which are bonded to opposite sides of a dielectric material. The upper cavity is center fed, and output ports are coupled symmetrically around the circumference of the cavity. A qualitative theory of operation on which the engineering design of the divider was based is as follows.

Energy coupled into the upper cavity at the center propagates radially outward with cylindrical symmetry. At the common circumferential boundary between the upper and lower cavities, some of the propagating energy couples into the lower cavity and, assuming a uniform boundary, propagates toward the center of this lower cavity, again with cylindrical symmetry. A double stub reactive tuner, connected to the tuning port mounted at the center of the lower cavity, controls the phase of energy reflected back to the upper cavity. This feature allows for limited control of the reactive component of the input impedance of the device, i. e., the impedance seen at the center input port of cavity No. 1. Complete tuning is not possible since an amplitude discrepancy between the natural component of reflected energy and the controlled component is inherent in the system design, i. e., the controlled component propagates over a longer path and is therefore subject to greater attenuation.

The output ports placed around the circumference of the upper cavity are symmetrically located and spaced at about a half wavelength or less from each other. Loads connected to these ports act in parallel, and may be compared to an equivalent surface impedance for the upper cavity, particularly as the number of output ports increases and/or the spacing between ports (normalized to a wavelength) decreases. The radial transmission line acts as an impedance transformer and can be designed to transform this equivalent surface impedance to an appropriate level to achieve a matched condition at the input port of the device.

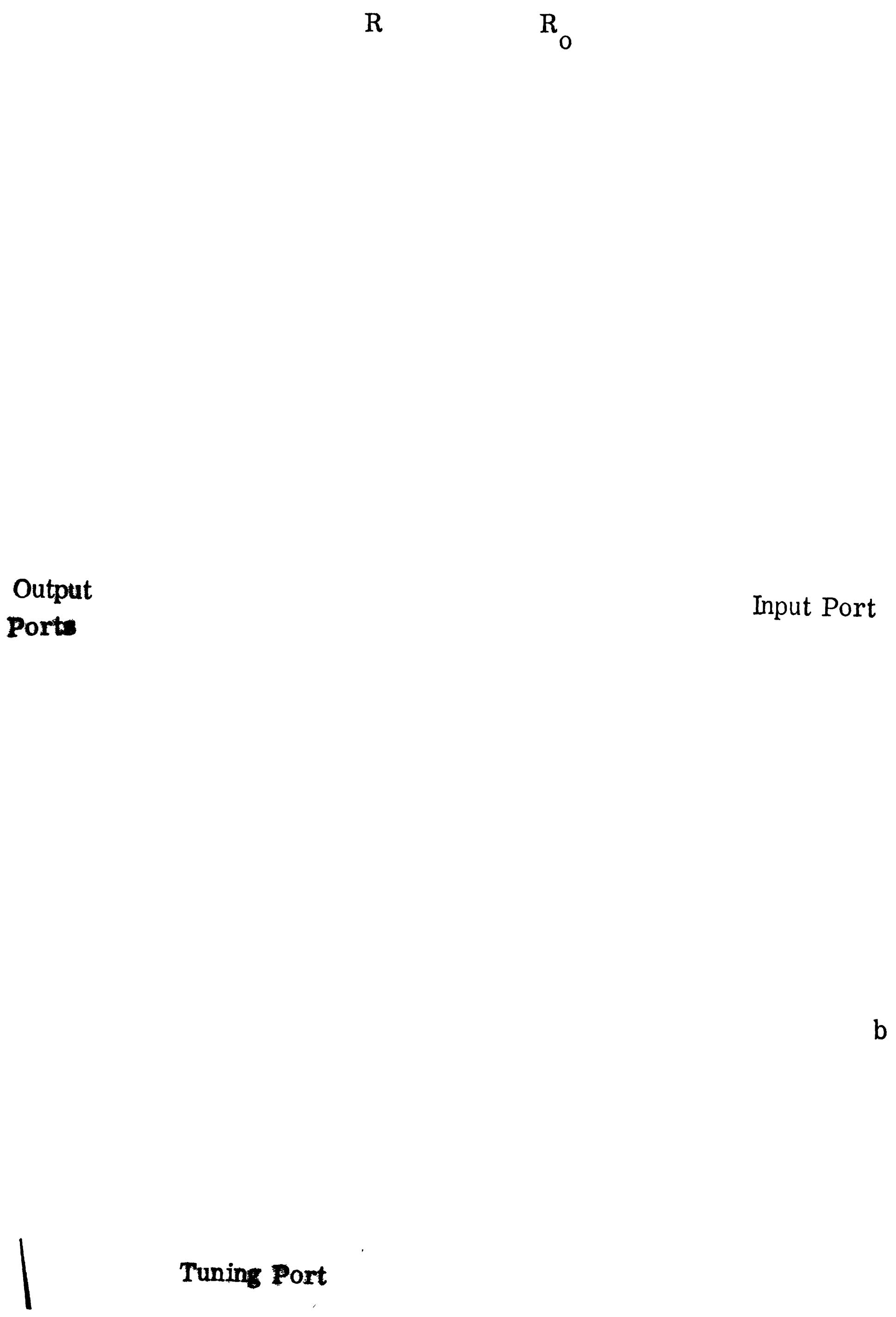

FIG. 4-5 4-WAY STRIP RADIAL TRANSMISSION-LINE POWER DIVIDER.

The symmetry of this device suggests that extremely uniform amplitude and phase properties should be obtainable at each output port while construction methods are kept extremely simple and straightforward. That this is, in fact, the case, is borne out by the data presented below. In addition, a large number of output ports can be located along the outer circumference of the circular device, and the number can be increased significantly more for a given change in the overall size of this divider than for a "finger type" divider. Depending on specific requirements for a particular application, the diameter of the device can be adjusted to yield a wide range for the number of output ports. As the design frequency decreases, the number of output ports possible also increases since the diameter of the device becomes proportionately larger.

In the development work which was performed only those operational characteristics of a power divider necessary to produce an operating model of a volume array were of immediate interest. Therefore, only those aspects of theoretical analysis and experimental design which were necessary to achieve a functioning power divider having good phase and amplitude uniformity of the outputs, and an acceptable input impedance level, were performed. The following material describes the qualitative analysis and design procedures carried out in arriving at such a model.

4.3.1 Engineering Design Calculations

In order to obtain a basis for choosing some of the basic design parameter values needed to construct an experimental model of a radial line divider, calculations were performed for a theoretical model which gives an approximation to the upper cavity of the divider as described in Section 4.3. This model is the cylindrical cavity radial transmission-line described and analyzed by at least two authors (Marcuvitz, 1951 and Harrington, 1961). Figure 4-6 shows the details of this configuration. Since the value "b", which is the distance between the guiding plates, is very small compared to wavelength in this particular case (stripline material thickness b = 1/8" and wave length λ = 9.45"), only E type modes will propagate. The principal mode is a TEM or transmission-line mode. The dominance of this mode is due to the following factors:

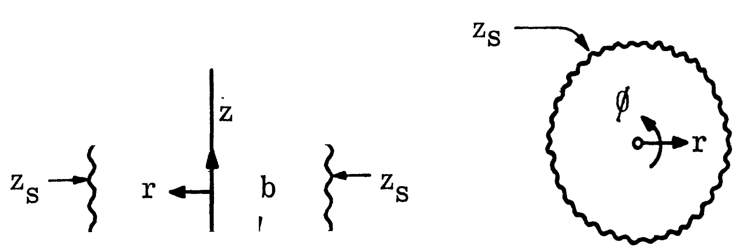

Side View

Top View

FIG. 4-6: CYLINDRICAL RADIAL TRANSMISSION-LINE, CENTER-FED, WITH CIRCUMFERENTIAL SURFACE IMPEDANCE z_s .

(1) $b/\lambda << 1$; (2) the symmetric excitation at the center of the disc; and 3) the symmetry of the circumferential surface load impedance. Using this model, the expression for the input impedance seen at the center of the line is

$$z(r)=z_0(r)\,\frac{\left[Ct(x,y)+j\,\frac{z_0(r_0)}{z(r_0)}\,\zeta(x,y)\right]\left[j\,\frac{z_0(r_0)}{z(r_0)}\,Ct(x,y)\right]}{\left[1+\frac{z_0(r_0)}{z(r_0)}\,Ct(y,x)\right]^2},$$

where

$z(r)$ is the input impedance seen at the center of the line, r being the radius of the inner line of the coaxial feed,

$z_0(r)=\sqrt{\frac{\mu}{\epsilon}}\cdot\frac{b}{2\pi r}$ is the characteristic impedance of the line of thickness b, permittivity ϵ, and permeability μ, at radius r,

$$Ct(x,y)=\frac{J_1(y)N_0(x)-N_1(y)J_0(x)}{J_1(x)N_1(y)-N_1(x)J_1(y)}$$

$$\zeta(x,y)=\frac{J_0(x)N_0(y)-N_0(x)J_0(y)}{J_1(x)N_1(y)-N_1(x)J_1(y)},$$

$x = kr,\quad y = kr_0,\quad k = 2\pi/\lambda$ and

where the J_i and N_i are the ordinary Bessel functions of the first and second kind, and $z(r_0)$ is the equivalent surface load impedance of the line located at radius r_0 from the center of the disk.

A computer program was written to evaluate this input impedance expression as a function of the radius of the line i.e., as a function of r_0, with r, $z(r_0)$ and f_0 (i.e., λ) as parameters. The results of these computations, given in numerical and graphical form, displayed the real and imaginary parts of the input impedance in separate groups. The resolution of the function $z(r)$ was determined by specifying an incremental change Δr_0 for computing successive values of $z(r_0)$.

Calculations were performed for the following data sets:

$$\left.\begin{array}{l}
1)\ r = 1/32'', \quad f_o = 2.0\ \text{GHz}, \quad \Delta r_o = \lambda/8, \quad r_{o_{max}} = 4\lambda \\
2)\ r = 1/16'', \quad f_o = 2.0\ \text{GHz}, \quad \Delta r_o = \lambda/8, \quad r_{o_{max}} = 4\lambda \\
3)\ r = 1/32'', \quad f_o = 2.0\ \text{GHz}, \quad \Delta r_o = \lambda/25, \quad r_{o_{max}} = 4\lambda
\end{array}\right\} \quad Z(r_o) = \begin{array}{l} .25,\ .50,\ .75,\ 1.0,\ 2.0, \\ 3.0,\ 4.0,\ 5.0,\ 10.0,\ 15.0,\ 20.0,\ 50.0 \end{array}$$

$$\left.\begin{array}{l}
4)\ r = 1/32'', \quad f_o = 1.0\ \text{GHz}, \quad \Delta r_o = \lambda/25, \quad r_{o_{max}} = 4\lambda \\
5)\ r = 1/16'', \quad f_o = 2.0\ \text{GHz}, \quad \Delta r_o = \lambda/25, \quad r_{o_{max}} = 4\lambda \\
6)\ r = 1/16'', \quad f_o = 1.0\ \text{GHz}, \quad \Delta r_o = \lambda/25, \quad r_{o_{max}} = 4\lambda
\end{array}\right\} \quad Z(r_o) = 2.0,\ 3.0,\ 4.0,\ 5.0$$

Samples of typical output data are given in graphical form in Fig. 4-7.

The output data from these computations were principally used to determine the range of values for the divider diameter over which the behavior of the driving point impedance of the device fell into a useful range, i.e., the magnitude of the real part of the input impedance at least comparable to the imaginary part, or preferebly larger, and the magnitude of the total impedance resulting in a reasonably good match to a 50 Ω coaxial line.

After comparing all of the output data sets and the variations therein, the range chosen for the divider radius was approximately $.5\lambda < R_0 < 3\lambda$.

4.3.2 Experimental Design

The materials from which the divider was fabricated were chosen on the basis of economy and the ease with which they could be handled. The basic materials and components used were:

1) Copper clad printed circuit laminate - brand name, Tellite
   Copper sheet thickness: .0028 inches
   Dielectric thickness: .125 ± .002 inches
   Relative Dielectric permittivity: 2.32 ± .01 to 4.3GHz
2) N type connectors: Types 35000, UG-536 A/U and UG-58 A/U
3) Silver conductive expoxy E - Solder No. 3025.

The divider design described in Section 4.3 as two cylindrical cavities with a common guiding plate, was arrived at for two principal reasons; 1) it is desirable to have a power dividing network which is completely shielded as to minimize all radiation effects, and 2) the difference in the

* In all of the above plots the abscissa units are r_o/λ, and $f_o = 2.0$ GHZ, $r = \frac{1}{32}$", $Z = Z(r_o)$.

FIG. 4-7a: SAMPLE DATA FROM CALCULATIONS OF RADIAL TRANSMISSION-LINE INPUT IMPEDANCE:

* In all of the above plots the abscissa units are r_o/λ, and $f_o = 2.0$ GHZ, $r = \frac{1''}{32}$, $Z_s = Z(r_o)$.

FIG. 4-7b: SAMPLE DATA FROM CALCUALTIONS OF RADIAL TRANSMISSION-LINE INPUT IMPEDANCE.

diameter of the outer and inner plates of a divider results in a circular aperture through which the upper and lower radial transmission-lines are coupled. (See Fig. 4-8 which shows a top view and disassembled view of a 16-way radial-line divider, and Fig. 4-5.) This coupling aperture allows some "tuning-out" of the reactive component of the driving point impedance at the input of the upper cavity. This tuning is accomplished by connecting a double stub tuner to the tuning port of the lower line. The width of the coupling aperture was indirectly determined by choosing the outer diameter of the device to be as small as construction features allowed.

Since the two halves of the device must be fastened together, a ring of 32 equally spaced No. 4-40 bolts and nuts was fastened around the outer circumference of the divider. It was initially thought that these bolts would also provide an effective shorting ring. However, as will be noted later, the spacing between the bolts proved too large compared to a wavelength and the shorting action of the ring was not very effective. This fact led to the use of an adhesive backed aluminum tape, wrapped around the circumference of the disc, to short the two outer plates together in the final models (Fig. 4-9).

The output and input port couplings were accomplished by the standard right-angle coupling procedure for a coaxial line into a stripline network (again see Fig. 4-9).

The mechanical connection of the N connectors to the stip line posed another problem. The normal method of fastening such connectors with bolts and nuts was not possible since the bolt clearance holes and the bolts themselves would have to go through the center conductor of the transmission - line, which would disturb the fields and the symmetry of the device both at the center and around the edge.

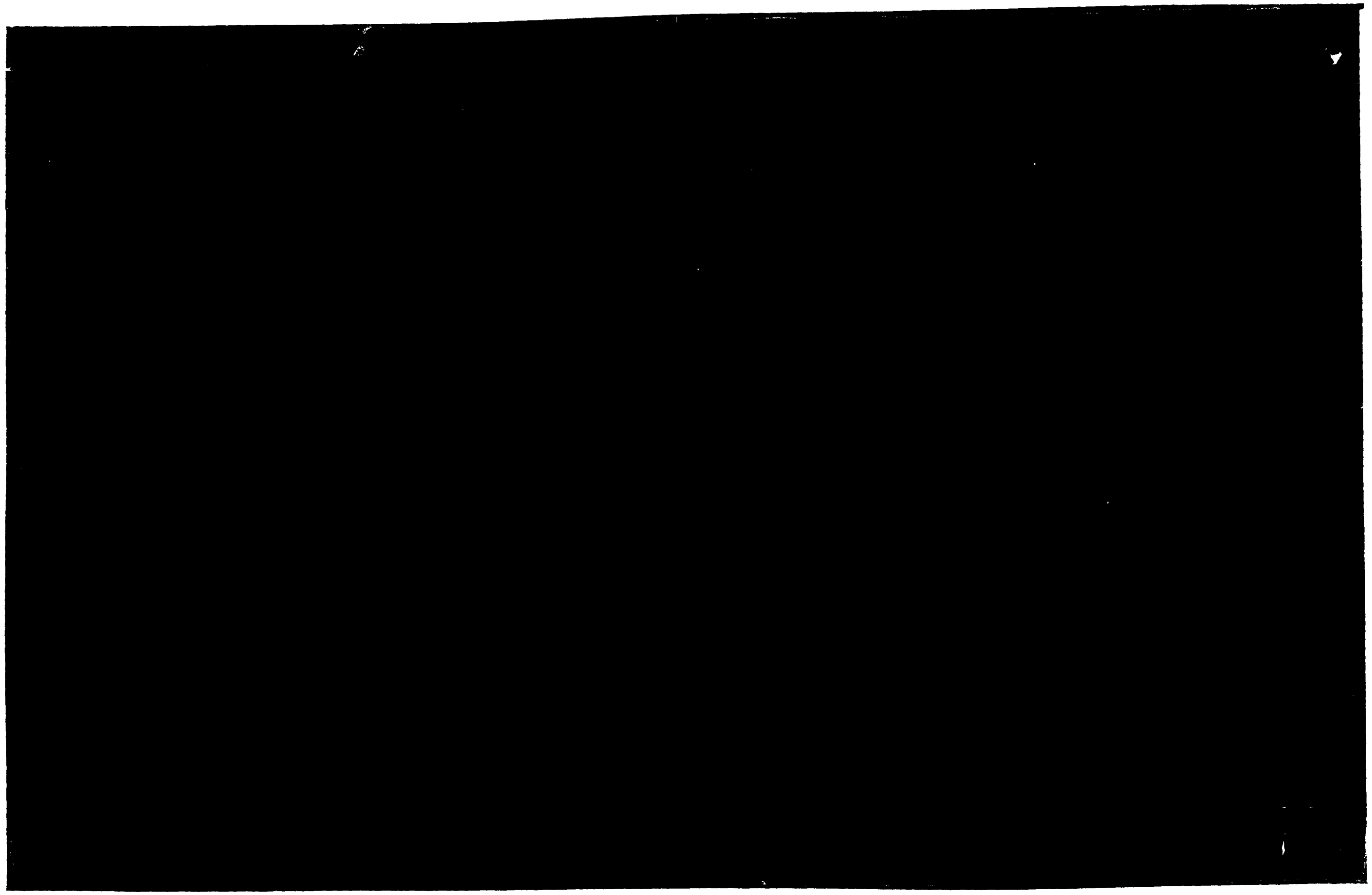

FIG. 4-8: SIXTEEN-WAY RADIAL STRIP TRANSMISSION-LINE POWER DIVIDER. Top view and disassembled (internal) view.

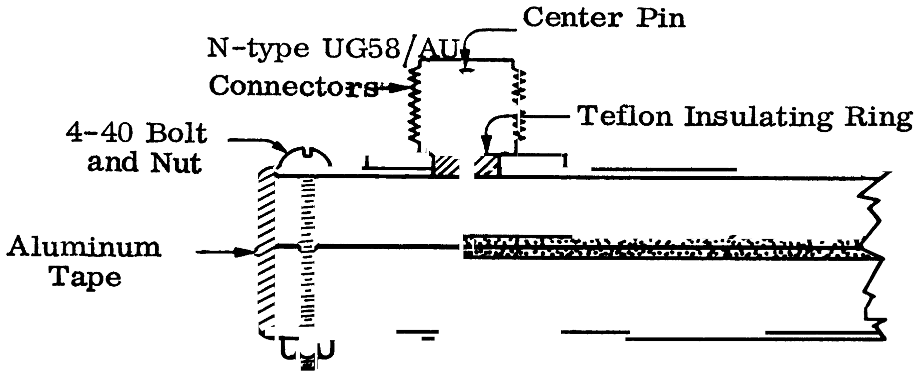

FIG. 4-9: CROSS SECTION VIEW OF OUTPUT PORT JUNCTION METHOD FOR CONNECTING COAXIAL CONNECTOR TO STRIP RADIAL TRANSMISSION-LINE INNER DISC. Also shown are the general construction features of the fastening nut and bolt, shorting tape and coupling aperture.

A solution to this problem was found by using silver conductive expoxy solder to bind the connector to the divider body. This material provided a good conducting and strong (2500 psi tensile strength) bond of the connector body to the outer plate of the radial line, and also of the center pin of the connector to the inner plate of the line. Ordinary solders, even low temperature mixtures, were not practical since the heat necessary for the solder to flow was sufficient to damage the bond of the copper sheet to the center strip of dielectric. In addition, noticeable "bubbling" and general warpage of the strip line occurred as a result of such heat.

The silver epoxy solder proved to be a very effective bonding material, particularly when the materials which were bonded together were immediately subjected to a few hours of heat curing at temperatures in the neighborhood of 110°F to 130°F. These temperatures were sufficiently low to prevent heat damage to the stripline materials.

The first design model, a four way divider, was constructed as shown in Fig. 4-10. The inner disc radius chosen was $R_0=4.725''$, which gave a normalized radius of $R_0/\lambda_0 = 1.7$ for $\lambda_0=2.77''$ (a frequency of 2.8 GHz) (See Fig. 4-7a and 4-7b with $R_0 \equiv r_0$). This choice was made in order to allow the radius of the device to be effectively changed over a range of roughly 5:1 by varying the frequency over a similar range with 2.8 GHz as the approximate center frequency. Additional reasons for this choice were related to equipment availability.

The rectangular geometry of the outer plates of the divider, and the values for the two rectangular dimensions were a result of the fact that stripline material is delivered in rectangular sheets 16"x22 1/2". One such sheet, cut in half, formed the two halves of the divider. At this point in the development it was still not clear that the ring of fastening bolts would not produce an effective shorting boundary. However, the measurements discussed below clearly indicated the ineffectiveness of this ring as a short circuit.

Since the goal of the design procedure was to produce an operating radial-line divider with only those properties of immediate interest, measurements were performed in the following manner. The input port of the four way divider

FIG. 4-10: 4 WAY STRIP RADIAL TRANSMISSION - LINE POWER DIVIDER.

was connected to the end of a slotted-line impedance measurement setup, as shown in Fig. 4-11. The four output ports of the divider were terminated in 50 ohm loads, and a double stub tuner was connected to the tuning port of the divider. Then in incremental steps over the frequency band from 1.0 GHz to 5.2 GHz, the following proceedures were carried out for each frequency. The radial line divider was tuned by means of the double stub tuner, to obtain a minimum VSWR. After obtaining the minimum VSWR, the standard double-null measurements needed to determine the input impedance of the device were made. Then the output power level of each output port of the divider was measured (see Fig. 4-12) with the input power level referred to 0 db. Ideally, the power level of each port of a four-way divider should be -6.0 db referred to the input power.

The results of these measurements are summarized by the values shown in Table IV-1 , and the accompanying Smith chart (Fig. 4-13). From these data it is evident that the ring of bolts becomes less effective as a shorting surface as the frequency increases, and therefore the rectangular geometry of the outer plates results in a lack of symmetry with respect to the center input port. These effects are implied by the deviation of the values of the power at the output ports from the -6 db ideal, and the nonuniformity of these output power levels from port to port. Also, the large discrepancies and nonuniformities essentially disappear at $f = 1.0$ GHz. At this frequency the divider has an acceptable input impedance level, corresponding to a mismatch loss of about -.33 db , and the output power levels are quite uniform, differing from the ideal value by about 1 db. The radius of the inner disc of the divider at this frequency gives a normalized radius of $R = .61$ which coincides with the first peak of the real part of $Z(r)$ indicated in the theoretical computations of Section 4.3.1.

Since a physically small divider is desirable, and since the power dividing and input impedance characteristics of the device at 1.0 GHz seemed adequate, no further steps were taken to investigate the possible modes of operation and 1.0 GHz was chosen as the frequency on which to base the line dimensions for experimental scaling purposes. Table IV-2 and Fig. 4-14 summarize the additional data taken to determine output port isolations, and

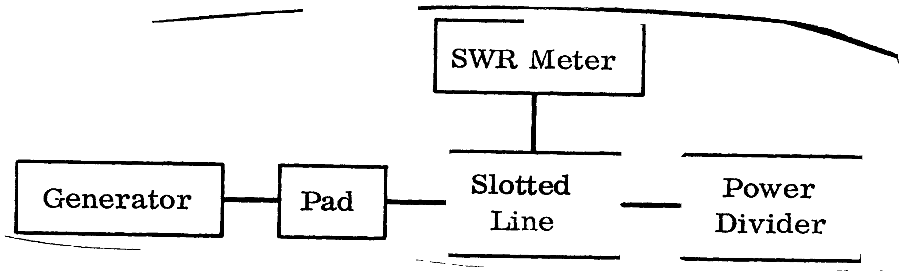

FIG. 4-11: IMPEDANCE MEASUREMENT BLOCK DIAGRAM.

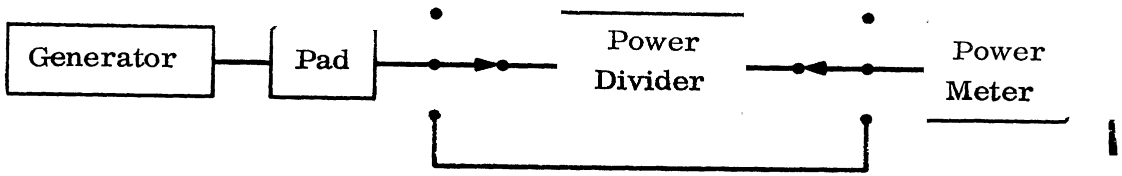

FIG. 4-12: POWER MEASUREMENT BLOCK DIAGRAM.

TABLE IV-1: DESIGN MODEL - FOUR WAY DIVIDER

Freq. GHz	Input Port SWR*		Output Port Power -db (referred to input)			
		Port No	1	2	3	4
5.2	1.08		14.4	14.0	14.4	14.4
4.8	3.40		17.8	27.0	27.0	25.5
4.4	1.25		13.2	13.8	13.0	13.2
4.0	2.80		16.5	15.2	22.5	16.0
3.6	1.8		32.4	33.7	31.8	28.6
3.2	2.75		20.7	12.2	21.3	12.1
2.8	1.73		9.4	13.9	9.8	13.5
2.4	5.6		36.5	30.4	35.0	27.0
2.0	4.7		12.5	15.4	12.5	15.6
1.6	4.8		19.8	19.2	19.6	19.7
1.2	1.15		11.9	11.2	11.7	11.3
1.0	1.75		7.1	7.2	7.0	7.3

*All ports terminated in 50 ohm loads.

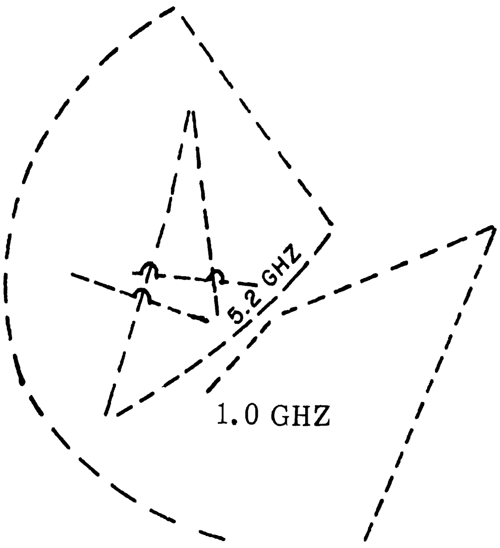

FIG. 4-13: INPUT IMPEDANCE PLOT. PROTOTYPE 4-WAY STRIP RADIAL TRANSMISSION-LINE POWER DIVIDER.

MISSING
PAGE

phase uniformity of the four-way device.

This four-way divider was next modified by adding four additional output ports, resulting in an eight-way power divider. This and the subsequent modification to a 16-way divider were performed to determine the sensitivity of the divider properties to changes in the output port spacings and the "effective surface impedance" which they represented. The choice of the 4 - 8 - 16 progression was based on the needs of the array, i. e., a 64-element array (Section 4. 2).

As can be seen from Table IV-3 and Fig. 4-15, the properties of the 8-way divider did not differ substantially from those of the 4-way divider. The input impedance mismatch, and uniformity of output signal phase and amplitude improved somewhat over those of the 4-way divider.

Finally, eight more output ports were added, resulting in a 16-way divider: the measured properties of this model are summarized in Table IV-4 and Fig. 4-15. The input impedance level results in a poorer match than in the 4-and 8-way divider cases, but not objectional for present purposes. This mismatch represents a power transmission loss of about -1. 1 db. The output port signal phase and amplitude uniformity are again very good, the maximum deviation of amplitude and phase between any two ports approaching the limits of experimental accuracy, i. e., 3^o and . 1 db. The maximum coupling between any two output ports is about -13 db.

The measurements of the output port phase uniformity summarized in the tables noted above, were carried out with the equipment setup symbolized by the block diagram of Fig. 4-16. This is a standard measurement technique based upon the addition of an unknown signal to a signal of known and controllable phase, to produce a null, i. e., a null results when the signals are 180^o out of phase. A double null averaging technique was used here, as in the impedance measurement procedures, in order to decrease the measurement inaccuracies due to noise effects.

16 Port

8 Port

FIG. 4-15: INPUT IMPEDANCES OF MODIFIED PROTOTYPE STRIP RADIAL TRANSMISSION-LINE POWER DIVIDER.

TABLE IV-2: PROPERTIES OF FOUR-WAY RADIAL-LINE DIVIDER, PROTOTYPE MODEL, FREQUENCY OF OPERATION = 1. 0 GHz

Input Port SWR = 1. 75 (All ports terminated in 50 ohm loads).

Maximum phase deviation between any two output ports = 13. 9 mm, at λ = 300 mm, or equivalently 16. 67 electrical degrees.

Output Port Phase Measurements

Port No.	Slotted Line Reading (mm) (Avg)
1	173. 3
2	159. 4
3	159. 4
4	160. 0

Output Port Isolation Device Reciprocity

Port Number	1	2	3	4	Input
Power Level	*	15.0	12.4	15.0	7.2
Referred to	15.5	*	5.9	12.3	7.0
Input Power	12.6	15.0	*	15.0	7.0
-db	15.0	12.0	15.0	*	6.7

---

*Indicates port into which power is fed.

TABLE IV-3; 8-WAY POWER DIVIDER - DESIGN MODEL. $f_o = 1.0$ GHz,

Maximum phase deviation between any two output ports = 3.7mm at λ - 300 mm, or equivalently 4.5 electrical degrees.

Input Port SWR 1.43

Output Port No.	Power Level -db (referred to input
1	9.4
2	9.4
3	9.3
4	9.4
5	9.3
6	9.6
7	9 4
8	9 4

Output Port Phase Measurement

Output Port No	Slotted Line Reading (mm) Avg.
1	96.0
2	96.4
3*	93.9
4	97.4
5	96.4
6	97 6
7	96 1
8	97.3

*After testing completed, cracking in bond of connector discovered.

TABLE IV-4. 16 WAY POWER [illegible]

[illegible]

equivalently [illegible]

Output Port Number	Power Level -db (referred to input)	Output Port Isolation (-db)	Slotted Line Reading (mm) Averaged
1	13.2	22.3	98.1
2	13.2	24.1	99.4
3	13.2	15.8	99.3
4	13.2	13.3	99.8
5	13.2	18 1	98.5
6	13.2	19 9	98.8
7	13.2	16 7	99.1
8	13.3	17.8	99.0
9	13.2	Feed Port	97.3
10	13.3	17.6	98.7
11	13.3	16.9	98.6
12	13.2	25.3	99.9
13	13.2	18.6	98.6
14	13.2	13.3	99.5
15	13.2	15.8	98.1
16	13.2	24.2	98.7
Input	X	13.1	X

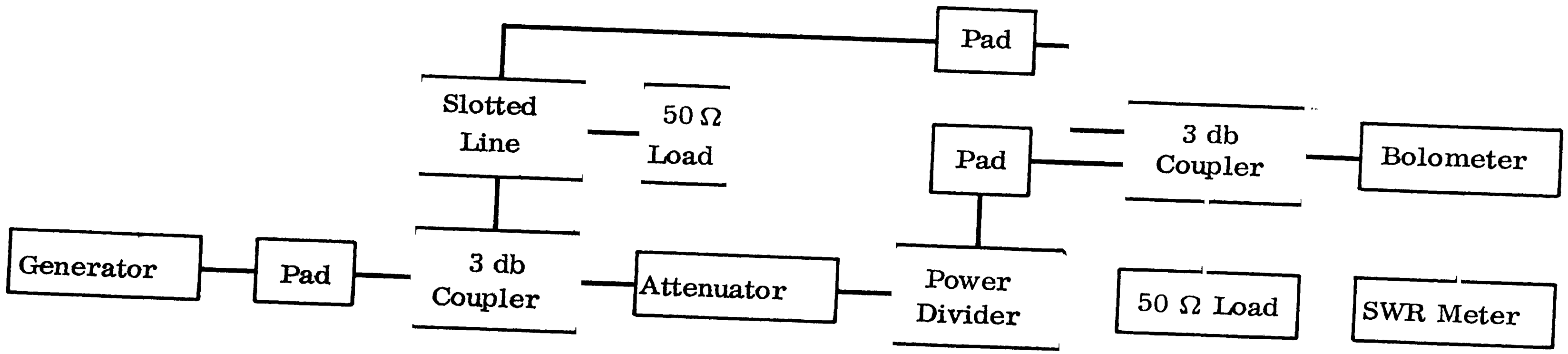

FIG. 4-16: PHASE MEASUREMENT BLOCK DIAGRAM

The design chosen for the feed network system (Section 4.2. 1) requires a total of five dividers; one four-way and four sixteen-way dividers. Based upon the above experimental results, two of the radial-line dividers were next constructed, one four-way and one sixteen-way divider. These models were designed on the basis of the dimensions of the prototype model scaled to 1.25 GHz for reasons of economy of material and size. The dimensions of this scaled model were; outer diameter = 9" (1.45λ), inner disc radius = 3.781" (.61λ). These two dividers were then tested to check input impedance level, output power level, and phase uniformity. The results of these measurements (denoted as 16-way divider Number 2, and four-way divider) are summarized in Table IV-5 and **Fig. 4-17**.

In addition, the prototype model discussed above was modified by cutting it into a cylindrical form and wrapping the outer edges with aluminum tape. Aluminum tape was used on all models to provide a completely shielded device. The modified prototype model was then tested at 1.25 GHz and found to perform adequately. This saved the construction time and the materials required for one of the four 16-way dividers required.

Finally, the remaining two 16-way dividers, denoted as Numbers 3 and 4, were constructed. Again measurements were made to check the critical parameters of the divider and these are also summarized in Table IV-5 and **Fig. 4-17**. The discrepancies in input impedances of the dividers are probably attributable to the inherent variations in construction procedures. This seems to be particularly evident since dividers No. 3 and 4 were built at the same time, while divider 2 and the prototype model, divider 1, were each constructed separately and the values of input impedance for dividers 3 and 4 are almost identical.

4.4 Array Design and Construction

The element radiators chosen for the volume array were slot-fed dipoles with dipole length $2\ell \doteq 3\lambda/8$ (see **Fig. 4-18**). These elements are standard, commercially available antennas and were found to be obtainable at low cost. The indicated frequency range of operation for these dipoles is 1.2 to 2.0 GHz,

#4(16 Port) #3 (16 Port)

#1 (16 Port)

4 Port

#2 (16 Port)

FIG: 4-17: SMITH CHART SUMMARY - INPUT IMPEDANCES OF STRIP RADIAL TRANSMISSION-LINE POWER DIVIDERS.

TABLE IV 5 SUMMARY OF L-BAND PROPERTIES OF RADIAL LINE DIVIDERS
Frequency of operation - 1.25 GHz.

Average Outpu Power level referred to input power level (-db); 16 way divider. 13.0db
4 way divider: -7.0 db.

Divider Type	No. of Divider	Input SWR	Max. Power Deviation db*	Max. Phase Deviation* (elec. deg.)
16 way	1	1.68	.4	7.34
16 way	2	2.5	.3	5.4
16 way	3	2.4	.1	3.15
16 way	4	2.4	.2	3.6
4 way	X	1.64	.2	2.7

*Maximum deviation which occurred between any two output ports

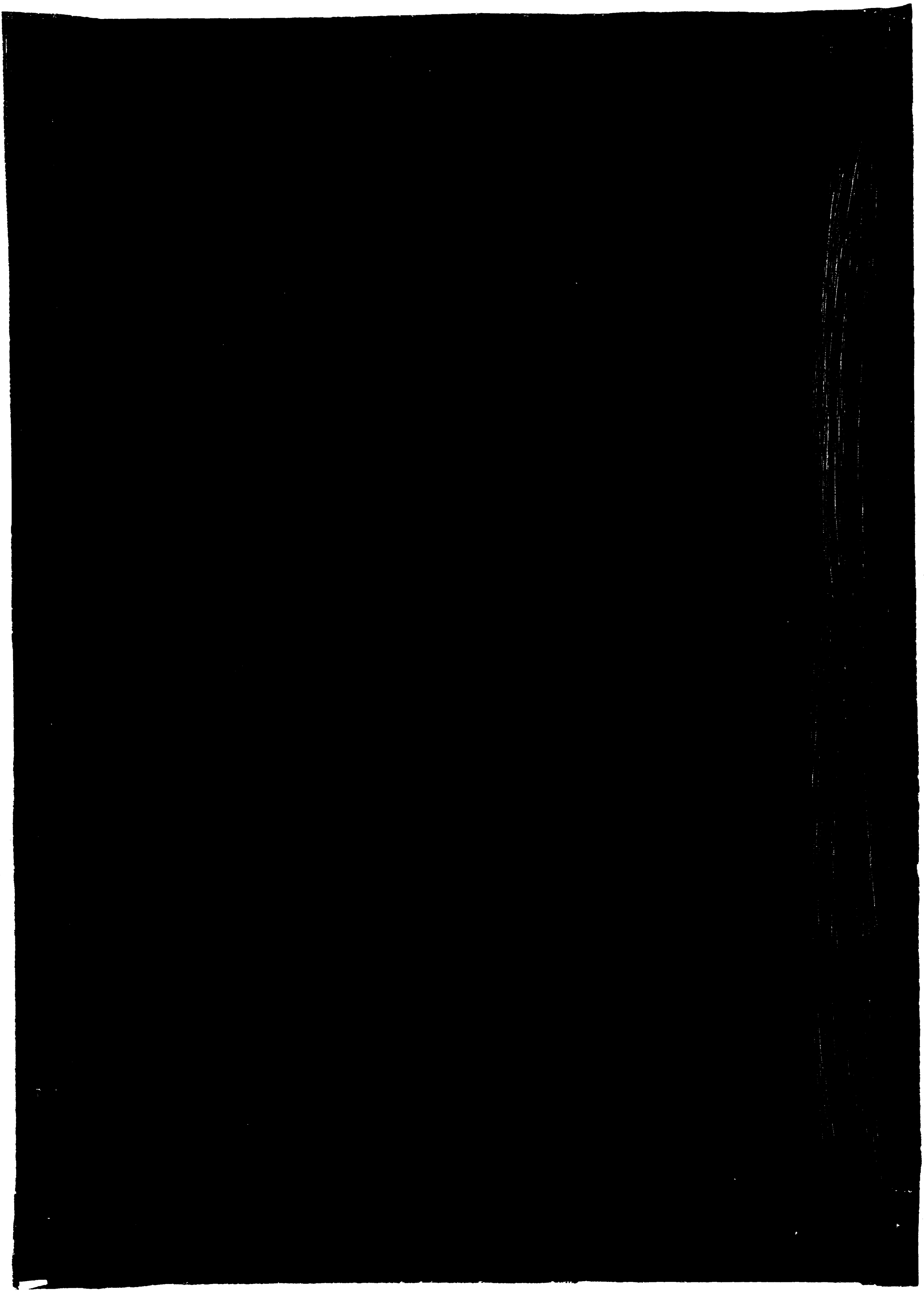

which is within the range decided upon for the array model (Section 4. 1).

Measurements of the input impedances and radiation patterns of four sample dipole elements resulted in the choice of 1. 25 GHz as the specific operating frequency for the array model. The dipole radiation patterns were all acceptable over their indicated band of operation, but the input impedance was most desirable from both the standpoint of minimum mismatch, and element to element impedance uniformity, at 1. 25 GHz. The impedance variation with frequency for the four sample elements is indicated in **Fig. 4-19**.

The geometric arrangement of the element radiators in the volume array follows a standard practice of arrays of lower dimension, namely a rectangular configuration, but in this case rectangular in all three dimensions. The spacings between elements in the three coordinate directions are not necessarily alike, but are each determined as discussed in Chapter III.

With the spatial geometric arrangement of the element radiators specified and the interelement spacing determined from the theoretical calculations, the topic of experimental array design really relates to the details of the supporting structure for the element radiators, i. e., the dipoles, and the details of the arrangement of the feed-lines for the dipoles.

In order to develop, test, and perhaps modify the various details of the construction design of the volume array support structure, a sequence of developments was undertaken. The first stage of this procedure involved the construction of three basic types of linear arrays, each consisting of four elements. Each of these array types, i. e., the linear end-fire, the broadside with parallel elements, and the broadside with collinear elements, can be viewed as sub-array components of the complete volume array. Of these three linear array types, the end-fire array was designed first. This choice was made based upon the expectation that attaining the progressive element phasing required for maximum radiation along the axis of the array would pose one of the more difficult problems to be encountered.

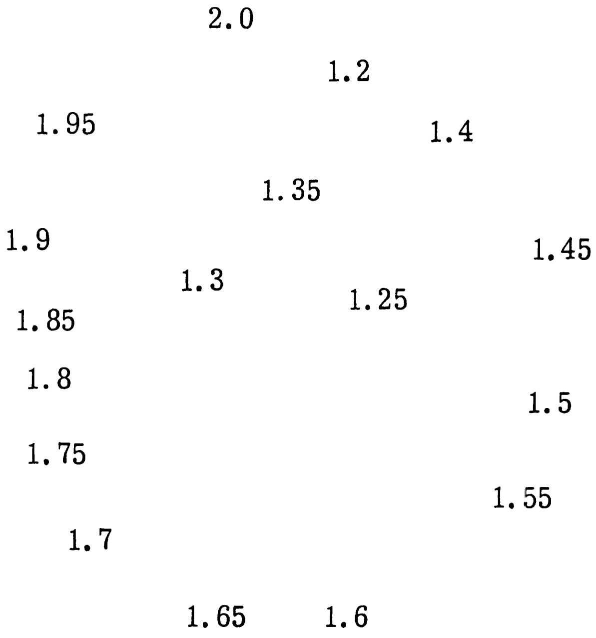

FIG: 4-19: INPUT IMPEDANCES OF 4 SAMPLE DIPOLE ELEMENTS vs FREQUENCY FROM 1.2 TO 2.0 GHZ (.05 GHZ STEPS)

The means of support for the dipole elements which was devised is shown in Fig. 4-20. The overall length of the array supports is approximately 4 feet. The interelement spacings of this and all subsequent arrays are given in tabular form in the following chapter (Table 5-2). The two rectangular cylinders in which the dipole arms are imbedded are made of expandable bead foam, sold under various brand names (Dilite, Pelaspan, etc) by several companies. The relative dielectric constant of this material is about 1.03, and so provides a close match to the free space environment of the antenna. However, one test was made to be certain that the effects of this foam are negligible, in particular with regard to distortions of the phase front of a wave propagating through a length of material, as is the case for the end-fire array. Two end-fire arrays were constructed, identical except for one feature. In one case the supporting foam was countersunk to accommodate the dipole balun structure, and to allow the two supporting cylinders to be butted together. In the other case, a gap equal to the diameter of the coaxial balun structure of the dipole was allowed to exist between the two supporting cylinders. These two arrays are shown in Fig. 4-21. Based on the measurements performed, the presence of this gap caused no significant change in the array pattern level or shape, as can be seen from the radiation patterns of Fig. 4-22.

The negligible measurable effects resulting from this change in the arrangement of the foam supporting structure supports an intuitive viewpoint that the very small difference between the dielectric constant of the foam and that of free space should allow relatively free use of foam material for this type of support structure without significantly affecting array behavior. However, in order to minimize the possibility of cumulative effects which might be present, however small, the thickness of all foam support members was held to a minimum. In addition, an attempt was made to achieve symmetrical placement of the foam with respect to the geometric center of the array.

FIG. 4-20: DETAILED VIEW OF DIPOLE SUPPORT IN STYROFOAM CYLINDERS:

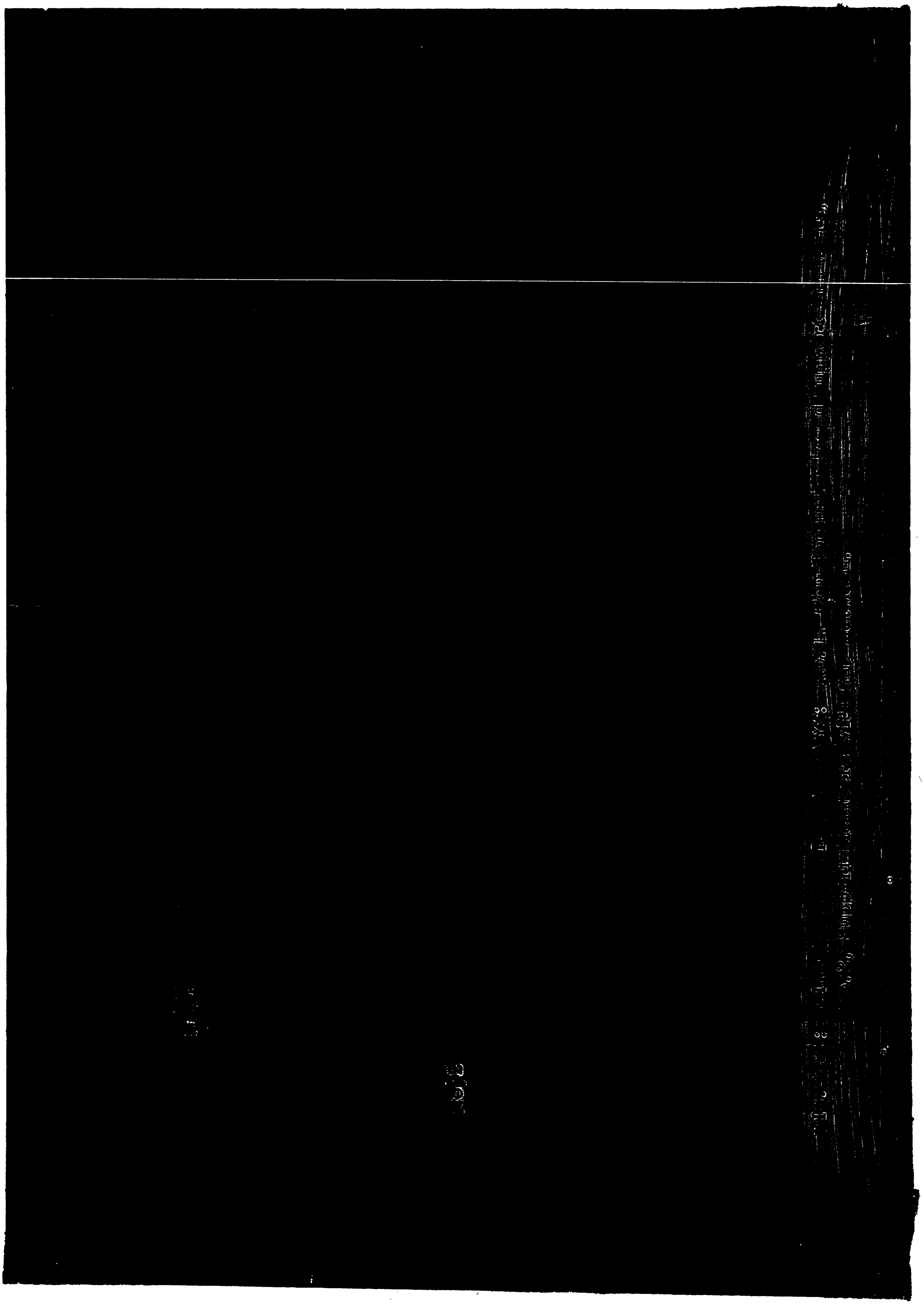

Open Foam Support

Closed Foam Support

FIG. 4-22: RADIATION PATTERNS (H PLANE) OF FOUR ELEMENT ENDFIRE ARRAY WITH VARIATION IN FOAM SUPPORT MEMBERS AS INDICATED.

After completing measurements on the end-fire array, the remaining two linear array types were similarly constructed and tested. The details of the construction of these arrays can be noted in Figs. 4-23 and 4-24. The support members of the linear broadside array with parallel elements were also about 4 feet in length. The linear broadside array of collinear elements required the use of wooden support members. Ordinary 1/2 inch quarter-round strips of white pine were used for this purpose,and in all subsequent cases these strips were used where support members other than foam cylinders were needed. Based upon all measurements performed during the overall experimental investigation, the manner in which such support members were used seems to have little effect on array properties at the model frequency.

One additional construction feature of the arrays should be noted for completeness. All fastening of the various portions of the array structure, and of the total structure itself to supports needed while performing pattern measurements, utilized a special purpose double-strand nylon filament tape. Use of this tape is fairly standard practice for antenna model mock-ups, and its influence on model properties has been determined to be negligible.

After all linear array measurements were completed, a sixteen-element (4x4) planar array, or to use volume array terminology ,, a single deck lattice array, was constructed and tested. The supporting structure for this array combined those features which were developed for the linear broadside arrays of parallel, and of collinear elements. These features can be noted in the photograph shown as **Fig.** 4-25. The outer dimensions of the supporting structure of the array are about **48"x30"** .

Following the completion of measurements on this single deck lattice array, the two, three and four deck lattice arrays were successively constructed. Each of these arrays made use of foam support blocks (4" thick, 4' long and of variable width depending on the number of decks) placed along two opposing sides of the array to hold the successive decks in position, and at fixed inter-deck spacing. The wooden supports of each single deck provided the means for

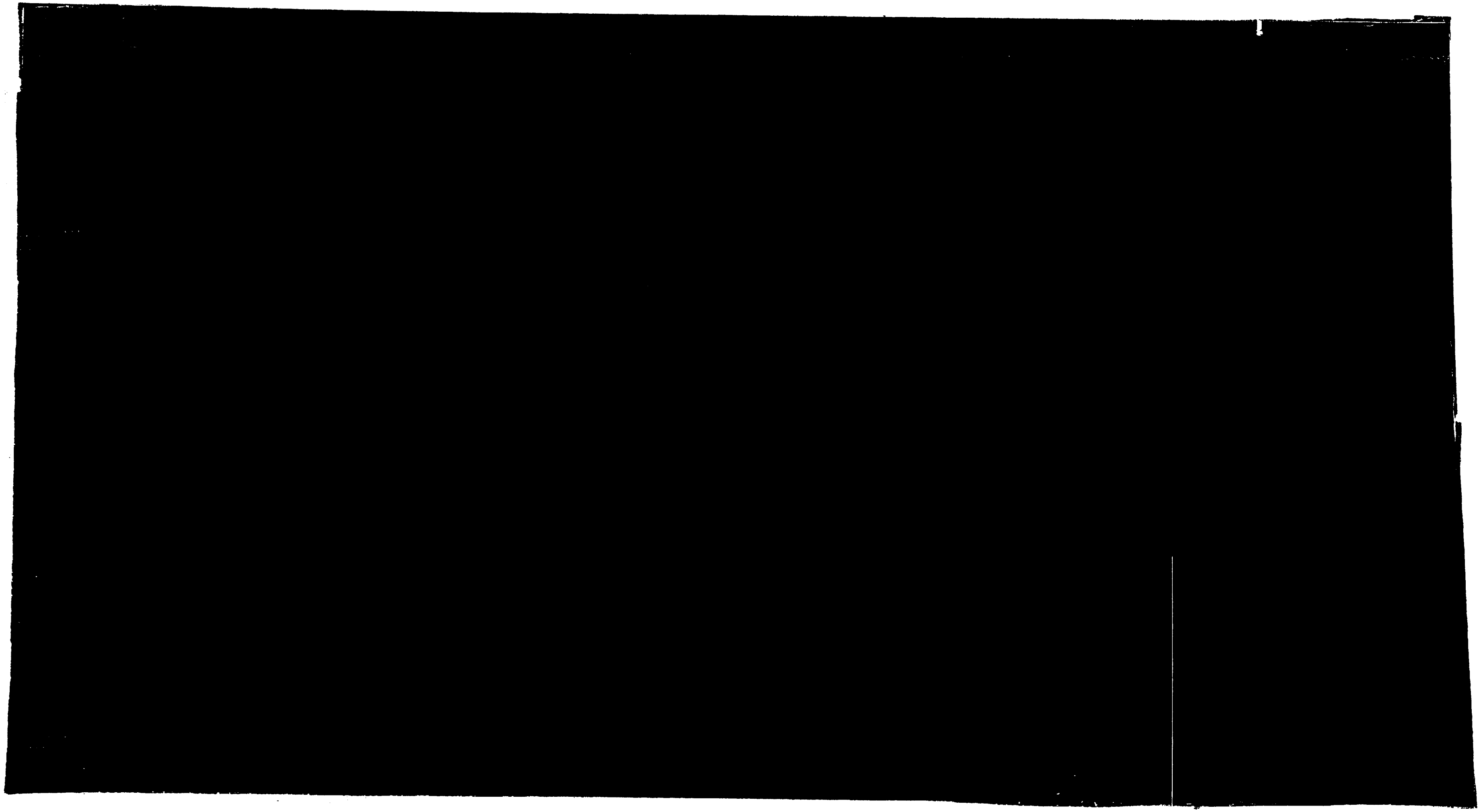

FIG. 4-23: LINEAR BROADSIDE ARRAY OF FOUR PARALLEL ELEMENTS

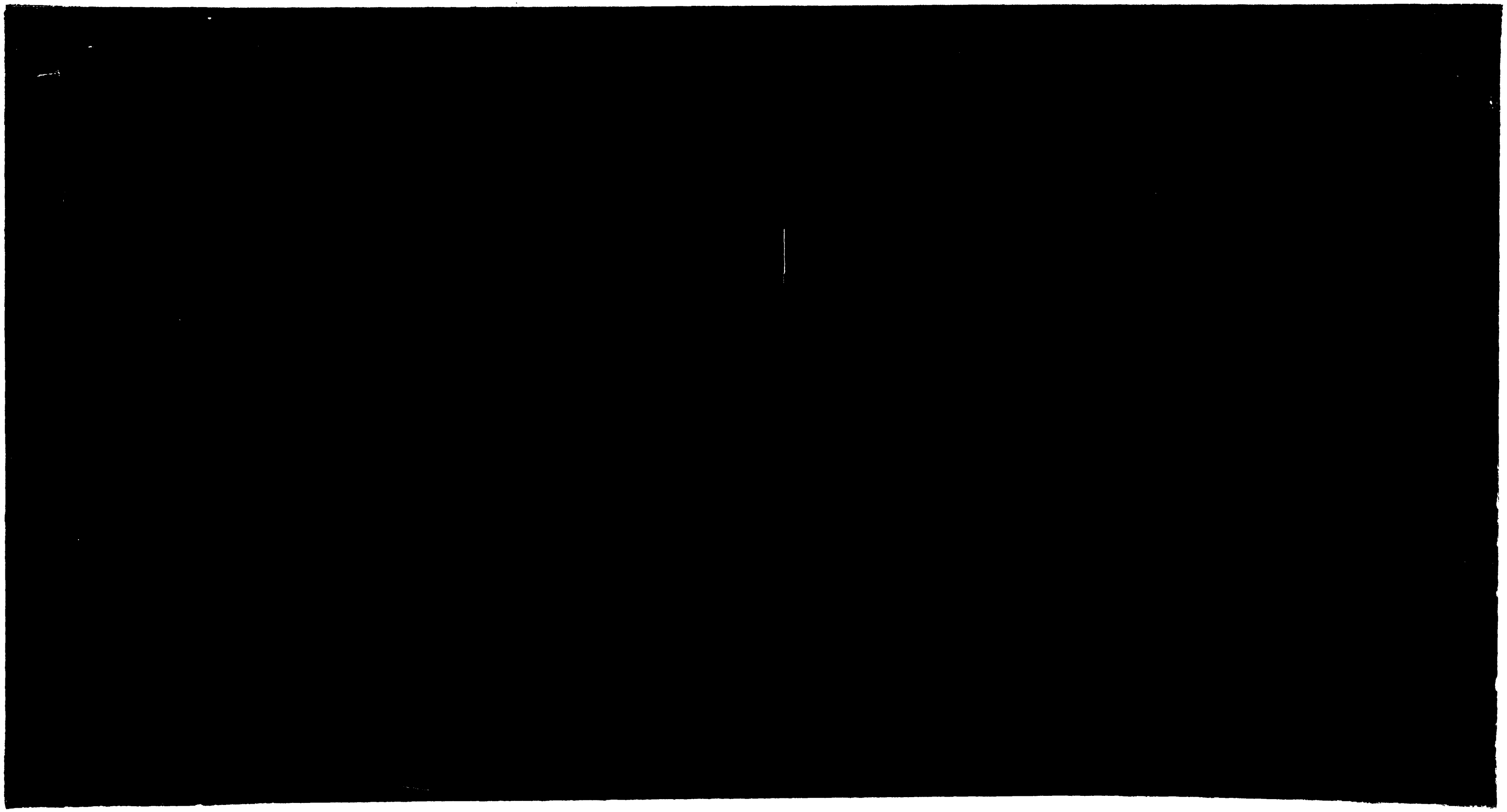

FIG. 4-24: LINEAR BROADSIDE ARRAY OF FOUR COLLINEAR ELEMENTS.

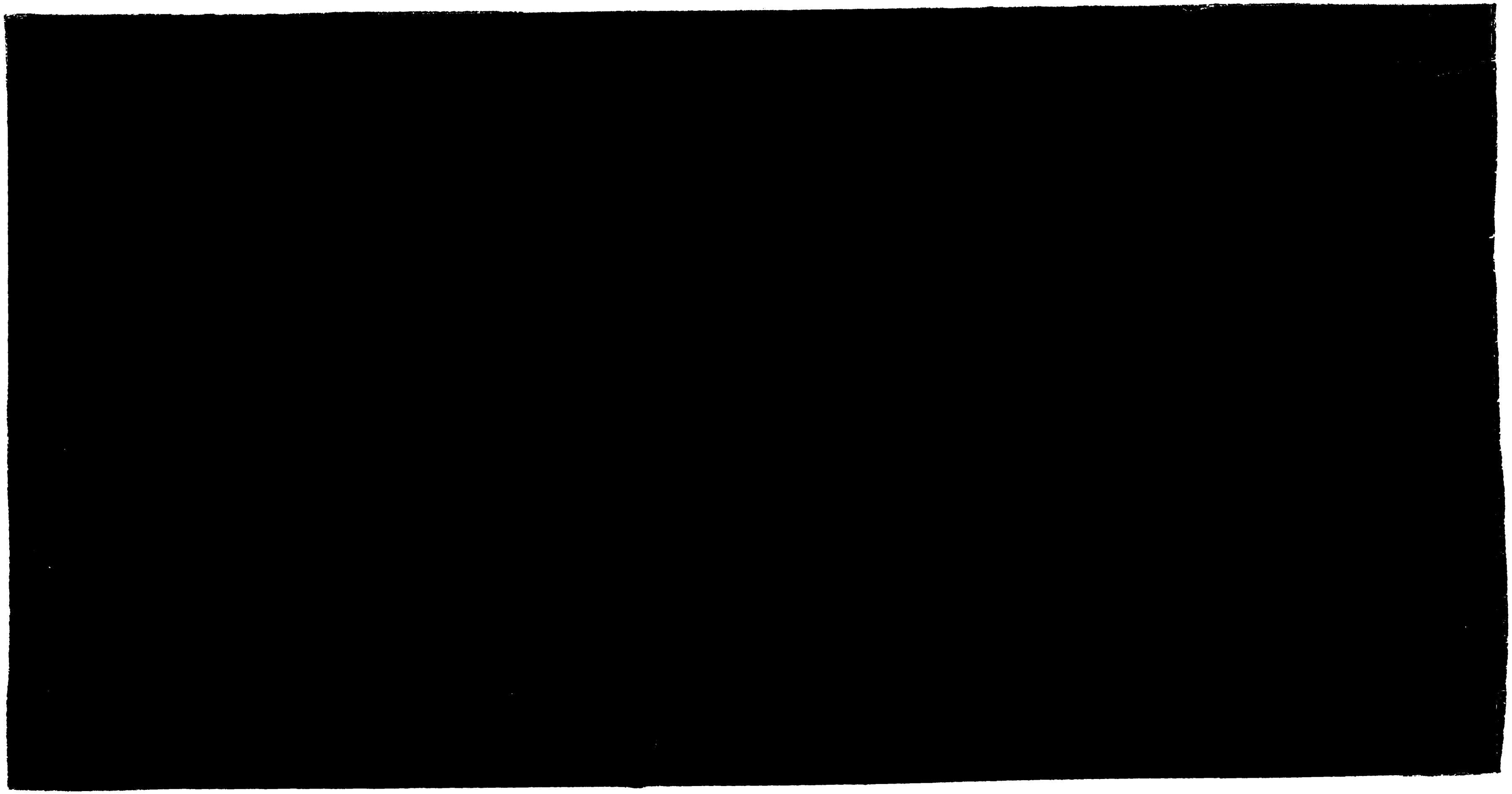

FIG. 4-25: 16-ELEMENT PLANAR ARRAY (SINGLE DECK LATTICE)

attaching the individual decks to these support blocks, and also for maintaining the specific deck spacings required. In addition small spacing blocks were used between decks in the two deck array, and between linear sub-arrays of parallel elements in the three and four deck arrays. These small blocks were necessary in order to obtain sufficient rigidity for the overall array structures, and thus assure that the various interelement spacings would remain relatively constant during test procedures. These various features can be noted in the photographs of these three array types (Figs. 4-26, 4-27, 4-28 and 4-29). The overall dimensions of the final array model, i.e. a 4 x 4 x 4 lattice array, including all supporting foam is about 4' x 4' x 1'.

In each of the arrays mentioned above, the element feed-lines were arranged normal (perpendicular) to the polarization axis of the dipoles in the array. This orthogonal relationsip was maintained within the region defined by the array support structure at all times. Figure 4-28 illustrates the arrangement in the case of the three deck lattice array.

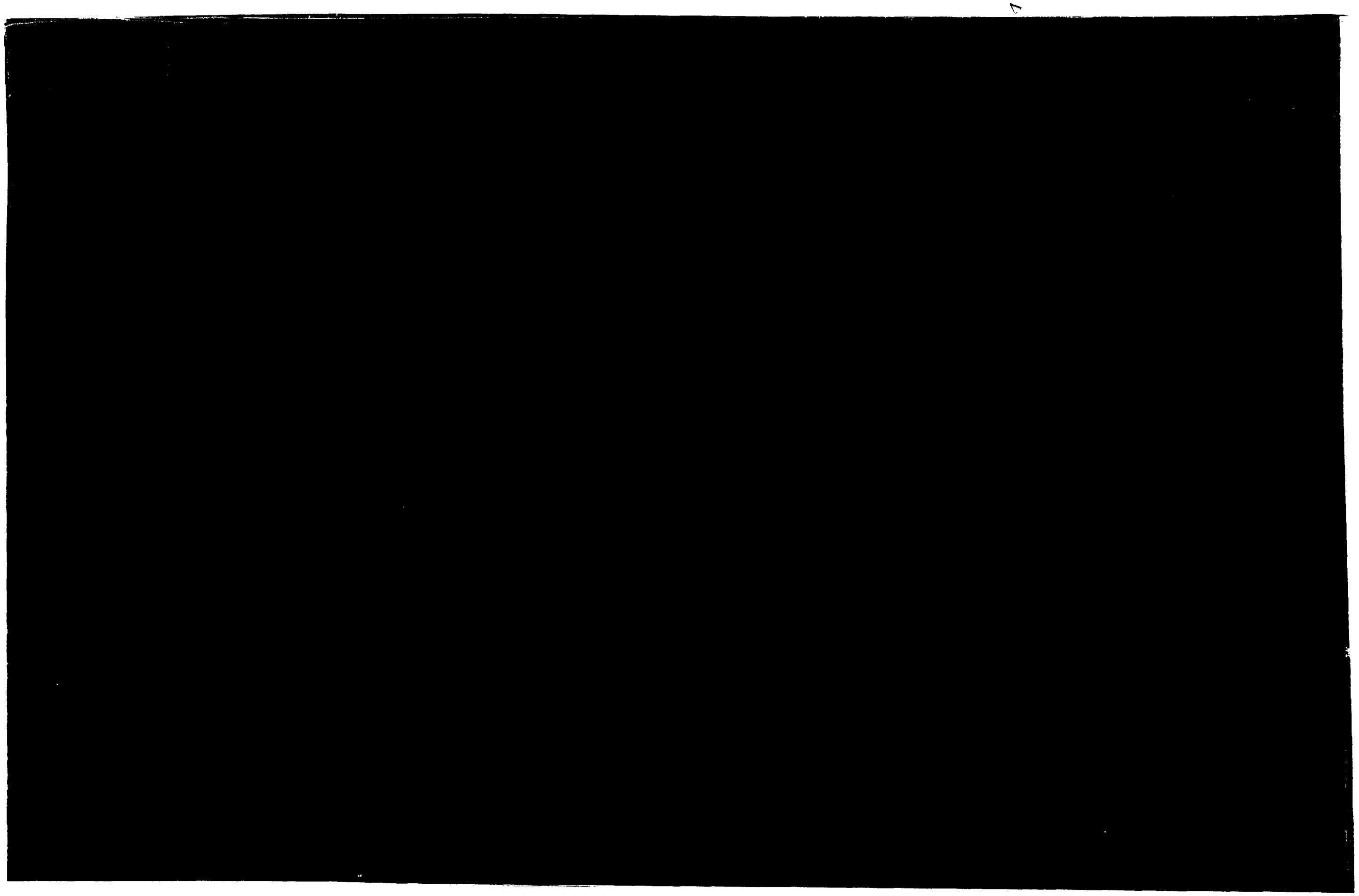

FIG. 4-26: END-ON VIEW OF TWO DECK LATTICE ARRAY (4 x 4 x 2) ATTACHED TO TEST PEDESTAL (IN LOWERED POSITION).

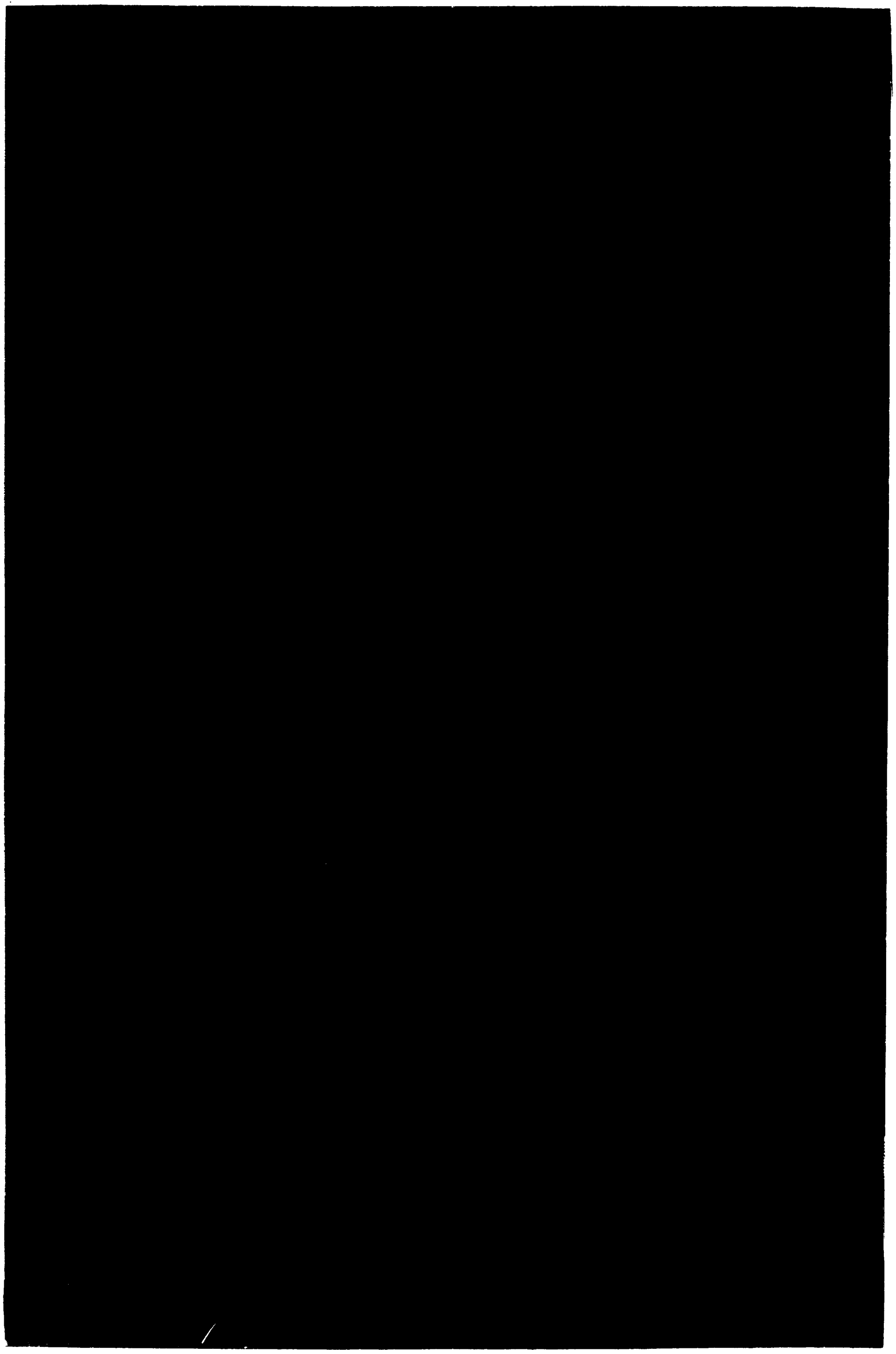

FIG. 4-27: TWO DECK LATTICE ARRAY (4 x 4 x 2)

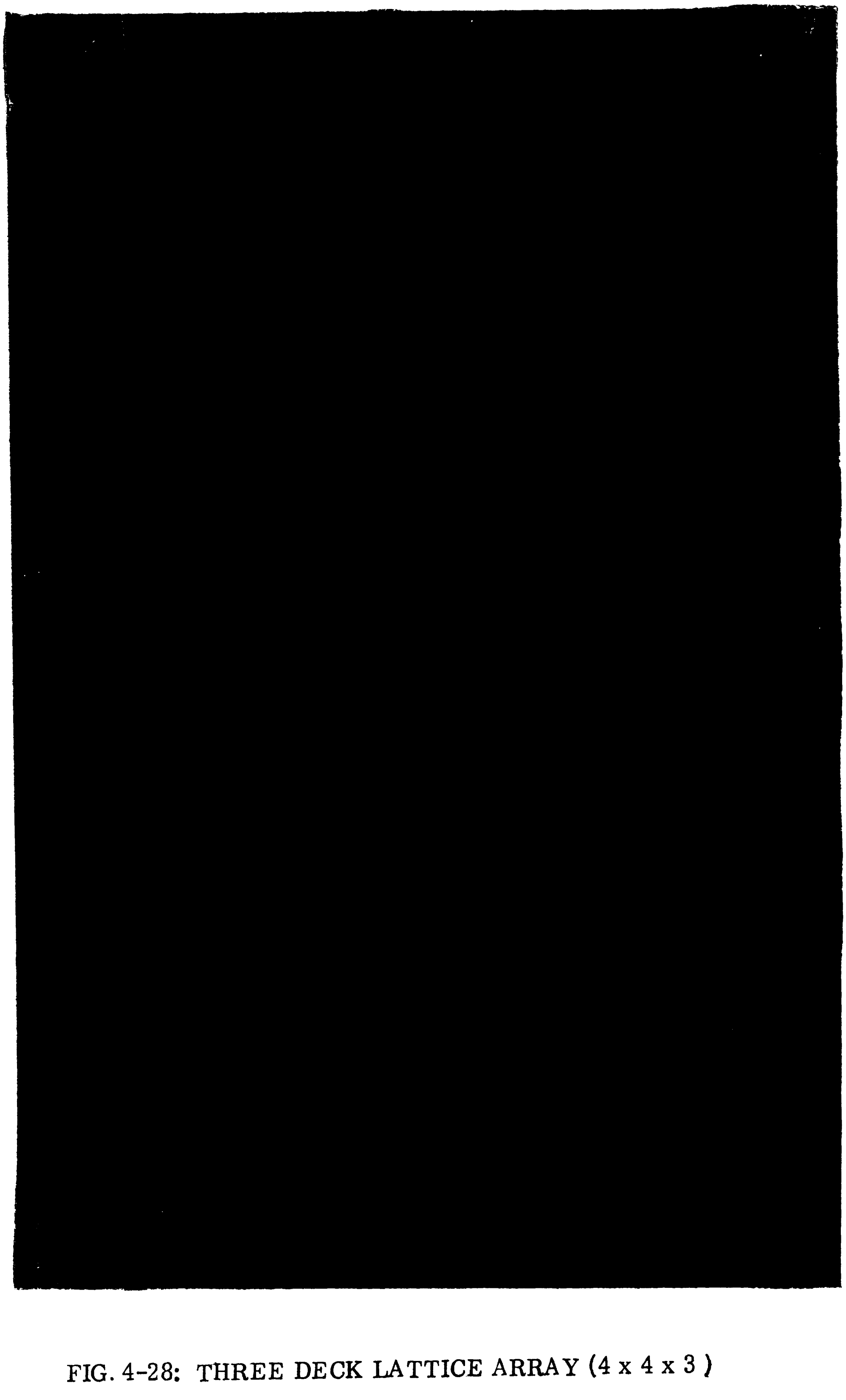

FIG. 4-28: THREE DECK LATTICE ARRAY (4 x 4 x 3)

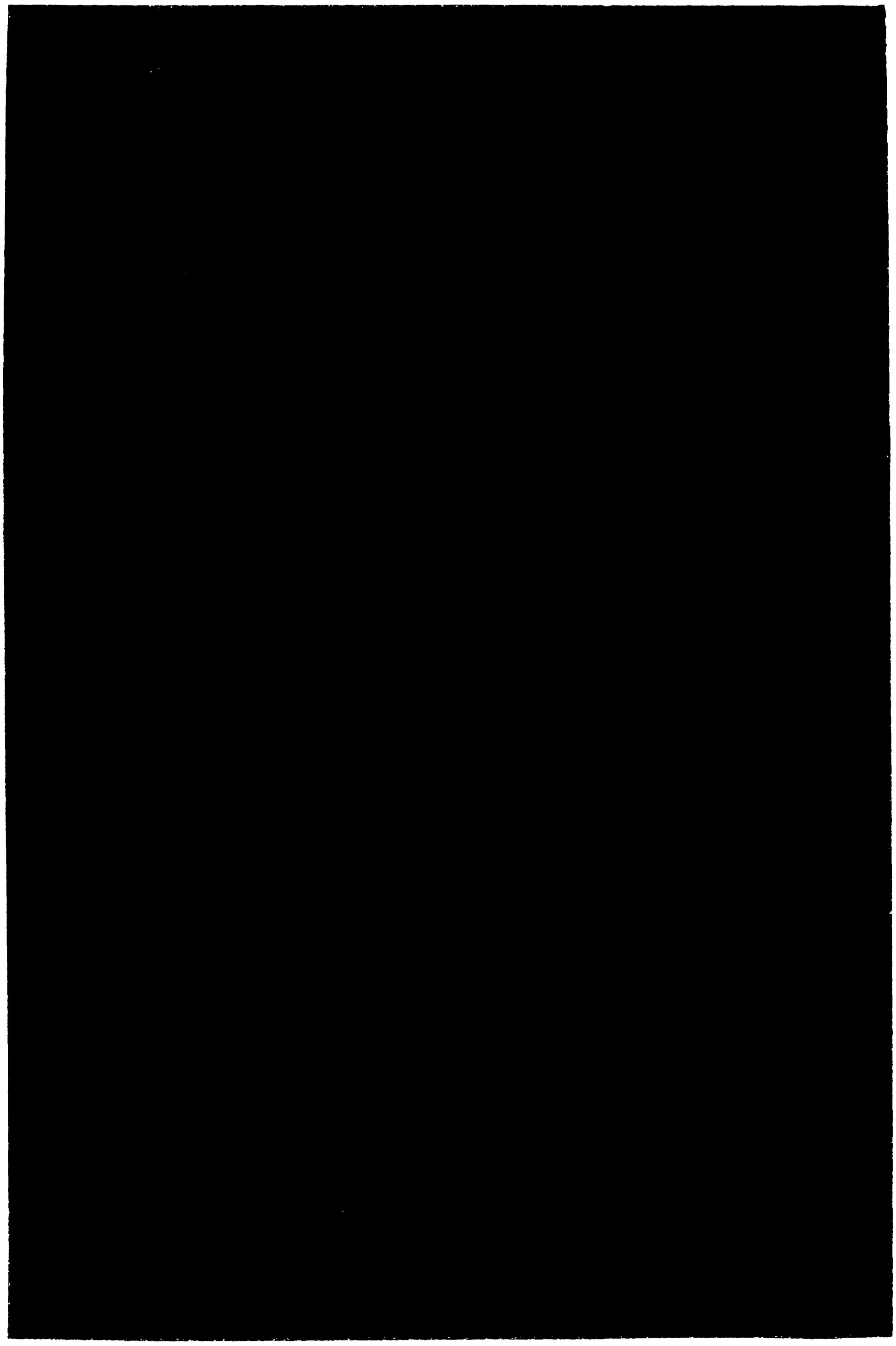

FIG. 4-29: FOUR DECK LATTICE ARRAY (4 x 4 x 4)

V

RESULTS OF EXPERIMENTAL MEASUREMENTS

5.1 General Discussion and Physical Realizability Criteria.

The significant array parameters for demonstrating the physical realizability of the volume array principle are taken to be the array radiation pattern, and the array-system gain. which is related to the array directivity by the efficiency factor η, i.e., $G = \eta D$.

In the experimental model considered, no attempt was made to optimize the system gain with respect to either transmission losses resulting from impedance mismatches, or network resistive and dielectric losses (see Chapter IV, Sec. 4.1 and 4.2). When possible, transmission losses due to mismatch effects were, however, experimentally verified and recorded. The measurements of the array radiation patterns were restricted to the E and H plane cuts of the full three-dimensional pattern. This restriction resulted largely from practical considerations. In particular the range facilities were not easily adaptable to the measurement of other pattern cuts.

From the theoretical standpoint, applying the pattern multiplication principle, the E and H plane cuts are sufficient to determine the characteristics of the entire radiation pattern of each type of array tested. In the ideal case, this fact follows from the various rotational symmetrics of the arrays, e.g. the rotational symmetrics of the three component linear sub-array patterns which produce the lattice array radiation pattern.

In practice, the three-dimensional radiation pattern can be expected to deviate somewhat from the theoretical pattern. These deviations result from mutual coupling effects, and from wavefront distortions caused by array element-radiatior support structures, feed lines and other feed-network components, and from the general surrounding environment of the array. In addition, various tolerance errors in element positioning and excitation also contribute to distortions of the ideal pattern. Such distortions may be evident in the E and/or H plane pattern cuts, and/or the rotational symmetrics of these patterns. The significance of such distortions may not be very great, however, if their magnitudes are small.

Since pattern measurements were restricted to E and H plane cuts, an attempt was made to obtain an approximation of total pattern distortion, particularly any strong secondary lobe structure. A measure of such distortion was based on the results of a comparison of theoretical and experimental E and H plane patterns, and the experimental system gain and theoretical maximum nominal directivity of the array. The maximum nominal directivity, defined as the ratio of the maximum value of radiated power to the integral of the complete normalized power pattern, gives a measure of the entire three dimensional radiation pattern. Some discrepancy between experimental array-system gain and optimum directivity can be expected due to various losses in the feed-network, and to the fundamental difficulties inherent in making absolute gain determinations. However, if the gain and maximum nominal directivity have similar values, and if the experimental and theoretical E and H plane patterns agree closely, then agreement between experimental and theoretical three-dimensional radiation patterns is strongly implied.

Based on this argument, for each array type tested, the measured value of array-system gain is compared with the theoretical optimum directivity, and the measured E and H plane patterns compared with the corresponding theoretical patterns. When such comparisons shown significant experimental-theoretical agreement, within the limits of experimental accuracies and known measurement limitations, then the physical realizability of the particular array-type will be considered established.

These experimental-theoretical gain and pattern comparisons also indicate the level of agreement of experimental directive properties of each array type with the corresponding theoretical maximum nominal directivity.

5.2 Coupling Effects

The degradation of array performance by mutual coupling between radiating elements in an array has been extensively studied in recent years, both theoretically and experimentally. The general qualitative effects of such coupling are well known, e.g., distortions of ideal array excitation resulting from changes in the driving point impedances of the radiating elements, and possible distortions of the radiating element current distributions. The particular quantitative effects on any given array parameter will vary depending on the details of the particular array configuration, the array element-radiator considered, and the construction details of the array and array feed-network.

A general indication of the magnitude of such coupling effects in the arrays tested here was obtained by observing the radiation pattern of each array type under a special excitation constraint. This constraint corresponds to the case of a transmitting array with only one element excited, and all others passively terminated in their normal load impedance. In this study, for those arrays having a reasonably small number of elements, patterns were taken under this constraint for all element radiators. For the larger arrays, such patterns were taken for certain element radiators only. These latter element samplings were chosen in such a manner so as to give some information on the symmetry of the array environment. All element patterns measured under this constraint will be termed element pattern factors, after Allen (1964). The degree to which these patterns deviate from the typical pattern of an isolated element radiator gives a qualitative measure of the strength of mutual coupling effects in the array, i.e., how strongly the elements of the array interact.

The element pattern factor results from the sum of the far field terms of all array elements. However, as already mentioned, only one element is actually driven in this particular case. The remaining array elements are indirectly excited by the directly driven element through mutual coupling effects. While this description represents the actual physical behavior related to the element pattern factor, a hypothetical situation can be envisioned which yields this same pattern for an array element. Consider an array of element radiators with no coupling between elements. If the element radiators possess current distributions which create element patterns similar to the various measured element pattern factors, then this hypothetical array has a radiation pattern and directivity indistinguishable from those of the actual array. This hypothetical case allows some significant comments to be made on the sensitivity of array parameters to element radiator patterns,and/ or current distributions,and distortions thereof. These comments are based on the measured element pattern factors and will be made in Section 5.4.

Another coupling effect which can affect an array is coupling between the element-radiators and the array feed-lines (including the balun structures of the element-radiators). Such coupling is associated with currents on the outer surfaces of the coaxial lines. This effect tends to distort the radiation pattern of the array, and decrease the array efficiency. The orthogonal arrangement of the feed-lines with respect to the polarization axis of the array (Chapter IV, Section 4.4) tends to minimize such coupling, particularly when the array is horizontally polarized. However, when the array is vertically polarized, the orthogonality relationship does not hold as can be seen in the photograph of the four deck vertically polarized lattice array shown in Fig. 5-1. A direct indication of the presence of this type of coupling is difficult to obtain. However, if such coupling effects are present and have significant values, they should cause observable departure

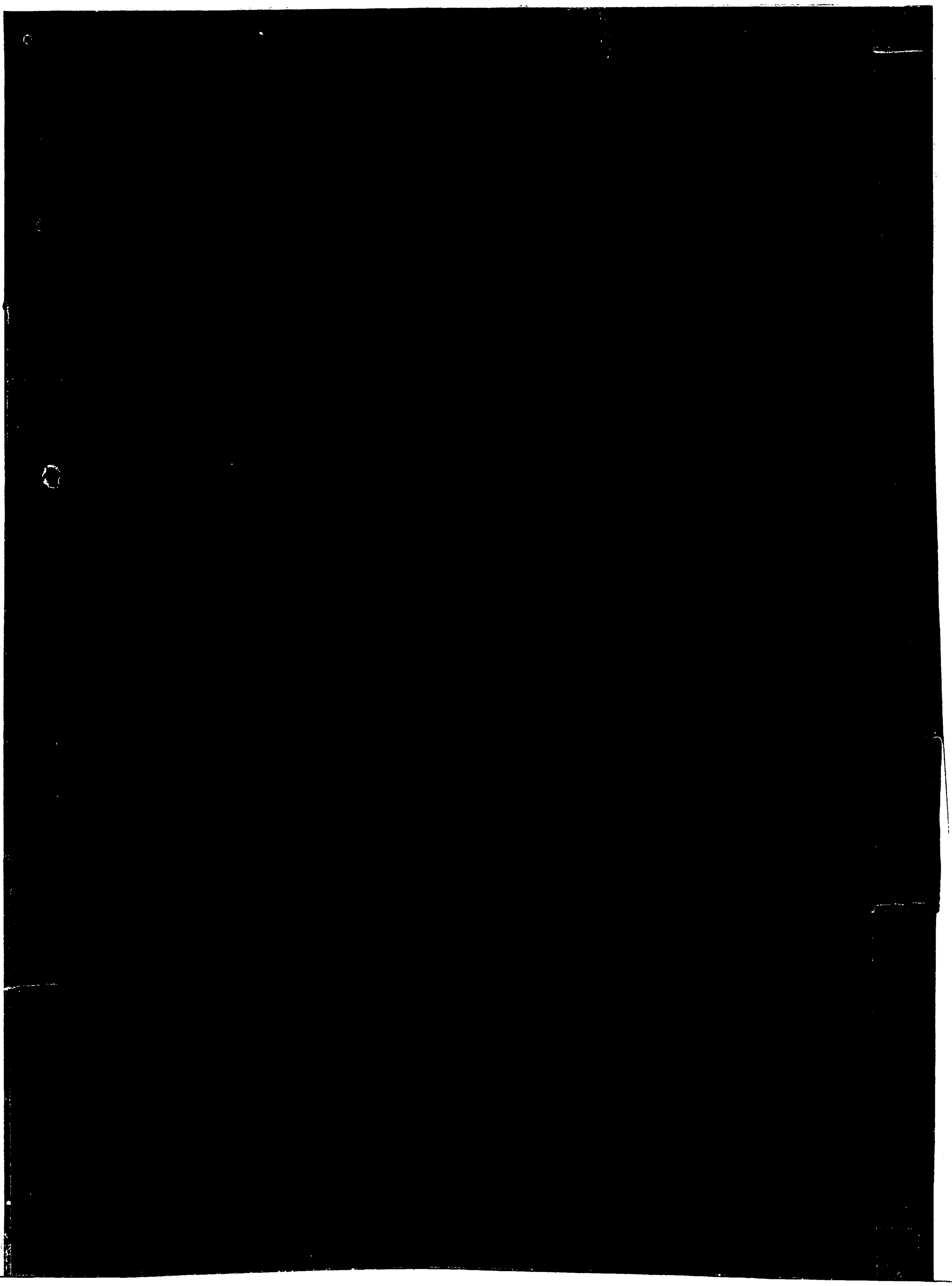

FIG. 5-1: VERTICALLY POLARIZED FOUR DECK (4x4x4) LATTICE ARRAY.

of the various experimental measurements from the corresponding theoretical predictions. If good agreement between theory and experiment is obtained, then apparently no such coupling exists to any significant degree.

One array characteristic in particular provides a good indication of this type of coupling. This parameter is the array cross polarization sensitivity, i.e., the sensitivity of a horizontally polarized array to a vertically polarized wave. In this case, the dipole elements of the array, being cross-polarized to the impinging fields, can be expected to extract very little power from the incoming wave. Consequently, any significant energy measured at the output of the array must result from currents excited on array feed-lines and other array feed-network components, which then couple into the dipole elements of the array. If the power level at the output of such a cross-polarized array is very low, then there is good indication that the array is insensitive to this type of coupling effect.

5.3 Results of Experimental Measurements

Based on the concepts outlined in Sections 5.1 and 5.2, measurements were made of the E and H plane cuts of the radiation pattern of each constructed array type using standard antenna measurement techniques. The output power level of the transmitter system (see Appendix C) was continuously monitored and recorded on each measured pattern. Prior to, and following each set of array measurements, the E and/ or H plane cuts of a dipole were recorded for gain calibration, again monitoring and recording the transmitter output power level.

The dipole used for gain calibration was identical to the dipole element-radiator used in the arrays, and conformed quite well to the theoretical properties of a $\frac{3}{8}\lambda$ dipole in the E plane pattern, i.e., nulls in excess of -30 db with respect to forward gain, and half power beamwidth of approximately 84°. However, as will be noted later there was evidence that the H plane pattern was more directive than theoretically predicted. Typical

E and H plane patterns for such a dipole are shown in Figure 5-2. These patterns illustrate the effect of the rotational ellipticity of the range test-pedestal (See Appendix C). The two polar patterns were typical of those taken for gain calibration on the outdoor range. The rectangular plot was made in an anechoic chamber on a test pedestal having no ellipticity, illustrating that the asymmetry of the E plane polar pattern from the outdoor range is due to the mount characteristics, rather than some anomalous dipole effect. By using a systematic setup procedure when making pattern and gain measurements, the effects of test pedestal ellipticity which tend to introduce errors into the gain calculations were minimized.

The experimental gain of each array was determined by the direct comparison method, subtracting the maximum values of the corresponding E (H) plane patterns of the array and the gain standard dipole after adjusting all patterns to common reference power level. These adjustments were necessary to compensate for transmitter power level drifts, fractional power monitoring (i.e., power divider effects), cable losses, and impedance mismatch losses. These factors should be kept in mind when comparing power levels between any patterns shown in this chapter.

The theoretical value to be compared with the experimental gain figure is the difference between the theoretical directivity of the appropriate array, and a $\frac{3}{8}\lambda$ dipole element. Since the theoretical directivities of a short (Hertzian) dipole and a half wave $\left(\frac{\lambda}{2}\right)$ dipole are 1.76 db and 2.15 db, the value 2.0 db was chosen for the $\frac{3}{8}\lambda$ dipole for numerical simplicity.

The arrays tested, in order of testing, were: four element linear end-fire array; four element linear broadside array with parallel elements; four element linear broadside array with collinear elements; 16 element (4 x 4) broadside planar array; 32 element (4 x 4 x 2) two deck lattice array; 48 element (4 x 4 x 3) three deck lattice array; 64 element (4 x 4 x 4) four deck lattice array. A summary of the results of the experimental measurements of gain and beamwidth for each type of

E Plane

H Plane

E Plane

FIG. 5-2: DIPOLE GAIN STANDARD PATTERNS: POLAR PLOTS-OUTDOOR RANGE; RECTANGULAR PLOT-ANEOCHOIC CHAMBER.

array, together with the corresponding theoretical values, is given in Table V-1. Table V-2 gives the optimum interelement spacing values used in the various array models. The discrepancies between experimental gain and theoretical optimum directivity $(G_{(v,h)} - \hat{D}_d)$ are directly indicated in the table for both horizontal and vertical polarizations, i.e., E and H plane radiation patterns. The acceptable level for experimental errors for the particular test range and equipment used is about ± .5 db. Since the array system feed-network incorporates several more components than the feed of the gain standard dipole, and since each of these components involves a power loss estimate, the experimental error limit should be increased by another ± .5 db, giving a total maximum expected experimental error level of ± 1.0 db.

The measured E and H plane array patterns, together with the corresponding theoretically predicted patterns are shown for the lattice arrays in Figures 5-3, 5-4, 5-6, 5-7, 5-9, 5-10, 5-12, and 5-13. Similar patterns are given for the linear arrays tested in Appendix D . The experimental array patterns of the four deck lattice array have indicated on them sample points from the corresponding theoretical patterns directly by black dots. The theoretical null positions are also indicated, by means of dotted lines. In general, agreement of theoretical and experimental E and H plane patterns for all arrays is quite good. The four deck lattice patterns were chosen for directly indicated comparison because this array represents the most complex configuration considered.

For each lattice the measurements of cross polarized radiation patterns, Figures 5-5, 5-8, 5-11, and 5-14, indicate that array sensitivity to such components in quite low, being -25 to -30 db below the main beam level in each case. The larger off-axis lobes of these patterns for a vertically polarized wave (horizontally polarized element radiators) result from the balun structures of the array elements (see Sec. 5.4).

For each array tested, E and H plane element pattern factors were measured as discussed above. For the lattice arrays with two or more decks, seven sample elements from each deck of an array were measured. Figure 5-15 illustrates the relative positions within an array of such

Array Type	Theoretical Optimum Directivity Referenced to a dipole D_d^o (db)	Experimental Gain Polarization				Beamwidth			
		Vert.		Horiz		E-Plane		H-Plane	
		G_v (db)	$G_v - \hat{D}_d$ (db)	G_H (db)	$G_H - \hat{D}_d$ (db)	Exp	Theor	Exp	Theor
4 Element Linear End-fire	6.8	6.3	-.5	6.1	-.7	61°	70°	69°	88°
4 Element Linear Broad-side Array of parallel Elements	8.7	9.6	+.9	7.7	-1.0	82.5°	— 84°	17°	16.5°
4 Element Linear Broad-side Array of collinear Elements	6.5	7.2	+.7	6.4	-.1	14°	14°	—	—
4 x 4 Planar Array	15.4	14.5	-.9	15.8	+.4	14.5°	14°	16°	16.5°
4 x 4 x 2 Lattice Array	18.4	16.4	-2.0	16.8	-1.6	15°	14.5°	15.5°	16.5•
4x4x3 Lattice Array	19.2	17.9	-1.3	17.6	-1.6	13.5°	13.25°	15°	15°
4x4x4 Lattice Array	19.8	16.8	-3.0	17.5	-2.3	12°	12°	14•	14.5°

TABLE V-1: SUMMARY OF EXPERIMENTAL VERSUS THEORETICAL GAINS AND BEAMWIDTHS FOR ALL ANTENNAS TESTED.

Array Size	OPTIMUM INTERELEMENT SPACING (IN WAVELENGTHS)		
	Parallel Elements "A"	Collinear Elements "C"	Endfire Elements "B"
4 x 4 x 1	.7875	.8875	—
4 x 4 x 2	.7875	.900	.2625
4 x 4 x 3	.8625	.975	.350
4 x 4 x 4	.8875	1.0875	.3875

TABLE V-2: ARRAY ELEMENT SPACING FOR MAXIMUM NOMINAL DIRECTIVITY.

Experimental

Theoretical

NUMBER OF ELEMENTS: 16

FIG. 5-3: PLANAR ARRAY RADIATION PATTERN E-PLANE CUT.

Experimental Theoretical

NUMBER OF ELEMENTS: 16

FIG. 5-4: PLANAR ARRAY RADIATION PATTERNS H-PLANE CUT.

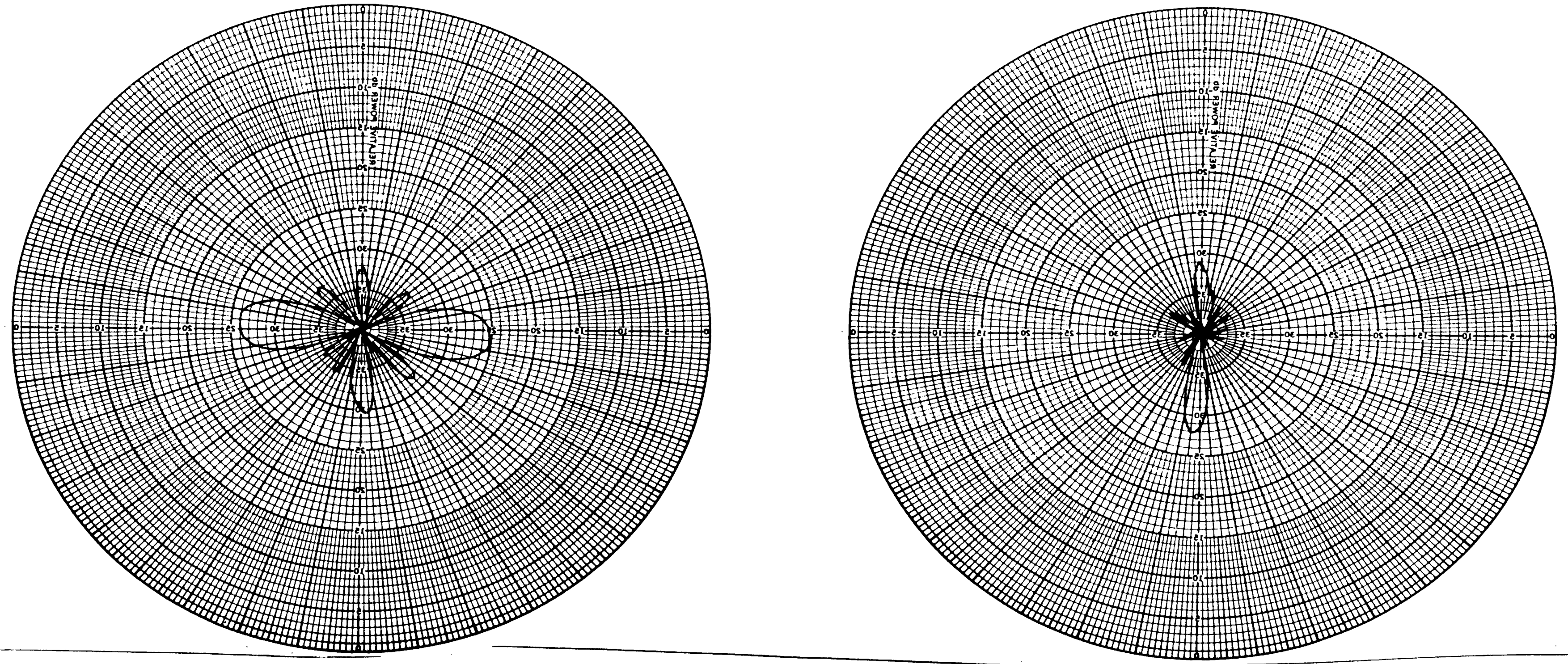

Horizontally Polarized Wave

Vertically Polarized Wave

FIG. 5-5: CROSS POLARIZED PATTERNS — PLANAR ARRAY.

Experimental

NUMBER OF ELEMENTS: 32

Theoretical

FIG. 5-6: 4x4x2 LATTICE ARRAY RADIATION PATTERN — E PLANE CUT.

Experimental **Theoretical**

NUMBER OF ELEMENTS: 32

FIG. 5-7: 4 x 4 x 2 LATTICE ARRAY RADIATION PATTERN - H-PLANE CUT.

Horizontally Polarized Wave

Vertically Polarized Wave

FIG. 5-8: CROSS POLARIZED PATTERNS — 4x4x2 LATTICE ARRAY.

Experimental Theoretical

NUMBER OF ELEMENTS: 48

FIG. 5-9: 4 x 4 x 3 LATTICE ARRAY RADIATION PATTERN - E-PLANE CUT.

Experimental Theoretical

NUMBER OF ELEMENTS: 48

FIG. 5-10: 4 x 4 x 3 LATTICE ARRAY RADIATION PATTERN - H-PLANE CUT.

Horizontally Polarized Wave

Vertically Polarized Wave.

FIG. 5-11: CROSS POLARIZED PATTERNS - 4 x 4 x 3 LATTICE ARRAY

MISSING
PAGE

MISSING
PAGE

Horizontally Polarized Wave

Vertically Polarized Wave

FIG. 5-14: CROSS POLARIZED PATTERNS - 4x4x4 LATTICE ARRAY.

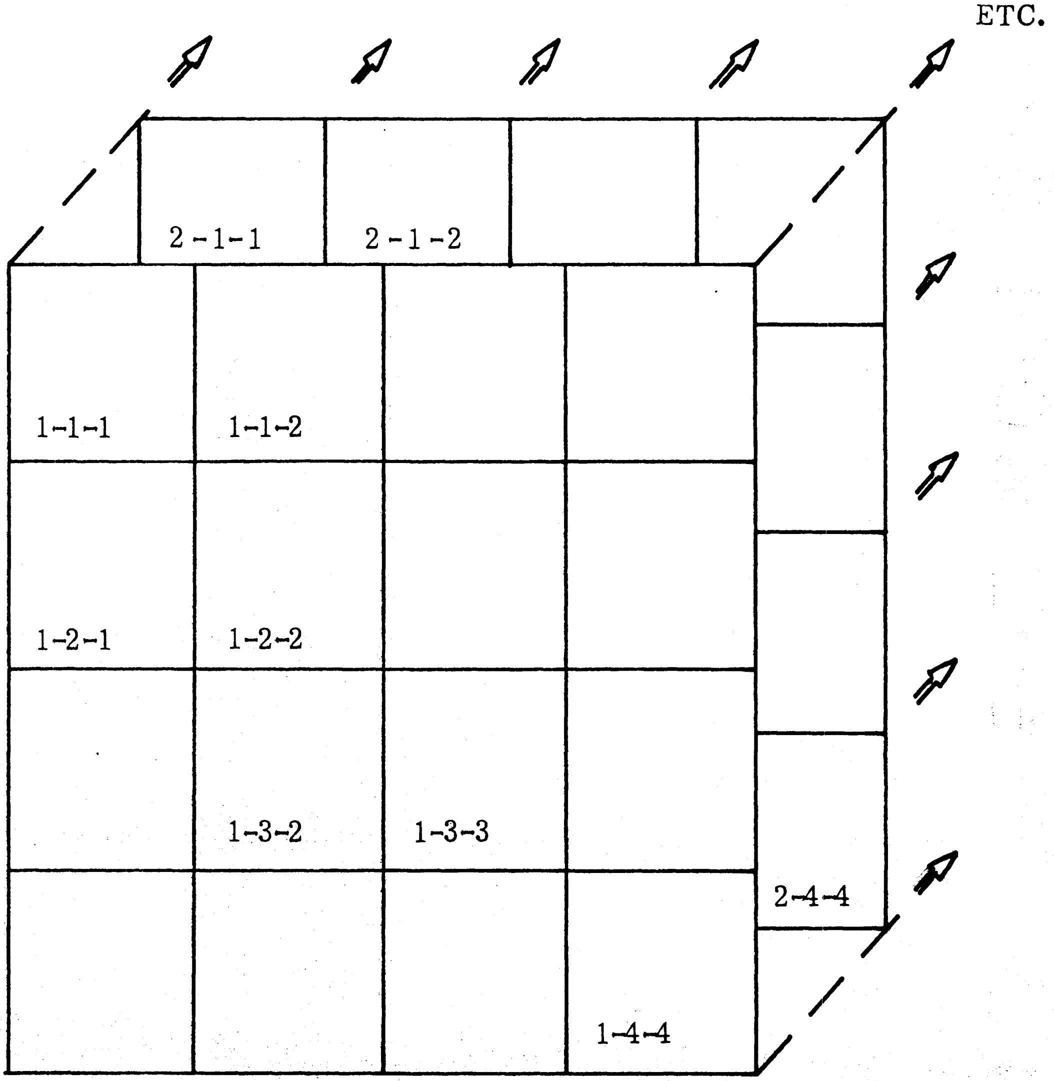

FIG. 5-15: POSITIONS OF DIPOLES WITHIN ARRAY STRUCTURE FOR WHICH ELEMENT PATTERN FACTORS WERE MEASURED.

sample elements. This figure illustrates the three dimensional matrix notation used to denote element radiator position within an array. The indices, in left to right order, denote deck number, row number, and column number. The row and column notation was defined for a horizontally polarized array.

The pattern factors for the sampled elements from the first and fourth decks of the four deck lattice array are shown as Figures 5-16, 5-17, 5-18, and 5-19. These two sets are representative of all the element pattern factors measured. Comparing these patterns pairwise, a check of array symmetry in all three coordinate directions can be made. Such a comparison indicates relatively good array symmetry. The element pattern factors for all other sample elements of the four deck lattice array, and those taken for all other array types, are placed in Appendix D for reference purposes. All element pattern factors measured show marked distortion from the corresponding ideal dipole patterns, indicating that considerable coupling effects are present. Sharp nulls in the H plane patterns correspond exactly to the position of coaxial feed cables arranged along one side of the array structure. In addition to distortions in the general shape of an element pattern factor, the pattern to pattern power levels in any fixed direction also show considerable variation. A summary of these variations is given in the tables of Fig. 5-20. These tables indicate the power level of each measured element pattern factor of an array in the direction of the main beam of the array, referenced to the first-numbered element of the array, i.e., element No. 1 for a linear array, element 1-1 for the planar array, and element 1-1-1 for each multiple deck lattice array These power level reference elements are indicated by the entry "0_R" in each set of tables. The location of each power level entry within a table corresponds to the location within an array of the element receiving such power.

The significance of the value given in these tables can be interpreted with the aid of Figures 5-21-A and 5-21-B. These figures give an equivalent circuit representation for a typical element radiator(s) within an

1-1 1-2

2-1 2-2

3-2 3-3

4-4

FIG. 5-16: ELEMENT PATTERN FACTORS - DECK NO. 1 OF 4 x 4 x 4 LATTICE ARRAY. E PLANE CUT.

1-1 1-2

2-1 2-2

3-2 3-3

4-4

FIG. 5-17: **ELEMENT PATTERN FACTORS - DECK NO. 4 of 4 x 4 x 4 LATTICE ARRAY. E PLANE CUT.**

1-1 1-2

2-1 2-2

3-2 3-3

4-4

FIG. 5-18: **ELEMENT PATTERN FACTORS - DECK NO.** 1 of **4 x 4 x 4 LATTICE ARRAY. H PLANE CUT.**

1-1

1-2

2-1

2-2

3-2

3-3

4-4

FIG. 5-19: ELEMENT PATTERN FACTORS - DECK NO. 4 of 4 x 4 x 4 LATTICE ARRAY. H PLANE CUT.

	LINEAR ARRAY TYPE											
Polarization	Broadside-Parallel Elements				Broadside-Collinear Elements				Endfire			
Horizontal	0_R	+.5	0	-.5	0_R	+.3	-.3	-.1	0_R	-1.9	-3.8	-6.2
Vertical	0_R	+1.45	+1.65	-.25	0_R	+.5	0	+.05	0_R	+.5	-1.3	-3.6

FIG. 5-20a: ELEMENT POWER LEVELS: LINEAR ARRAYS (All Values in db).

16 ELEMENT PLANAR ARRAY

	1	2	3	4
1.	0_R	1.3	1.2	.05
2.	2.25	1.85	1.9	2.2
3.	2.25	2.8	1.65	2.2
4.	1.6	1.3	2.1	1.3

Horizontal Polarization

	1	2	3	4
1.	0_R	1.0	1.0	-1.0
2.	2.0	2.1	1.0	1.3
3.	2.2	2.1	.8	1.0
4.	.5	1.2	.5	.1

Vertical Polarization

FIG.: 5-20b: SAMPLE ELEMENT POWER LEVELS: 16 ELEMENT PLANAR ARRAY (All Values in db).

	1	2	3	4
1.	0_R	1.6		
2.	1.2	.6		
3.		1.2	1.2	
4.				.6

Horizontal Polarization
Deck No. 1

	1	2	3	4
1.	-5.5	-4.2		
2.	-2.3	-.7		
3.		-.8	-1.7	
4.				-5.7

Horizontal Polarization
Deck No. 2

	1	2	3	4
1.	0_R	.4		
2.	1.3	.7		
3.		1.6	1.0	
4.				-.4

Vertical Polarization
Deck No. 1

	1	2	3	4
1.	-8.1	-5.9		
2.	-2.6	-2.6		
3.		-2.1	-4.1	
4.				-6.6

Vertical Polarization
Deck No. 2

FIG. 5-20c: SAMPLE ELEMENT POWER LEVELS: 32 ELEMENT-TWO DECK LATTICE ARRAY (4 x 4 x 2) (All Values in db).

	1	2	3	4
1.	0_R	.05		
2.	.6	.6		
3.		.6	-.3	
4.				-2.3

Horizontal Polarization
Deck No. 1

	1	2	3	4
1.	1.7	-.5		
2.	1.3	1.3		
3.		2.3	1.4	
4.				1.9

Horizontal Polarization
Deck No. 2

	1	2	3	4
1.	-4.7	-3.7		
2.	-2.1	-1.0		
3.		-3.0	-2.0	
4.				-5.5

Horizontal Polarization
Deck No. 3

	1	2	3	4
1.	0_R	1.3		
2.	.7	.1		
3.		1.3	.6	
4.				1.1

Vertical Polarization
Deck No. 1

	1	2	3	4
1.	-1.4	-.9		
2.	-.9	-.45		
3.		-.95	-1.95	
4.				1.95

Vertical Polarization
Deck No. 2

	1	2	3	4
1.	-5.5	-4.5		
2.	-4.0	-1.5		
3.		-2.55	-1.6	
4.				-4.9

Vertical Polarization
Deck No. 3

FIG. 5-20d: **SAMPLE ELEMENT POWER LEVELS: 48 ELEMENT - THREE DECK LATTICE ARRAY (4 x 4 x 3) (All Values in db).**

	1	2	3	4
1.	0_R	.05		
2.	1.1	.1		
3.		.35	.05	
4.				1.55

Horizontal Polarization
Deck No. 1

	1	2	3	4
1.	.8	.8		
2.	.8	.4		
3.		1.1	-1.1	
4.				-1.

Horizontal Polarization
Deck No. 2

	+	2	3	4
1.	-3.5	-2.5		
2.	-1.0	-.4		
3.			.6	
4.				-2.8

Horizontal Polarization
Deck No. 3

	1	2	3	4
1.	-5.3	-5.1		
2.	-5.8	-2.3		
3.		-3.2	-3.6	
4.				-6.55

Horizontal Polarization
Deck No. 4

FIG. 5-20e: SAMPLE ELEMENT POWER LEVELS: 64 ELEMENT - FOUR DECK LATTICE ARRAY (4 x 4 x 4) (All Values in db).

	1	2	3	4
1.	0 R	.1		
2.	1.55	1.55		
3.		1.05	1.1	
4.				-.4

Vertical Polarization
Deck No. 1

	1	2	3	4
1.	.6	.6		
2.	.1	-.9		
3.		-.4	-1.9	
4.				-1.2

Vertical Polarization
Deck No. 2

	1	2	3	4
1.	-3.7	-2.2		
2.	-1.3	.3		
3.		-.2	-1.2	
4.				-3.65

Vertical Polarization
Deck No. 3

	1	2	3	4
1.	-4.65	-4.7		
2.	-5.3	-3.4		
3.		-2.8	-6.75	
4.				-3.3

Vertical Polarization
Deck No. 4

FIG. 5-20f: SAMPLE ELEMENT POWER LEVELS: 64 ELEMENT - FOUR DECK LATTICE ARRAY (cont.) (All Values in db)

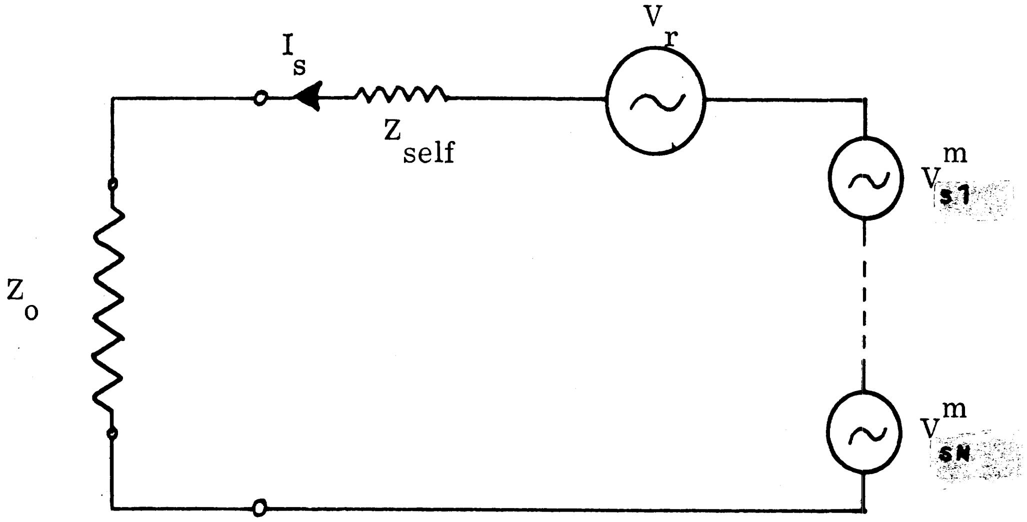

FIG. 5-21a: EQUIVALENT CIRCUIT FOR ELEMENT "s" IN AN "N" ELEMENT RECEIVING ARRAY.

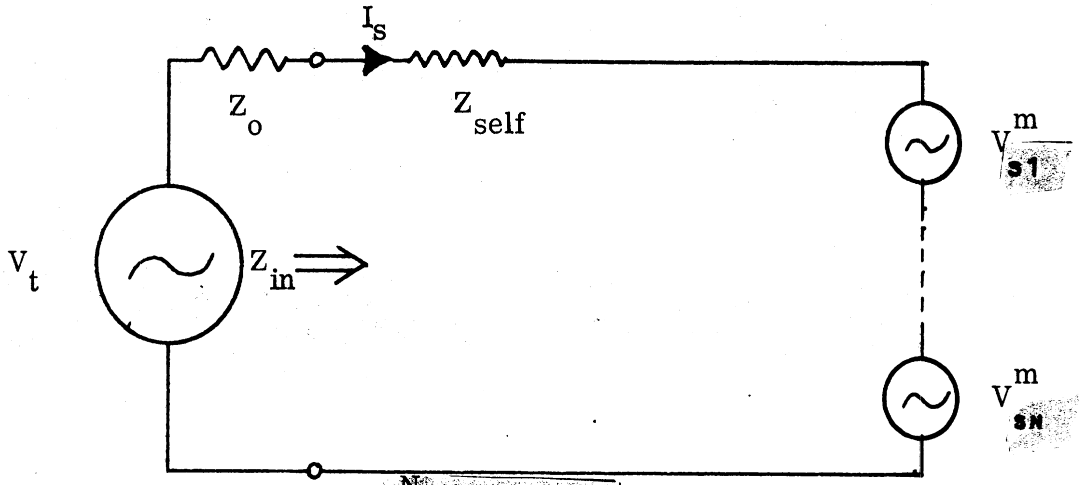

$$Z_{in} = Z_{self} + \sum_{\substack{j=1 \\ j \neq s}}^{N} \frac{V^m_{sj}}{I_s}$$

FIG. 5-21b: EQUIVALENT CIRCUIT FOR ELEMENT "s" IN AN "N" ELEMENT TRANSMITTING ARRAY.

N element array environment for the two possible modes of operation i.e., receive and transmit. The voltage sources labeled V_{sj}^{m} represent the voltages induced in the sample element by the remaining (N-1) array elements, i.e., mutual coupling effects. From these figures, it is apparent that from the circuit standpoint, mutual coupling effects may be interpreted in one of two ways, depending on the mode of operation of the array. When the array is transmitting, the voltage sources $V_{sj}^{m}\Big|_{\substack{j \neq s \\ j = 1,2,3\ldots}}$ in effect change the driving point impedance of the array element radiator from Z_{self} to Z_{in}, i.e., an impedance change due to mutual coupling effects. When the array is receiving, the voltage sources V_{sj}^{m} combine with the voltage term V_r (the voltage which would be induced in an isolated element) to yield a resultant voltage V_{sum}. The sum $\sum_{j=1}^{N}\Big|_{j \neq s} V_{sj}^{m}$ will vary from element to element within the array. As a result of such variations, the excitation distribution of an actual array usually differs from the theoretical model. The values given in the Tables of Figure 5-20 are sample values illustrating such excitation distortion in terms of power levels. The assumed theoretical distribution for all arrays considered here is a uniform one. Thus, in the absense of mutual coupling effects, all table entries should be identical i.e., all zeros. As is evident from the table entries, the departure from uniform illumination is considerable in all lattice arrays tested.

One other parameter of the array feed-network was measured to provide an additional check on the level of mutual coupling effects, and also as a check on one of the loss figures used in adjusting the array pattern power levels when determining absolute gain figures. This parameter is the standing wave ratio of the input port of each sixteen-way power divider used to feed one array deck. These measurements were made with the array in a transmitting mode of operation. Table V-3 summarizes these

	Input Port VSWR (Transmission Loss)			
Divider Number	1	2	3	4
Output Loading Condition				
50 Ω	1.68 (-.28db)	2.5 (-.9db)	2.4 (-.8db)	2.4 (-.8db)
2 Deck Lattice Array			2.98 (-1.2db)	2.05 (-.51db)
3 Deck Lattice Array		2.41 (-.8db)	1.97 (-.48db)	1.88 (-.41db)
4 Deck Lattice Array	1.78 (-.36db)	2.40 (-.8db)	2.01 (-.50db)	1.92 (-.45db)

TABLE IV-3 : Input Port Missmatch Characteristics of Radial Strip Transmission Line Power Dividers.

measurements, and gives the transmission loss equivalent to each standing wave ratio. The standing wave ratios and equivalent loss figures for each 16-way divider with uniform 50 ohm output port loading are also given for comparison.

5.4 Discussion of Experimental Results

Comparison of the experimental and theoretical array patterns shown in Section 5.3 indicates good agreement between experiment and theory. The level of agreement increases with array complexity. This trend can be attributed to two factors. First as the array complexity i.e., number of element radiators, increases, the array patterns become sharply directive. Such patterns are less subject to factors such as ground reflections and general coupling to various features of the array environment which tend to distort the pattern from the ideal. Secondly, as the number of element radiators increases, the averaging effect on certain types of spurious signals also increases, which should, in general decrease the total array sensitivity to such factors.

The half power beamwidth of each lattice array pattern is virtually identical with the corresponding theoretical value, and the null positions of theoretical and experimental patterns also show good agreement. The minimum depths of experimental pattern nulls are typically -20 to -25 db below the main beam maxima.

The broad beamed patterns of the various linear arrays show larger discrepancies from the theoretical values. These discrepancies are mostly due to the ellipticity of the antenna test pedestal rotator (See Appendix C). This factor resulted in apparently narrower beamwidths being recorded for the broad beamed patterns than was actually the case. The magnitude of this error was dependent on the position of the antenna on the test pedestal, and the worst positioning occurred for the linear endfire array.

The rotational symmetry of the lattice array patterns also appears to conform fairly well to theoretical prediction (see discussion below on statistical error effects on power level discrepancies within a given pattern).

The most significant disturbances in pattern symmetry occurred in the cases of vertical polarization (H plane patterns). In these cases, it was necessary to group a large number of coaxial feed lines along one edge of the array structure, and the most serious disturbances of pattern symmetry occur in the direction corresponding to the location of such cables. (The effect of these cables on element pattern factors was noted earlier and is mentioned again below.) Typically, the disturbances of array pattern symmetry are not large, and decrease with increasing array complexity.

In general, the theoretical and experimental lattice array patterns show almost exact agreement of power levels throughout the main beam, and good agreement through the first sidelobe. The power levels of the remaining sidelobes and the backlobe show varying levels of discrepancy, with theoretical values. The significance of such discrepancies with regard to agreement between experiment and theory is, however, minor. The argument on which this conclusion is based, is as follows.

The actual excitation and interelement spacing of each element radiator in an actual array are, at best, good approximations to the ideal values specified in the theoretical model. In addition, the materials used to support the element radiators and overall structure of the array create an environment which varies with aspect angle. The cumulative result of such effects can best be expressed from the statistical viewpoint. Generally speaking, the far-field of an actual array is, by superposition, a sum of individual terms, the magnitude and phases of which can be described as random variables having certain probability distributions, means, and variances. The observed agreement of experimental and theoretical radiation patterns discussed above suggests that the variances of such far field terms are small, with mean values in relatively good agreement with the ideal (non-statistical) values. However, the variances of such terms are certainly not likely to be zero, and consequently some discrepancies in the values of amplitude and phase of the far field terms exist. These discrepancies result in small variations in the power levels of the various far field components. In the case where the sum of the array element far field terms is large, e.g., the main beam, the effect of such variations is small compared with the sum. But when a sum of array element far field terms is small, e.g., sidelobes and backlobe, the effect of these variations, while small in an absolute sense, can be large compared to the value of the sum. For example, in the case of the 4 x 4 x 4 lattice array, statistical errors of this type which would cause an increase of 6 db from the ideal backlobe power level, correspond to a variation of less than .3 db at the power level of the main beam maximum, and about .7 db at the 3 db beamwidth points.

The measured experimental array gains differ from corresponding theoretical directivity values to varying degrees. Several factors can be cited as contributing to such discrepancies. First it is well known that the experimental measurement of absolute gain of an antenna is extremely difficult. In particular, any reflections from the ground, test mount, or feed networks can significantly influence gain figures. This is particularly true for broad beamed antennas such as the gain standard dipole used in the above measurements. One such effect noted was due to the coaxial feed line of the dipole, which appeared to distort the H plane (vertical polarization) dipole pattern. The result of this effect was to make the dipole more directive than theoretically predicted.

Finally, as discussed above, the experimental error limit applicable to the gain figures for the various lattice arrays is on the order of 1.0 db due to the complexity of the array system feed network. and inherent experimental equipment error.

As was discussed in Section 5.1, the criteria for establishing the feasibility, or physical realizability, of the lattice array concept relies on the combined results of gain and pattern measurements. The discussion of the above paragraphs indicates that measured gain figures, while indicative of the general level of array performance, cannot be relied upon as precise indicators. However, these gains, combined with the excellent agreement between experimental and theoretical radiation pattern cuts gives positive indication that the lattice array concept is physically realizable as an operating antenna system.

In an identical manner, the experimental gain and radiation pattern measurements generally support the theoretical results of Chapter III on lattice array directivities although discrepancies between experimental and theoretical values of array gain were encountered, as discussed above.

One point relating to these gain discrepancies is worth noting. The measurements of the 16 way power divider input port VSWR's (or equivalently, the input port impedance mismatch transmission loss), and the array element factors indicate that considerable mutual coupling between array elements exists. The experimental procedure used in this work gave minimal consideration to the impedance mismatch (illumination distortion) effects resulting from such mutual coupling (see above). Consequently, the possibility exists of decreasing the theoretical-experimental gain figure discrepancies by treating the various impedance mismatch (illumination distortion) problems in more detail experimentally.

From the practical standpoint, it is worth noting that the experimentally measured gains of the three and four deck lattice arrays are very close to the ideal gains of parabolic reflector antennas with comparable physical aperture areas (See Chapter III, Section 3.5.3.b).

The results of the E and H plane radiation pattern measurements together with the patterns indicating cross polarized radiation sensitivity indicate that coupling between array element radiators and element feed lines and balun structures has negligible effect on lattice array properties. Of course whether such effects are negligible due to a lack of actual induced source current distributions, or to an averaging effect over many different sources cannot be determined from these measurements. In any case, regardless of the mechanism, the observable sensitivity of the lattice arrays to such coupling effects is very low.

Finally, the overall results of the experimental measurement program permit an important interpretation of the theoretical results of Chapter III. These theoretical results for array directivities were arrived at under the assumptions of uniform excitation of the array elements, and ideal short dipole element patterns. The various measurements taken indicate considerable deviation of the experimental model from these theoretical assumptions. In particular the variation of element pattern factor power levels as indicated in the tables of Fig. 5-20 imply that the actual array excitation is quite distorted from the uniformly excited model. Also, the element pattern factors themselves are very distorted versions of the corresponding ideal dipole patterns. However, in spite of these deviations from the theoretical model assumptions, the results for array radiation patterns and array directive gains agree quite well in general with predicted values.

In view of these facts, it appears that the results of Chapter III for array directivities remain valid even when mutual coupling effects cause actual array characteristics, or parameters, to deviate considerably from those of the ideal theoretical model. An explanation for this result relates to the relative sharpness of the array pattern in comparison with an element pattern, or element pattern factor. If the array pattern is very directive in comparison with the element pattern, then the details of the element pattern have relatively little influence on the array directivity (excluding the possibility of an element pattern null in the direction of the array main beam).

Another consequence of the above results is that the numerical results of Chapter III for array directivities are applicable to arrays of elements other than dipoles, as long as the elements possess radiation patterns which are fairly smooth and slowly varying compared to the array factor pattern of their arrayed geometry.

CHAPTER VI

SUMMARY OF CURRENT WORK AND PROBLEM AREAS FOR FUTURE INVESTIGATION

6.1 Summary of Current Work

The preceding chapters have investigated in detail some of the properties of three dimensional dipole arrays. The directivity, and parameters related thereto, of lattice array configurations of short dipoles have been considered from a theoretical standpoint. Experimentally, the physical realizability of a lattice array has been investigated, and the correlation between theoretical and experimental values of certain array parameters established.

The theoretical portion of this work begins with the derivation of an exact expression for the directivity of arrays of short dipoles, with the array geometry and dipole orientations completely arbitrary. Based upon this expression, a numerical investigation of the maximum nominal directivity obtainable from a rectangular array geometry with a fixed number of element radiators was undertaken. Computer search procedures, specially developed for this investigation, resulted in detailed data on the nature of the surfaces and hypersurfaces defined by the directivity functions for two and three dimensional arrays. This data were displayed in the form of contour maps and single variable curves related to the directivity surfaces and hypersurfaces.

From the numerical data obtained, various array parameters were evaluated, i.e., array "bandwidth", maximum nominal directivity, and optimum element spacings. In addition, certain figures of merit, i.e., gain-beamwidth product, directivity per unit aperture area, directivity per unit volume, and the maximum nominal directivity factor, were investigated in order to provide a convenient basis for comparisons between two and three dimensional arrays, and between these arrays and parabolic reflector antennas. The maximum nominal directivity factor facilitated comparisons between optimally spaced arrays, and arrays with non-optimum interelement spacings.

A short discussion of the role of mutual coupling in the theoretical array model and in the subsequent analysis of this model is included at the end of Chapter III.

The experimental investigation can be divided into two categories. First, a feed-network was designed and developed which provided the appropriate excitation for the lattice arrays to be experimentally tested, and which minimized certain difficulties expected in exciting this type of array. A significant feature of this work was the design and development of a novel type of power divider. This device utilizes the principles of nonuniform transmission lines, and is constructed from strip-line materials.

The second phase of the experimental program was concerned with the actual measurement of radiation patterns and gain for various classes and sizes of arrays. The most complex of the arrays which were constructed and tested was a 4 x 4 x 4 lattice array. The agreement between the theoretical and experimental radiation patterns of the various arrays studied was quite good. The gain measurements were used to provide a check on the theoretical directivity values, although the measured gain is actually related to the directivity by an efficiency factor smaller than one. The agreement between the measured gain values and the theoretical directivities were relatively good, despite the efficiency factor, and certain difficulties related to the measurement procedures as discussed in Chapter V.

In addition to these measurements, which were used to establish the physical realizability of the lattice array concept, certain other data was obtained relating to mutual coupling effects in the array. This data indicates that the array radiation pattern and maximum nominal directivity are not very sensitive functions of such effects. An interpretation of this same data leads to the conclusion that the theoretical results for lattice array directivity and radiation pattern as given in Chapters II and III, are not limited to the short dipole elements used in the array model. In particular, the results of Chapters II and III would appear to hold for element radiators other than dipoles, as long as the directivity of the element is not comparable to the directivity of the array factor.

6.2 Problem Areas for Future Investigation

The role of mutual coupling effects in the lattice array model was mentioned from a theoretical standpoint in Chapter III, and considered experimentally on a qualitative basis in Chapter V. The results of the experimental investigation indicate that mutual coupling does not materially affect the maximum nominal directivity value obtained for the idealized array model. A numerical investigation of this experimental deduction would be of interest, and could be carried out based on the expressions for directivity given in Chapter II.

The experimental data obtained also led to the conclusion that the maximum nominal directivity value is not sensitive to the particular element radiator used in the array model. A numerical investigation of this fact could be carried out using the expression for the directivity of arrays of long dipoles as given in Appendix A.

The directivity maximization investigation carried out in Chapter III is addressed to the problem of obtaining the largest possible nominal directivity for rectangular array configurations with a fixed number of elements. Three other maximization problems could also be considered. First, under the constraint of rectangular array geometries, but with the number of element radiators a variable of the problem, what is the maximum directivity value attainable for an array of fixed spatial dimensions, i.e., fixed length, area, or volume.

A second maximization problem concerns the array configuration which results in the maximum nominal directivity for a fixed number of elements, i.e., the constraint of rectangular array geometries is removed from the original maximization problem.

A third problem is the obvious extension of the second. What is the maximum nominal directivity attainable by packing elements into some given region of space.

Each of the above maximization problems, including the original, were implicitly constrained to the condition of uniform illumination. If this constraint is removed, in any or all of the above problems, the complete optimization problem for array directivity could be considered, i.e., maximization of directivity with respect to both element positioning and element excitation. Such an analysis might take the form of an extension to higher dimensional arrays of Uzkov's fundamental optimization study for linear arrays (Uzkov, 1946)(See also, Tai, 1964).

A problem of primary importance in a full evaluation of the practicality of the lattice, or volume array concept, is that of the impedance properties of the element radiators of such arrays. Some theoretical work along this line has already been completed (Chang, 1967), but not much has been done experimentally.

Finally, as was mentioned in Chapter I, the three dimensional array offers an interesting alternative to the planar array for electronic beam scanning. The physical geometry of a three dimensional array would appear to have the potential for eliminating some of the beam broadening, grating lobe formation, and impedance variation problems which limit the scan angles obtainable with planar arrays. A theoretical study of the variation in directivity, beamwidth, and general radiation pattern behavior could be carried out. The expressions given in Chapter II could be used for the investigation of directivity in such a case.

The impedance variations encountered as a function of scan angle could also be studied on a theoretical or experimental basis. In conjunction with any experimental investigation of a scannable three dimensional array, the design problems related to a feed-network for such an array would almost certainly offer some unique and interesting problem areas.

These possible areas for future investigation offer a variety of challenging problems, some of which are perhaps intractable as stated here in their most general terms. However, these problem areas have been cited to point up the fact that the results presented during the course of this investigation represent only a few of the available problems which are related to three dimensional array configurations.

BIBLIOGRAPHY

Allen, J.L. (November 1964), "Array Antennas: New Applications for an Old Technique," IEEE Spectrum, 1 No. 11, pp. 115-130.

Arditi, M. (March 1955), "Characteristics and Applications of Microstrip for Microwave Wiring," IRE Transactions on Microwave Theory and Techniques, MTT-3, No. 2, pp. 31-49.

Barrett, R.M. (March 1955), "Microwave Printed Circuits - A Historical Survey," IRE Transactions on Microwave Theory and Techniques, MTT-3, No. 2, pp. 1-9.

Blass, J. (1960), "Multidirectional Antenna - A New Approach to Stacked Beams," IRE International Convention Record, Part I, Antennas and Propagation, pp. 48-50.

Chang, V.W.H., and P.W.P King (May 1967), "Theoretical Study of Dipole Array of N Parallel Elements," Cruft Laboratory Scientific Report No. 18 (Series 3), AFCRL-67-0404.

Delaney, W.P. (July 13, 1962), "Steering Radar Antenna Beams," Electronics, pp. 50-53.

Dukes, J.M.C. (March 1958), "The Application of Printed - Circuit Techniques to the Design of Microwave Components," Proc. IEEE, 105, Part B, No. 20, pp. 155-172.

Hansen, R.C. and R.S. Elliott (1966), "The Theory of Antenna Arrays," Chapter 1, pp. 1-67 of Volume II, Array Theory and Practice Microwave Scanning Antennas, Edited by R.C. Hansen, Academic Press.

Jasik, H. (Editor), (1961), Antenna Engineering Handbook, Chapter 30, McGraw-Hill Book Company, by K.S. Packard and R.V. Lowman, pp. 30 - 14 thru 30-18.

Kelleher, K.S. (1961), Antenna Engineering Handbook, Edited by H. J. Jasik, McGraw-Hill Book Company, Chapter 12, pp. 12-4 thru 12-13.

Ksienski, A. (October, 1961), "Signal Processing Antennas," Part I, Microwave Journal, 4, No. 10, pp. 77-85.

Ksienski, A. (November 1961), "Signal Processing Antennas," Part II, Microwave Journal, 4, No. 11, pp. 87-94.

BIBLIOGRAPHY
(Continued)

Sanders Associates (November 30, 1956), Handbook of Triplate Microwave Components, First Scientific Report, AFCRC-TN-56-961, ASTIA Doc. No. AD 110157, Published by Sanders Associates, Incorporated, Nashna, New Hampshire.

Shelton, J.P. and K.S. Kelleher (March 1961), "Multiple Beams from Linear Arrays," IRE Transactions on Antennas and Propagation, AP-9, No. 2, pp. 154-161.

Shnitkin, H. (December 1960), "Survey of Electronically Scanned Antennas," Microwave Journal, 3, No. 12, Part I, pp. 67-72.

Shnitkin, H. (January 1961), "Survey of Electronically Scanned Antennas," Microwave Journal, 4, No. 1, Part II, pp. 57-64.

Sterba, E.J. (July 1931), "Theoretical and Practical Aspects of Directional Transmitting Systems," Proc. IRE, 19, No. 7, pp. 1184-1215.

Tai, C.T. (31 March 1963), "The Gain of Uniform Arrays of Isotropic Sources and Dipoles," Report 1522-2, The Antenna Laboratory, The Ohio State University Research Foundation.

Tai, C.T. (July 1964), "The Optimum Directivity of Uniformly Spaced Broadside Arrays of Dipoles," IEEE Transactions on Antennas and Propagation, AP-12, No. 4, pp. 447-454.

Uzkov, A.I. (1946), "An Approach to the Problem of Optimum Directive Antennae Design," Comptes Rendus, Dok. Acad. Ser. ,USSR, L111, No. 1, pp. 35-38.

Wolff, E.A. (1966), Antenna Analysis, John Wiley and Sons, Incorporated, pp. 285-288.

Young, S.O. (February 1965), "Statistical Optimization of Antenna Processing Systems," Radio and Electronic Engineer, 29, No. 2, pp. 117-127.

APPENDIX A

DIRECTIVITY OF ARRAYS OF LONG DIPOLES

A.1 General Expression for the Directivity of Arrays of Long Dipoles with Arbitrary Array Geometry.

Consider the directivity expression for arrays of long dipoles. The locations of the dipole elements are arbitrary, as for the short dipole case of Chapter II but the orientations of the elements are not arbitrary; they are chosen so that the current elements representing the dipoles are in the +z direction. This specialization was made because the expressions for the more general case are not of immediate interest, and the results considerably more complex notationally.

Considering the basic nature of the problem at hand, it is apparent that for the long dipole array, the analysis of Chapter II, Section 2.2 still applies with only one change. This change is due to the different element pattern-product function $\mathcal{F}_{nm}(\theta, \phi)$. Since the long dipole elements of the array are identically oriented, the (n, m) subscript designation of the pattern-product function will be dropped, and this function will be designated as $\mathcal{F}(\theta, \phi)$.

For a long dipole of half length "ℓ", the (θ, ϕ) dependency of the E field pattern function is

$$f(\theta, \phi) = \frac{\cos(k\ell \cos\theta) - \cos(k\ell)}{\sin\theta}$$

Expanding the cosine terms of the numerator into their power series representations in terms of $\cos\theta$ and $\sin\theta$, we may express the pattern function in the form:

$$f(\theta, \phi) = \sin\theta \sum_{\alpha=0}^{\infty} A_{\alpha} \cos^{2\alpha}\theta$$

where

$$A_\alpha = \sum_{\nu=\alpha+1}^{\infty} (-1)^{\nu+1} \frac{(k\ell)^{2\nu}}{(2\nu)!} = \sum_{\nu=0}^{\alpha} (-1)^{\nu} \frac{(k\ell)^{2\nu}}{(2\nu)!} - \cos(k\ell)$$

Since the pattern-product function is the product of pairs of element patterns

$$\mathcal{F}(\theta,\phi) = \sin^2\theta \sum_{\alpha=0}^{\infty}\sum_{\beta=0}^{\infty} A_\alpha A_\beta (\cos\theta)^{2(\alpha+\beta)}$$

$$= \sin^2\theta \sum_{\gamma=0}^{\infty} \left\{ \sum_{\delta=0}^{\gamma} A_{\gamma-\delta} A_\delta \right\} \cos^{2\gamma}\theta$$

Using this $\mathcal{F}(\theta,\phi)$ in place of $\mathcal{F}_{nm}(\theta,\phi)$, an analysis comparable with that indicated in Section II-C can be carried out, with the result

$$D(\theta,\phi) = \frac{\sum_{n=1}^{N}\sum_{m=1}^{M} V_n V_m \cos(x_{nm} k\sin\theta\cos\phi + y_{nm} k\sin\theta\sin\phi + z_{nm} k\cos\theta + \delta_{nm}) \cdot}{\sum_{n=1}^{N}\sum_{m=1}^{N} V_n V_m \cos\delta_{nm} \left\{ \sum_{\omega=0}^{\infty} j_\omega(k\rho_{nm})\, G_\omega(k\rho_{nm},\mu_{nm}) \right\}}$$

$$\cdot \left\{ \frac{\cos(k\ell\cos\theta) - \cos k\ell}{\sin\theta} \right\}^2 \qquad \text{(A.1)}$$

where $G_0(k\rho_{nm},\mu_{nm}) = \sum_{\gamma=0}^{\infty} \left\{ \sum_{\delta=0}^{\gamma} A_{\gamma-\delta} A_\delta \right\} \mathcal{A}^{(1)}_{0,\gamma}(k\rho_{nm},\mu_{nm})$

and for $\omega \geq 1$

$$G_\omega(k\rho_{nm},\mu_{nm}) = \sum_{\gamma=\omega}^{\infty} \left\{ \sum_{\delta=0}^{\gamma} A_{\gamma-\delta} A_\delta \right\} \mathcal{A}^{(1)}_{\omega,\gamma}(k\rho_{nm},\mu_{nm})$$

$$+ \left\{ \sum_{\delta=0}^{\omega-1} A_{\omega-\delta-1} A_\delta \right\} \mathcal{A}^{(2)}_{\omega}(k\rho_{nm},\mu_{nm})$$

with

$$\mathcal{A}^{(1)}_{\omega,\gamma}(k\rho_{nm},\mu_{nm}) = \left(\frac{2}{k\rho_{nm}}\right)^{\omega} \Gamma(\omega+1) \sum_{p=\gamma-\omega}^{\gamma} \binom{2\gamma}{2p} (\cos\mu_{nm})^{2(\gamma-p)} (\sin\mu_{nm})^{2p}$$

$$\frac{[2(\gamma-p)-1]\,!!}{[2(\gamma-p)]\,!!} (-1)^{p+\omega-\gamma} \binom{p}{p+\omega-y} \left\{ 1 - \frac{[2(\gamma+1)]\,!\,(2p)\,!}{(2\gamma)\,!\,[2(p+1)]\,!} \sin^2\mu_{nm} \right\}$$

$$\mathcal{A}^{(2)}_{\omega}(k\rho_{nm},\mu_{nm}) = \left(\frac{2}{k\rho_{nm}}\right)^{\omega} (\omega+1) \sum_{p=-1}^{\omega-1} \binom{2\omega}{2(p+1)} (\cos\mu_{nm})^{2(\omega-p-1)}$$

$$(\sin\mu_{nm})^{2(p+1)} \frac{[2(\omega-p-1)-1]\,!!}{[2(\omega-p-1)]\,!!} (-1)^{p+\gamma}$$

Note: $[2n-1]\,!! \equiv 1\cdot 3\cdot 5\cdots(2n-1)$

$[2n]\,!! = 2\cdot 4\cdot 6\cdot 8\cdots(2n)$

and for $n = 0$, $[2n-1]\,!! = 1$ and $2n\,!! = 1$

Consider now the effect of truncating the infinite sums indicated in the denominator of $D(\theta,\phi)$. Such a truncation is equivalent to using an approximate pattern-product function $\mathcal{F}_M(\theta,\phi)$. where

$$\mathcal{F}_M(\theta,\phi) = \sin^2\theta \sum_{\alpha=0}^{M} \sum_{\beta=0}^{M} A_\alpha A_\beta (\cos\theta)^{2(\alpha+\beta)}$$

The error in the value of the denominator of $D(\theta,\phi)$ resulting from the use of this approximate pattern-product function is

$$\Bigg| \sum_{\alpha=0}^{\infty} \sum_{\beta=0}^{\infty} A_\alpha A_\beta \int_0^{\pi}\!\!\int_0^{2\pi} \cos(x_{nm} k\sin\theta\cos\phi + y_{nm} k\sin\theta\sin\phi + z_{nm} k\cos\theta + \delta_{nm}) \cos^{2(\alpha+\beta)}\theta \sin^2\theta \, d\Omega - \sum_{\alpha=0}^{M} \sum_{\beta=0}^{M} A_\alpha A_\beta \int_0^{\pi}\!\!\int_0^{2\pi} \cos(x_{nm} k\sin\theta\cos\phi + y_{nm} k\sin\theta\sin\phi + z_{nm} k\cos\theta + \delta_{nm}) \cos^{2(\alpha+\beta)}\theta \sin^2\theta \, d\Omega \Bigg| \le$$

$$\frac{40\,\pi\,(k\ell)^{2(M+2)}}{(2M+3)\,(2M+5)\,[2\,(M+2)]\,!} \equiv \epsilon\,(M,\,k\ell)$$

Some typical values of this error are:

1) For a half wave dipole:

$$\epsilon\left(3,\frac{\pi}{2}\right) \simeq 3 \times 10^{-4}, \quad \epsilon\left(6,\frac{\pi}{2}\right) \simeq 5 \times 10^{-10}$$

2) For a full wave dipole:

$$\epsilon\,(6,\,\pi) \simeq 3 \times 10^{-5}, \quad \epsilon\,(8,\pi) \simeq 2 \times 10^{-8}$$

Since from previous work it seems reasonable to expect that the value of the denominator for expected values of ℓ and M will be on the order of unity, these errors are negligible. The exact size of the error will, of course, depend upon M. For slight increases in the value of M, error bounds such as the ones given above can be made much smaller.

Using the finite sum approximation to the pattern-product function, i.e., $\mathcal{F}_M\,(\theta,\phi)$, the directivity function becomes:

$$D(\theta,\phi) = \frac{\sum_{N=1}^{N}\sum_{m=1}^{N} V_n V_m \cos(x_{nm} k \sin\theta \cos\phi + y_{nm} k \sin\theta \sin\phi + z_{nm} k\cos\theta + \delta_{nm}) \cdot \left\{\frac{\cos(k\ell\cos\theta) - \cos k\ell}{\sin\theta}\right\}^2}{\sum_{n=1}^{N}\sum_{m=1}^{N} V_n V_m \cos\delta_{nm} \left\{\sum_{\omega=0}^{2M+1} j_\omega(k\rho_{nm})\, G_\omega(K\rho_{nm},\mu_{nm})\right\}} \tag{A.2}$$

where M $\geq$ 1 with

$$G_0\,(k\rho_{nm},\mu_{nm}) = \sum_{\gamma=0}^{M}\left\{\sum_{\delta=0}^{\gamma} A_{\gamma-\delta}\, A_\delta\right\} \mathcal{A}_{0,\gamma}^{(2)}\,(k\rho_{nm},\mu_{nm}) +$$

$$+ \sum_{\gamma=M+1}^{2M}\left\{\sum_{\delta=\gamma-M}^{M} A_{\gamma-\delta} A_\delta\right\} \mathcal{A}_{0,\gamma}^{(1)}\,(k\rho_{nm},\,\mu_{nm})$$

and for $1 \leq \omega \leq M$

$$G_{\omega}(k\rho_{nm}, \mu_{nm}) = \sum_{\gamma=\omega}^{M} \left\{ \sum_{\delta=0}^{\gamma} A_{\gamma-\delta} A_{\delta} \right\} \mathcal{A}^{(1)}_{\omega,\gamma}(k\rho_{nm}, \mu_{nm}) + \left\{ \sum_{\delta=0}^{\omega-1} A_{\omega-\delta-1} A_{\delta} \right\} \bullet$$

$$\bullet\ \mathcal{A}^{(1)}_{\omega}(k\rho_{nm}, \mu_{nm}) + \sum_{\gamma=M+1}^{2M} \left\{ \sum_{\delta=\gamma-M}^{M} A_{\gamma-\delta} A_{\delta} \right\} \mathcal{A}^{(1)}_{\omega,\gamma}(k\rho_{nm}, \mu_{nm})$$

$$G_{M+1}(k\rho_{nm}, \mu_{nm}) = \left\{ \sum_{\delta=0}^{M} A_{M-\delta} A_{\delta} \right\} \mathcal{A}^{(2)}_{M+1}(k\rho_{nm}, \mu_{nm}) +$$

$$+ \sum_{\gamma=M+1}^{2M} \left\{ \sum_{\delta=\gamma-M}^{M} A_{\gamma-\delta} A_{\delta} \right\} \mathcal{A}^{(2)}_{M+1,\gamma}(k\rho_{nm}, \mu_{nm})$$

and for $M + 2 \leq \omega \leq 2M$

$$G_{\omega}(k\rho_{nm}, \mu_{nm}) = \sum_{\gamma=\omega}^{2M} \left\{ \sum_{\delta=\gamma-M}^{M} A_{\gamma-\delta} A_{\delta} \right\} \mathcal{A}^{(1)}_{\omega,\gamma}(k\rho_{nm}, \mu_{nm}) +$$

$$\left\{ \sum_{\delta=\omega-M-1}^{M} A_{\omega-\delta-1} A_{\delta} \right\} \mathcal{A}^{(2)}_{\omega}(k\rho_{nm}, \mu_{nm})$$

$$G_{2M+1}(k\rho_{nm}, \mu_{nm}) = A_{M}^{2}\, \mathcal{A}^{(2)}_{2M+1}(k\rho_{nm}, \mu_{nm})$$

with $\mathcal{A}^{(1)}_{\omega,\gamma}(k\rho_{nm}, U_{nm})$ and $\mathcal{A}^{(2)}_{\omega}(k\rho_{nm}, \mu_{nm})$ defined as before.

A.2 Directivity expressions for long dipole arrays with regular Array Geometry.

As seen in Section III, arrays having a regular geometry allow the expression for $D(\theta, \phi)$ to be simplified considerably by collecting terms of the numerator and of the denominator which have the same form and common parameter values. These parameter values occur in pairs, i.e., length and angle, and depend only on the geometry of the element locations. Since the simplification of D (θ, ϕ) is merely a counting problem for each parameter pair, the results achieved for each array type considered previously apply to the corresponding long dipole array. For example, a linear broadside array of N parallel, uniformly illuminated long dipoles has a maximum directivity.

$$D_{max} = N\,(1-\cos k\ell)^2 \Big/ 2\left\{ \sum_{\gamma=0}^{M} \left[\sum_{\delta=0}^{\gamma} A_{\gamma-\delta}\, A_{\delta} \right] \frac{1}{(2\gamma+1)\,(2\gamma+3)} + \sum_{\gamma=M+1}^{2M} \left[\sum_{\delta=\gamma-M}^{M} A_{\gamma-\delta}\, A_{\delta} \right] \frac{1}{(2\gamma+1)\,(2\gamma+3)} + \sum_{n=1}^{N-1} \left(1-\frac{n}{N}\right) \cdot \left\{ \sum_{\omega=0}^{2M+1} j_{\omega}\,(nck)\; G_{\omega}\,\left(nck, \frac{\pi}{2}\right) \right\} \right\}$$

Note: The first two terms of the denominator correspond to the case n=m, i.e., $\rho_{nm} = 0$). From this example it can be seen that the directivity expressions for long dipole arrays having the same array geometry as the short dipole cases considered in Chapter II can be written immediately from the combination of these previous results, and Eq. (A.2).

APPENDIX B

INTEGRATION TECHNIQUES

The principal difficulty to be resolved in obtaining an exact expression for the directivity of arrays of short dipoles with arbitrary array geometry and arbitrary element orientation, is the evaluation of integals of the general form:

$$I = \frac{1}{4\pi} \int_0^{\pi} \int_0^{2\pi} \cos(\lambda \sin\theta \sin(\phi + \xi) + \gamma \cos\theta + \delta) \cdot$$

$$\cdot \cos^{\alpha_1}\theta \sin^{\alpha_2}\theta \cos^{\alpha_3}\phi \sin^{\alpha_4}\phi \, d\Omega \ . \tag{1}$$

where $d\Omega \equiv \sin\theta \, d\phi \, d\theta$.

Consider a specific set of values for the parameters "α_i" of the integrand of (1) which will reduce this general expression to the particular form of one of the integrals denoted as $\mathcal{I}_i^{nm}$ in Chapter II, Section 2. 2. 2. In particular, consider the set of "α_i" which results in $\mathcal{I}_1^{nm}$, i.e., $\alpha_i = 0$ for all i. The techniques used in evaluating all of the integrals $\mathcal{I}_i^{nm}$ are identical. Only the algebraic complexities and number of trigonometric identities required to arrive at the final quadrature differ from case to case. $\mathcal{I}_1^{nm}$ is the least complicated integral in the sense of the amount of such algebraic and trigonometric manipulations, and was chosen for this reason to illustrate the various integration techniques used.

For the case $\alpha_i = 0$ for all i, the expression (1) becomes

$$I = \frac{1}{4\pi} \int_0^{\pi} \int_0^{2\pi} \cos(\lambda \sin\theta \sin(\phi + \xi) + \gamma \cos\theta + \delta) \, d\Omega \ .$$

Expanding the integrand

$$I = I_1 \cos\delta + I_2 \sin\delta$$

where

$$I_1 = \frac{1}{4\pi}\int_0^{\pi}\int_0^{2\pi} \cos(\lambda \sin\theta \sin(\phi + \xi) + \gamma\cos\theta)\ d\Omega \quad .$$

and

$$I_2 = \frac{1}{4\pi}\int_0^{\pi}\int_0^{2\pi} \sin(\lambda \sin\theta \sin(\phi + \xi) + \gamma\cos\theta)\ d\Omega \quad .$$

Consider the evaluation of the expression for I_1.. The integrand of I_1 is seen to be a periodic function of the variable "ϕ", with a period of either π or 2π, depending on the value of $\gamma \cos\theta$.

The integration with respect to "ϕ" is over the interval $[0, 2\pi]$. Given the periodicity of the integrand, a change of variable $\phi \rightarrow \phi' - \xi$ and a subsequent shift of the resulting range of integration from $[\xi, 2\pi + \xi]$ to $[0, 2\pi]$ can be carried out without affecting the result of the integration. Carrying out these operations, the expression for I_1 becomes (with the primed notation dropped):

$$I_1 = \frac{1}{4\pi}\int_0^{\pi}\int_0^{2\pi} \cos(\lambda \sin\theta \sin\phi + \gamma\cos\theta)\ d\Omega \quad .$$

From this point on, the principal task is to perform appropriate coordinate transformations so as to obtain the integrand in a form for which the indicated integrations are tractable. This procedure is enormously facilitated by using the technique of Watson mentioned in Chapter II, Section 2.2.2. Basically, this technique involves performing coordinate transformations by permuting the direction cosines denoted by the symbols ℓ, m, and n, and defined by the relationships $\ell = \cos\theta_x = \sin\theta\cos\phi$, $m = \cos\theta_y = \sin\theta\sin\phi$ and $n = \cos\theta_z = \cos\theta$. The region of integration is considered a spherical "cap" which remains fixed in three-dimensional space while the coordinate transformations are being carried out. In the expression for I_1, the "cap" is, in fact, the complete sphere.

Using this notation and conceptual procedure, the expression for I becomes:

$$I_1 = \frac{1}{4\pi}\iint_\Omega \cos(\lambda m + \gamma n)\, d\Omega \quad .$$

Performing the transformation $\ell \rightarrow -n'$, $m \rightarrow m'$ and $n \rightarrow \ell'$

$$I_1 = \frac{1}{4\pi}\iint_\Omega \cos(\lambda m' + \gamma \ell')\, d\Omega \quad .$$

Substituting the expressions for m' and ℓ' in terms of the variables "θ'" and "ϕ'"

$$I_1 = \frac{1}{4\pi}\int_0^{\pi}\int_0^{2\pi} \cos(\lambda \sin\theta' \sin\phi' + \gamma \sin\theta' \cos\phi')\, d\Omega \quad .$$

Dropping the prime notation, and using the relationship

$$\lambda \sin\theta \sin\phi + \gamma \sin\theta \cos\phi = \rho \sin\theta \sin(\phi + \mu)$$

where

$$\rho = \sqrt{\lambda^2 + \gamma^2} \qquad \text{and} \qquad \mu = \tan^{-1}\left(\frac{\gamma}{\lambda}\right)$$

the expression for I_1 becomes

$$I_1 = \frac{1}{4\pi}\int_0^{\pi}\int_0^{2\pi} \cos(\rho \sin\theta \sin(\phi + \mu))\, d\Omega \quad .$$

Now the integrand is a periodic function of "ϕ" with period π, and so proceeding as above and substituting the expression for $d\Omega$ as a function of "θ" and "ϕ", the expression for I_1 becomes.

$$I_1 = \frac{1}{4\pi}\int_0^{\pi}\int_0^{2\pi} \cos(\rho \sin\theta \sin\phi) \sin\theta\, d\phi\, d\theta \quad .$$

Using the direction cosine notation, this expression can be rewritten as

$$I_1 = \frac{1}{4\pi} \int_0^{\pi} \int_0^{2\pi} \cos(\rho\ m)\, d\Omega \quad .$$

Performing the transformation $\ell \rightarrow \ell'$, $m \rightarrow n'$, $n \rightarrow -m'$, the expression for I_1 becomes

$$I_1 = \frac{1}{4\pi} \int_0^{\pi} \int_0^{2\pi} \cos(\rho\ n')\, d\Omega \quad .$$

Dropping the prime notation and substituting the expression for "n" in terms of "θ", I_1 becomes

$$I_1 = \frac{1}{4\pi} \int_0^{\pi} \int_0^{2\pi} \cos(\rho \cos\theta) \sin\theta\, d\phi\, d\theta \quad .$$

With the integrand in this form the indicated integrations can be easily carried out. Integrating with respect to "ϕ", the expression for I_1 becomes.

$$I_1 = \frac{1}{2} \int_0^{\pi} \cos(\rho \cos\theta) \sin\theta\, d\theta \quad .$$

Integrating with respect to "θ", the expression for I_1 becomes

$$I_1 = \frac{1}{2} \left\{ - \frac{\sin(\rho\cos\theta)}{\rho} \Bigg|_0^{\pi} \right\} = \frac{1}{2} \left\{ \frac{\sin\rho}{\rho} + \frac{\sin\rho}{\rho} \right\}$$

$$\therefore\ I_1 = \frac{\sin\rho}{\rho}$$

Returning now to the expression for I_2, it is seen that the integrand has the same functional dependency on "θ" and "ϕ" as does I_1. None of the operations performed in evaluating I_1, up to the final evaluations of the definite double integral, depended on the fact that the integrand behaved as the cosine of a functional dependency on "θ" and "ϕ". Therefore, the identical procedure can be carried out for I_2 with the result that the expression for I_2 becomes

$$I_2 = \frac{1}{4\pi} \int_0^{\pi} \int_0^{2\pi} \sin(\rho \cos\theta) \sin\theta \, d\phi \, d\theta \quad .$$

If the integration with respect to "ϕ" is carried out, the expression for I_2 becomes

$$I_2 = \frac{1}{2} \int_0^{\pi} \sin(\rho \cos\theta) \sin\theta \, d\theta \quad .$$

Carrying out the integration with respect to "θ", the following result is obtained:

$$I_2 = \frac{1}{2} \left\{ - \frac{\cos(\rho \cos\theta)}{\rho} \Bigg|_0^{\pi} \right\} = \frac{1}{2} \left\{ - \frac{\cos\rho}{\rho} + \frac{\cos\rho}{\rho} \right\}$$

$\therefore$

$$I_2 = 0 \quad .$$

Combining the above results for I_1 and I_2, the final expression for I is:

$$I = \cos\delta \, \frac{\sin\rho}{\rho} \quad .$$

APPENDIX C

ANTENNA MEASUREMENT FACILITIES AND APPARATUS

All antenna pattern and gain measurements were performed on a 30' test range. Standard measurement techniques were used. The details of the various equipments were as follows. The transmitting system consisted of an L-band horn having an E-plane half-power beamwidth of 22° and an H-plane half-power beamwidth of 29°. This horn was driven by a GR-1218-A source (frequency range 1.0 - 2.0 GHz, maximum power output 300 mw). The transmitting frequency was checked with a wave meter, and the output power level was monitored with an HP-415-A SWR meter using a crystal detector and a -20 db directional coupler. The transmitting antenna was located approximately 20' above the ground on a wooden support tower. The antenna test mount utilized a 584 type radar pedestal which provided for lowering and raising the test model and also rotating the model in the transmitted field. This test mount and supporting equipment were standard apparatus used by the Radiation Laboratory. The lengths of the various components of the test mount, combined with the antenna height were always adjusted to provide good alignment of the test model height with the transmitter antenna height. In view of the fairly broad beamwidth of the transmitting horn, this adjustment was not very critical in terms of maintaining uniform excitation across the array face for the actual range length and maximum antenna dimensions. The length of the range, i.e. 30 feet, was more than sufficient to satisfy the condition $R > 2d^2/\lambda$ ($2d^2/\lambda \leq 16.7$ feet for this case) for a sufficiently planar wavefront of the exciting wave, and care was taken to maintain the array orientation with respect to that of the transmitting horn to prevent linear phase distortion across the array face.

A feature of the rotator mount which should be noted is an eccentricity of ± 8" in the position of an antenna (mounted on the standard support poles) about the center of rotation of the test pedestal. Adaptation of the mount to accommodate the various array types tested changed the magnitude of this eccentricity. However, based on the free space attenuation constant, an upper bound on the variation of signal amplitude caused by the largest such eccentricity is -1.0 db.

The signal recording equipment was a standard arrangement using a bolometer detector and an Antlab recorder with capabilities for recording polar or rectangular patterns on either a db or linear scale.

The general arrangement of the test range facilities is shown in the following photograph (FIG. C-1).

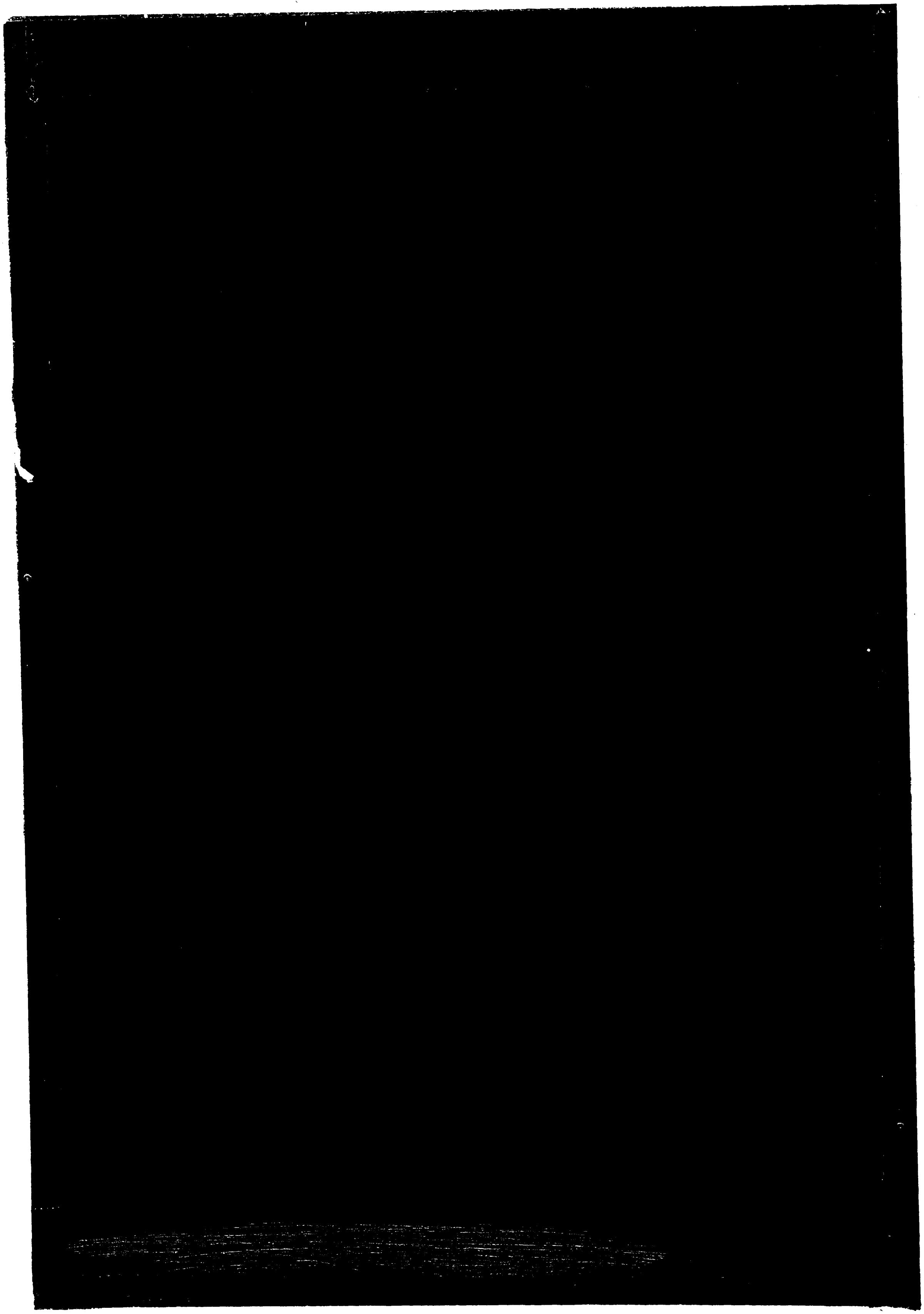

FIG. C-1: 30' ANTENNA TEST RANGE.

APPENDIX D

RADIATION PATTERNS OF LINEAR, PLANAR, AND LATTICE ARRAYS

The radiation patterns given here are included in this thesis for completeness, and are sufficiently labeled so as to be self explanatory. The term "element pattern factor" is explained in Chapter V, Section 5.2. The patterns labeled "cross polarized" indicate a measurement performed with the array cross polarized to the field of the incident wave. The significance of this measurement is also discussed in Chapter V, Section 5.2.

The array patterns, and the element pattern factors of deck-numbers one and four of the 4x4x4 lattice array (both "E" and "H" plane cuts) are given in Chapter V, Section 5.3.

FIG. D-1: FOUR ELEMENT LINEAR ENDFIRE ARRAY RADIATION PATTERN — "E" PLANE CUT.

E-1

E-2

E-3

E-4

FIG. D-2: ELEMENT PATTERN FACTORS OF A FOUR ELEMENT LINEAR ENDFIRE ARRAY — "E" PLANE CUT.

Experimental

Theoretical

FIG. D-3: FOUR ELEMENT LINEAR ENDFIRE ARRAY RADIATION PATTERN — "H" PLANE CUT.

E-1 E-2

E-3 E-4

FIG. D-4: ELEMENT PATTERN FACTORS OF A FOUR ELEMENT LINEAR ENDFIRE ARRAY — "H" PLANE CUT.

Array

E-1

E-2

E-3

E-4

FIG. D-5: ARRAY RADIATION PATTERN AND ELEMENT PATTERN FACTORS OF A FOUR ELEMENT BROADSIDE LINEAR ARRAY OF COLLINEAR ELEMENTS – "H" PLANE CUT.

FIG. D-6: RADIATION PATTERN OF A FOUR ELEMENT BROADSIDE LINEAR ARRAY OF COLLINEAR ELEMENTS — "E" PLANE CUT.

E-1

E-2

E-3

E-4

FIG. D-7: ELEMENT PATTERN FACTORS OF A FOUR ELEMENT BROADSIDE LINEAR ARRAY OF COLLINEAR ELEMENTS — "E" PLANE CUT.

Array

E-1

E-2

E-3

E-4

FIG. D-8: ARRAY RADIATION PATTERN AND ELEMENT PATTERN FACTORS OF A FOUR ELEMENT BROADSIDE LINEAR ARRAY OF PARALLEL ELEMENTS — "E" PLANE CUT.

Experimental

Theoretical

FIG. D-9: RADIATION PATTERN OF A FOUR ELEMENT BROADSIDE LINEAR ARRAY OF PARALLEL ELEMENTS — "H" PLANE CUT.

E-1

E-2

E-3

E-4

FIG. D-10: ELEMENT PATTERN FACTORS OF A FOUR ELEMENT BROADSIDE LINEAR ARRAY OF PARALLEL ELEMENTS — "H" PLANE CUT.

1-1

2-1

1-2

2-2

1-3

2-3

1-4

2-4

FIG. D-11: ELEMENT PATTERN FACTORS OF A SIXTEEN ELEMENT PLANAR ARRAY – ROWS No. 1 AND No. 2 – "E" PLANE CUT.

3-1

4-1

3-2

4-2

3-3

4-3

3-4

4-4

FIG. D-12: ELEMENT PATTERN FACTORS OF A SIXTEEN ELEMENT PLANAR ARRAY — ROWS No. 3 AND No. 4 — "E" PLANE CUT.

1-1

2-1

1-2

2-2

1-3

2-3

1-4

2-4

FIG. D-13: ELEMENT PATTERN FACTORS OF A SIXTEEN ELEMENT PLANAR ARRAY – ROWS No. 1 AND No. 2 – "H" PLANE CUT.

3-1 4-1

3-2 4-2

3-3 4-3

3-4 4-4

FIG. D-14: ELEMENT PATTERN FACTORS OF A SIXTEEN ELEMENT PLANAR ARRAY — ROWS No. 3 AND No. 4 — "H" PLANE CUT.

1-1 1-2

2-1 2-2

3-2 3-3

4-4

FIG. D-15: ELEMENT PATTERN FACTORS – DECK No. 1 OF 4x4x2 LATTICE ARRAY – "E" PLANE CUT.

1-1 1-2

2-1 2-2

3-2 3-3

4-4

FIG. D-16: ELEMENT PATTERN FACTORS – DECK No. 2 OF 4x4x2 LATTICE ARRAY – "E" PLANE CUT.

1-1 1-2

2-1 2-2

3-2 3-3

4-4

FIG. D-17: ELEMENT PATTERN FACTORS – DECK No. 1 OF 4x4x2 LATTICE ARRAY – "H" PLANE CUT.

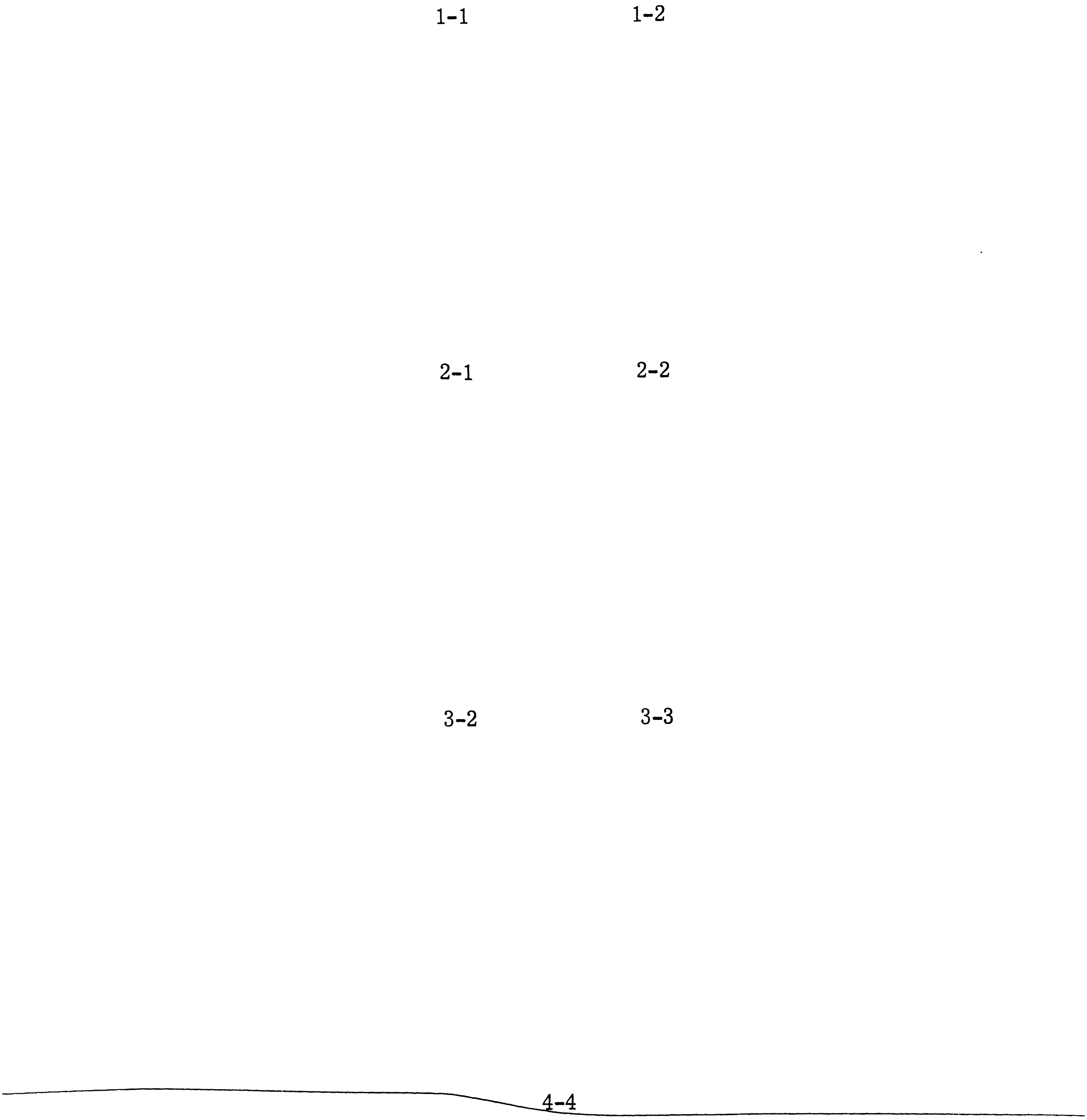

FIG. D-18: ELEMENT PATTERN FACTORS – DECK No. 2 OF 4x4x2 LATTICE ARRAY – "H" PLANE CUT.

1-1 1-2

2-1 2-2

3-2 3-3

4-4

FIG. D-19: ELEMENT PATTERN FACTORS – DECK No. 1 OF 4x4x3 LATTICE ARRAY – "E" PLANE CUT.

1-1 1-2

2-1 2-2

3-2 3-3

4-4

FIG. D-20: ELEMENT PATTERN FACTORS – DECK No. 2 OF 4x4x3 LATTICE ARRAY – "E" PLANE CUT.

1-1 1-2

2-1 2-2

3-2 3-3

4-4

FIG. D-21: ELEMENT PATTERN FACTORS – DECK No. 3 OF 4x4x3 LATTICE ARRAY – "E" PLANE CUT.

1-1 1-2

2-1 2-2

3-2 3-3

4-4

FIG. D-22: ELEMENT PATTERN FACTORS — DECK No. 1 OF 4x4x3 LATTICE ARRAY — "H" PLANE CUT.

1-1 1-2

2-1 2-2

3-2 3-3

4-4

FIG. D-23: ELEMENT PATTERN FACTORS — DECK No. 2 OF 4x4x3 LATTICE ARRAY — "H" PLANE CUT.

1-1 1-2

2-1 2-2

3-2 3-3

4-4

FIG. D-24: ELEMENT PATTERN FACTORS – DECK No. 3 OF 4x4x3 LATTICE ARRAY – "H" PLANE CUT.

1-1 1-2

2-1 2-2

3-2 3-3

4-4

FIG. D-25: ELEMENT PATTERN FACTORS — DECK No. 2 OF 4x4x4 LATTICE ARRAY — "E" PLANE CUT.

1-1 1-2

2-1 2-2

3-3 4-4

FIG. D-26: ELEMENT PATTERN FACTORS – DECK No. 3 OF 4x4x4 LATTICE ARRAY – "E" PLANE CUT.

1-1 1-2

2-1 2-2

3-2 3-3

4-4

FIG. D-27: ELEMENT PATTERN FACTORS — DECK No. 2 OF 4x4x4 LATTICE ARRAY — "H" PLANE CUT.

1-1 1-2

2-1 2-2

3-2 3-3

4-4

FIG. D-28: ELEMENT PATTERN FACTORS – DECK No. 3 OF 4x4x4 LATTICE ARRAY – "H" PLANE CUT.